TECHNICAL MEMORANDUM

724

Recommended Fire Emission Service Enhancements

J.W. Kaiser[1,2,3], N. Andela[4], J. Atherton[1], M. de Jong[1], A. Heil[5], R. Paugam[1], S. Remy[2], M.G. Schultz[5], G.R. van der Werf[4], T.T. van Leeuwen[4], M.J. Wooster[1]

Research Department

May 2014

[1] King's College London, UK
[2] ECMWF, UK
[3] Max Planck Institute for Chemistry, Germany
[4] Free University Amsterdam, The Netherlands
[5] Forschungszentrum Jülich, Germany

This report has been delivered to EU as MACC-II project deliverable D_32.1.

European Centre for Medium-Range Weather Forecasts
Europäisches Zentrum für mittelfristige Wettervorhersage
Centre européen pour les prévisions météorologiques à moyen

Series: ECMWF Technical Memoranda

A full list of ECMWF Publications can be found on our web site under:
http://www.ecmwf.int/publications/

Contact: library@ecmwf.int

European Centre for Medium Range Weather Forecasts
Shinfield Park, Reading, Berkshire RG2 9AX, England

Executive Summary

The Global FIRE Assimilation System (GFAS) uses satellite-based fire observations to estimate global smoke constituent emission rates from vegetation fires. They are used as boundary conditions in the atmospheric composition and air quality forecasting systems implemented by MACC-II for the Copernicus Atmosphere Services (CAS). GFAS is itself a service implemented by MACC-II for the CAS, which attracts a growing user-base worldwide. This report summarises the research that has gone into improving GFAS during MACC-II and provides a roadmap for the evolution of the operational fire emissions service into the CAS. It addresses the topics identified in a recent assessment of the performance and the user feedback of the routinely produced version, GFASv1.

The following enhancements are recommended for the next update of GFAS. Their scientific developments are essentially concluded and their implementation in the routine production system is overall progressing well:

- more specific observation data quality control
- correction for varying fire detection thresholds across the MODIS swath
- resilience against failure of one of the MODIS instruments
- improved spurious signal mask for volcanoes and gas flares
- land cover map with higher resolution and more specific land cover classes, plus peat
- updated conversion factors for fire radiative power (FRP) to dry matter burnt (DM)
- annual variability in the emission factors for CO_2, CO and CH_4
- updated emission factors for all other chemical species and aerosol types
- injection height estimation with dedicated observation products and plume rise model

Our scientific investigations of the representation of the diurnal variability of fires and the correction of the low bias of geostationary observations have also progressed. The current lines of research focus on fitting the parameters of a Gaussian for the diurnal variability and a FRP- and viewing angle-based bias correction, which is conceptually consistent with the correction for varying fire detection thresholds across the MODIS swath. These developments will be incorporated into GFAS. They will improve the temporal resolution to one hour, reduce inaccuracies, and increase the redundancy of input data, thus improving the operational stability of GFAS.

Further investigations have tested for spurious FRP signals from industrial activities other than gas flares, advanced the understanding of the relationships between FRP and DM, and between FRP and the fire weather index. These investigations will probably need to be followed up in the CAS to improve the GFAS service.

In the long term, the approach of scaling FRP to DM from another inventory will reach its limits because it preserves the inaccuracies of the reference inventory. On the other hand, information from atmospheric smoke plume observations becomes more and more accessible. We therefore propose to develop GFAS further into a fire emission model that is derived from physical understanding, fire observations and other fire emission inventories like GFED, and parameterise the main uncertainties. The parameters should then be estimated from atmospheric observations with the help of the global CAS systems. This approach will require even closer interaction with follow-up activities of the global production and validation sub-project of MACC-II/-III and with the wider fire research community, most usefully represented in the Interdisciplinary Biomass Burning Initiative (IBBI).

TABLE OF CONTENTS

1 Introduction

1.1 General introduction

The Global Fire Assimilation System (GFAS) has been developed in the MACC and MACC-II projects for producing vegetation smoke emission estimates in real time to serve as boundary conditions of the atmospheric analyses and forecasts in EU's global and European Copernicus Atmosphere Services (CAS). GFAS is based on satellite fire radiative power observations and uses the Global Fire Emissions Database (GFED) as a reference for conversion of FRP to dry matter burned. The assimilation system contains a simple parameterisation to forecast fire emissions in case of cloud obscureness etc., and it provides daily global emission estimates of a large variety of trace gases and aerosol compounds that can be used in global and regional chemistry transport models. For details of GFAS version 1, see Kaiser et al., 2012. This report summarises the research that has gone into improving GFAS during MACC-II and provides a roadmap for the evolution of the operational fire emissions service into the CAS.

GFAS development started in the MACC project and has continued throughout MACC-II, the Interim Implementation of (the services to) Monitoring Atmospheric Composition and Climate. In late 2013, two sub-versions, 1.0 and 1.1, of GFASv1 run in real-time production mode. The main difference is in their resolutions: 0.5 deg and 0.1 deg, respectively. GFAS is routinely used as input for all global and several regional atmospheric services of MACC-II. In addition, it has a growing user base in several research groups worldwide. The FIR sub-project of MACC-II is developing updates for GFAS in order to achieve a service provision with improved accuracy and new products according to the requirements of the atmospheric services in the CAS. In doing so, MACC-II takes advantage of, and contributes to, the latest research in the very active scientific field of emission estimation from vegetation fires.

A recent MACC-II report [deliverable D_31.2, also available as Andela et al., 2013] has characterised the accuracy of GFASv1, and confirmed its suitability for the pre-operational productions. While the accuracy of GFAS was found to be state-of-the-art, several areas were identified, in which enhancement of the GFAS would improve the accuracy of the CAS. Concerning the monitoring of global fire radiative power (FRP), on which GFAS is built, the report recommends further development in four respects:

- compensation of the viewing angle-dependency of the MODIS fire detection threshold
- improved temporal resolution using an updated fire model and geostationary observations
- correction of bias between daily observations of the two MODIS instruments
- improved quality control and spurious signal masking

These aspects are addressed in Chapter 2 below. Concerning the estimation of emissions from FRP, the recent report recommends further development regarding:

- a better adapted calculation of emission factors of FRP to dry matter burnt
- dedicated peat fire treatment throughout the boreal region
- validation activity

The first two aspects are addressed in Chapter 3 of this document. The validation is discussed in Section 1.2 below. Concerning system extensions, the recent reports suggests to implement

- fire activity forecasts
- injection height estimates

These aspects are addressed in Chapter 4 of this document. Finally, Chapter 5 summarises the conclusions that are currently being drawn from the research activities of the FIR sub-project and the status of the implementation of GFAS updates. It also lists recommendations for further research and updates to be performed in 2014 and during the operation production phase of GFAS.

1.2 Remark on validation

Validation of global fire emissions is notoriously difficult because direct quantification of such emissions is only possible in laboratory experiments, in which fires are necessarily much smaller and thus have different burning characteristics than vegetation burning in open landscapes. The comparison of trace gas and aerosol concentrations resulting from fire emissions with field measurements is confounded by the fact that fuel conditions and ambient atmospheric conditions are highly variable. Numerous ground-based and air-borne field campaigns have measured smoke composition in the atmosphere near the fire or further downwind. Satellite observations, mostly of aerosol optical depth and carbon monoxide, have been have been used in inversion studies to give top-down estimates of fire emissions.

Andela et al. 2013 have shown that real-time fire emission estimates can be verified through a comparison with several other, possibly retrospective, emission estimates. While consistency with other bottom-up inventories lends credibility, it is not strictly an independent validation since all inventories share common elements. Therefore, a comprehensive independent validation can only be achieved against independent atmospheric plume observations. The MACC-II systems provide a unique opportunity for such validation because they combine global, long-term coverage with a comprehensive set of species. Additionally, a large number of observations are already considered in the data assimilation and regular validation reports, e.g. Eskes et al. 2013, compare the MACC-II model to independent observations. However, possible errors of the atmospheric simulations have to be taken into account before conclusions on the accuracy of the fire emissions can be drawn. This requires personal interaction with the atmospheric model development and validation teams on a case-by-case basis. Therefore, it is impossible to apply an automated, comprehensive validation procedure for fire emissions with the atmospheric systems of MACC-II. Instead, Andela et al. 2013 have compiled a set of study cases from the MACC-II validation reports and the wider literature. The reader is referred to the Andela et al., 2013 report for details. In the meantime, another well observed case has occurred with the long-range transport of smoke plumes from Canadian fires across the Atlantic in July 2013. The structure of the plumes have been well observed by the ceilometer network of the German weather service, cf. Figure 1.

In order to establish a more systematic and comprehensive validation procedure for the fire emissions, it would be helpful to perform sensitivity studies with the full global MACC-II model, i.e. aerosols, reactive gases and greenhouse gases, with nudged meteorology. Producing such simulations in real-time was recommended also in the conclusions of the MACC-II workshop reactive gases, greenhouse gases and aerosols in Wermelskirchen (June 2013). We recommend making the corresponding model set-up

available in MACC-II for additional sensitivity studies w.r.t. fire emission that can be evaluated against the collected set of case studies and any further cases that get identified in future validation reports.

Furthermore, since GFAS is gaining more users within the scientific community who apply the emission estimates in their modelling studies of field campaigns etc., such feedback can also provide additional validation and help to identify potential shortcomings of the fire emission system. A new international platform to discuss such activities and results is the Interdisciplinary Biomass Burning Initiative (IBBI), which is sponsored by WMO, IGAC and iLEAPS.

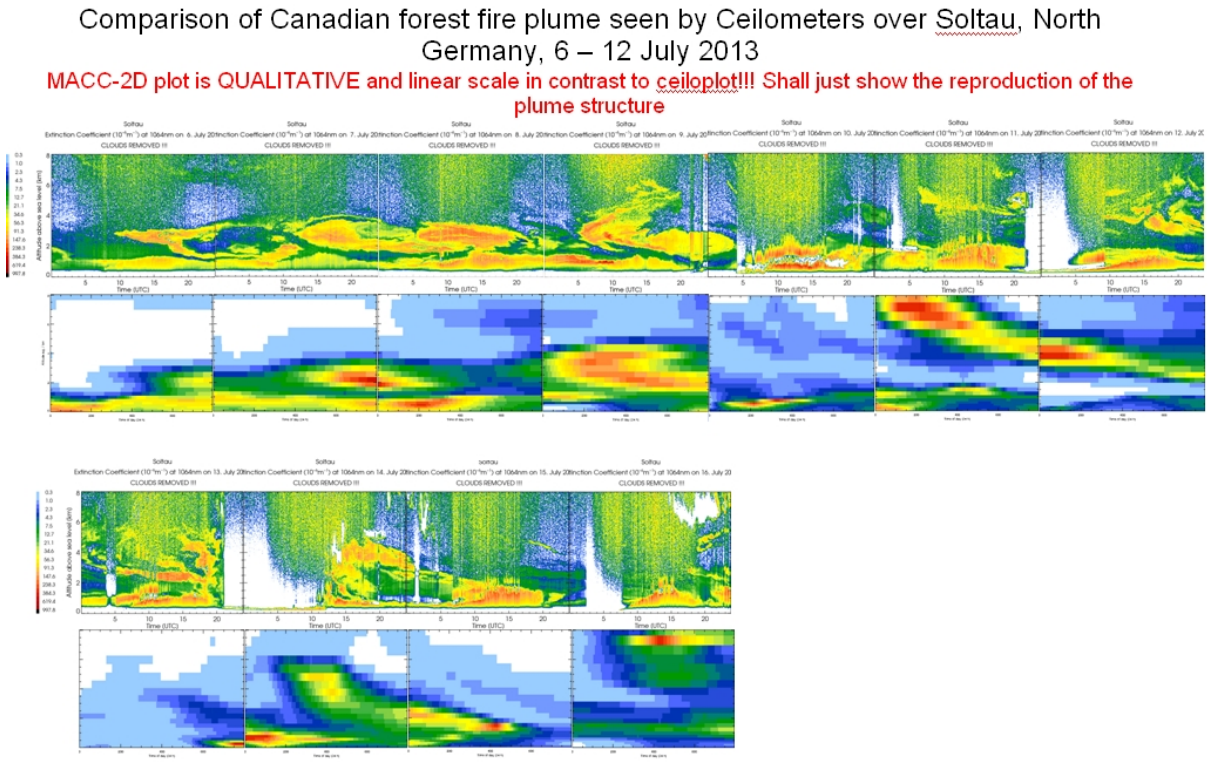

Figure 1: Comparison of DWD ceilometer profiles (top rows) and MACC-II real-time analyses of aerosol optical depth profiles (bottom rows). (Courtesy Harald Flentje, DWD Hohenpeißenberg)

2 Analysis and processing of FRP observations

2.1 Swath-dependence of MODIS fire detections

The fire detection threshold of the MODIS instrument varies across the swath; it is smallest at the sub-satellite point and increases with viewing angle and pixel size towards the swath edges [Freeborn et al. 2010, Hyer et al. 2013]. This effect leads to lower FRP estimates in GFASv1 for grid cells that are observed nearer the MODIS swath edges. With the observational pattern of the MODIS instruments a spurious oscillation with a period of ~2 days is thus introduced in GFAS, which is most pronounced in the tropics [Andela et al. 2013, Sect. 5.2].

In this chapter, we analyse the effect of the viewing-angle dependence of the detection threshold on two quantities: (1) the average observed FRP and (2) the size-distribution of the observed FRP. All analyses are based on the MODIS FRP observations as represented in the gridded fields of GFASv1.1.

2.1.1 Average observed FRP

Figure 2 shows the annual average FRP observed by each of the MODIS instruments depending on viewing angle as represented in the gridded GFASv1.1 processing for two different years. Also shown is the behaviour of the merged dataset from both instruments. The lower panels show the normalisation of these curves to the values at the sub-satellite point; the relative FRP bias in GFASv1 is due to the reduced detection threshold for viewing angles > 0. Each individual fire is sampled only at a single viewing angle. However, the variable overpass geometry of MODIS together with the large sampling period effectively ensures that virtually identical fire distributions with identical average FRPs are sampled by each instrument with the different viewing angles. The fact that the curves are smooth shows that the sample is indeed large enough. Since all curves in the two lower panels agree within ~5%, it can be hypothesised that both instruments have the same relative bias and that the bias might be parameterised by a (almost quadratic) function with two parameters.

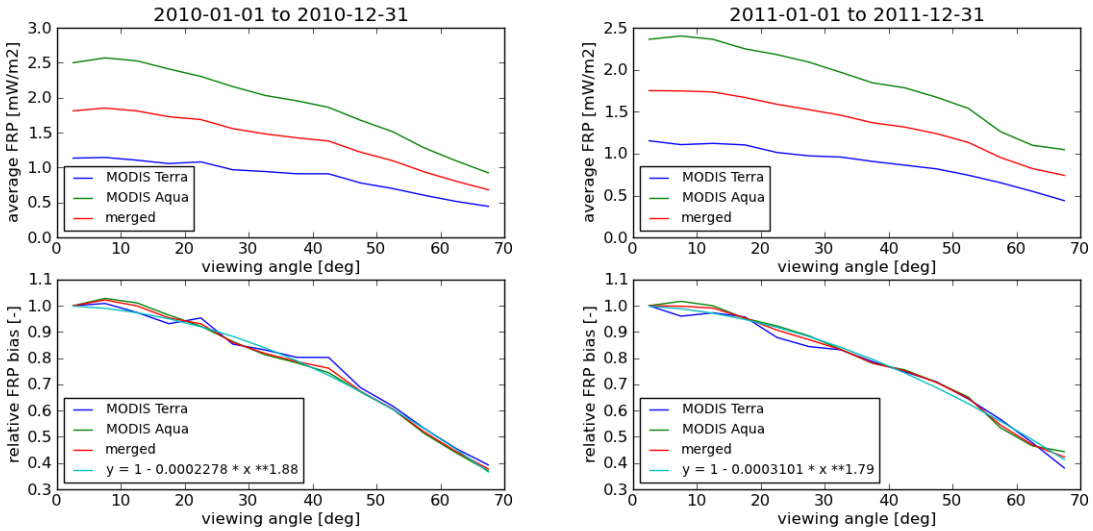

Figure 2: Annual average MODIS FRP in GFASv1.1 depending on viewing angle from Terra and Aqua for 2010 and 2011 (top) and relative bias relative to sub-satellite point observations, along with fit to bias of merged FRP (bottom).

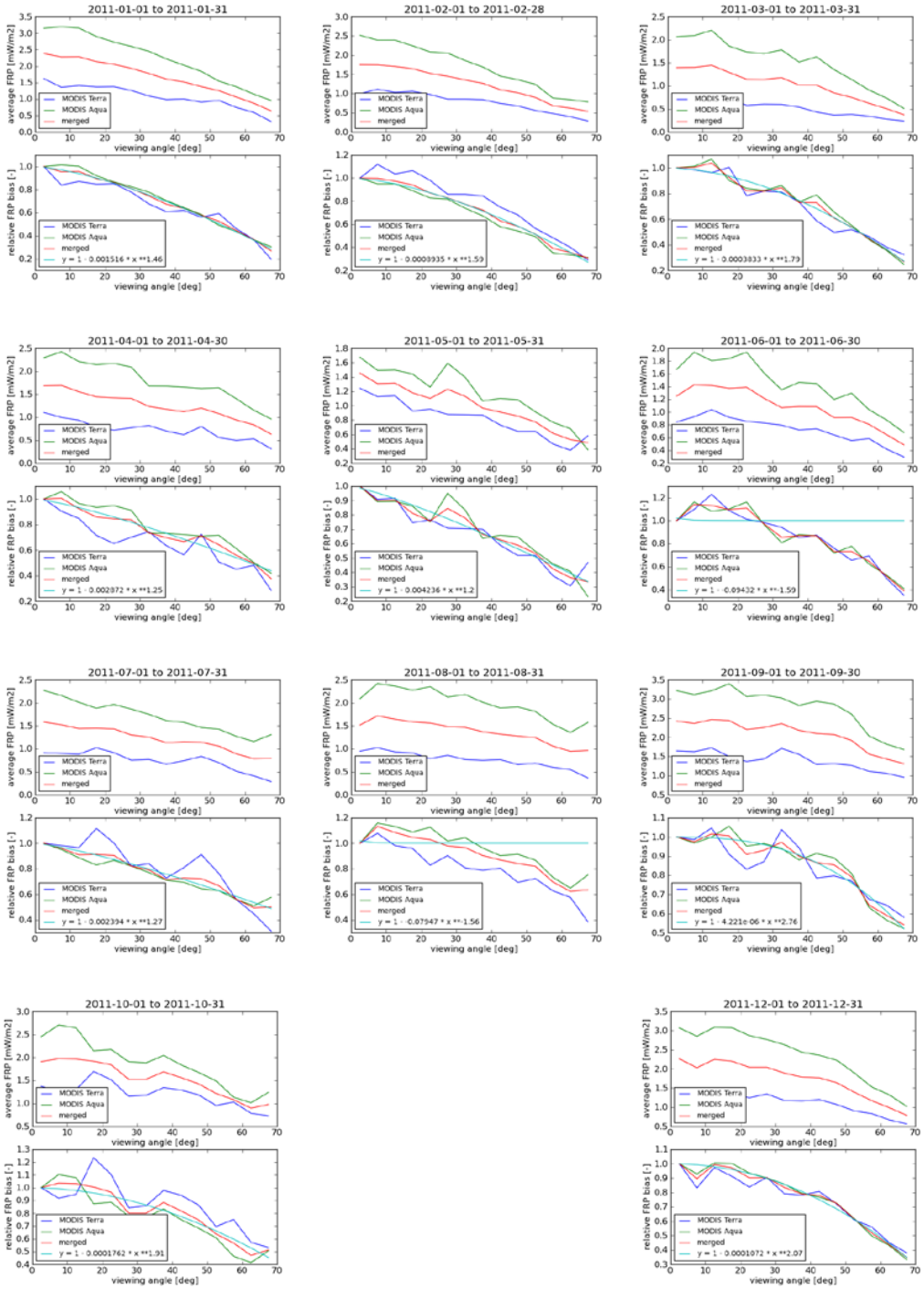

Figure 3: Monthly average MODIS FRP in GFASv1.1 depending on viewing angle from Terra and Aqua for 2011 (top) and relative bias relative to sub-satellite point observations, along with fit to bias of merged FRP (bottom).

The two instruments sample different fire distributions since they have different local overpass times. This results in the different values for the average FRP seen by MODIS aboard Terra and Aqua. However, both instruments display the same relative bias depending on viewing angle. This indicates that the derived bias parameterisation is able to isolate the instrument response from the observable signal. Figure 3 shows the

same analysis performed on monthly datasets. While the qualitative relationship is maintained throughout the year, large scatter indicates that the sample size of one month of MODIS observations is too small to characterise the instrument bias.

The dependence of the FRP underestimation at larger viewing angles on land cover type is shown in Figure 4. The underestimation displays a pronounced dependence on the land cover type. This is an indication that the underestimation may intrinsically depend on the fire type. The underlying reason may be that in areas with generally smaller fires the underestimation is affecting a larger proportion of the observed fires. For example, the underestimation is particularly strong for agricultural waste burning.

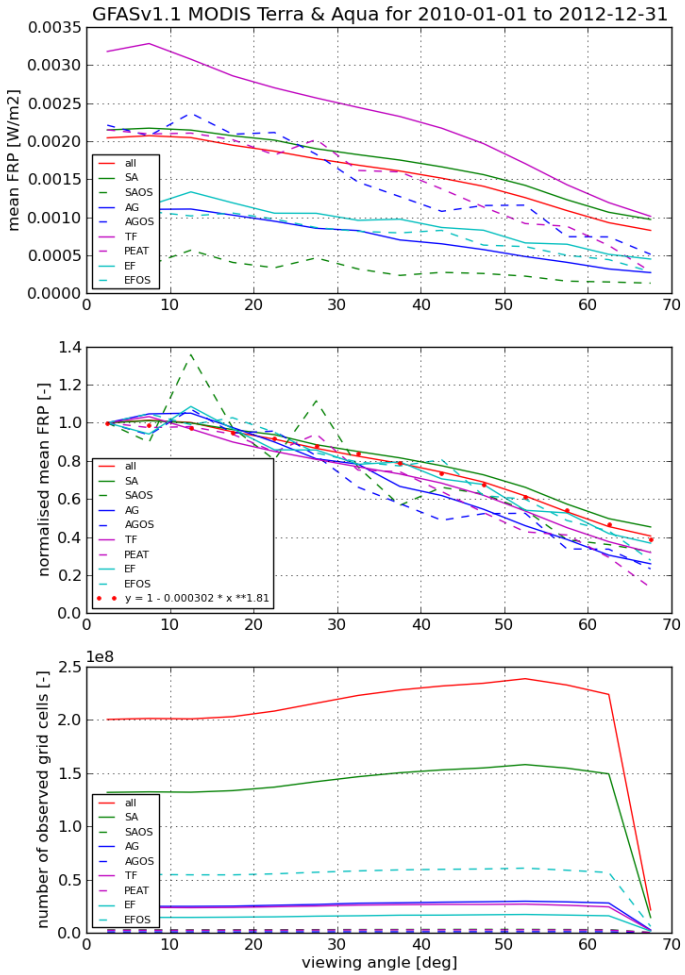

Figure 4: Average FRP (top), normalised average FRP (middle) and number of observed grid cells (bottom) in each GFASv1.0 land cover class and globally as observed by both MODIS instruments during 2010 to 2012.

In conclusion, it appears to be possible to correct the average global FRP observed in different viewing angles with a relative correction function based on two fitting parameters. However, such correction would still carry significant systematic errors in the distribution of FRP on different land cover or fire types, or possibly, fire sizes. Therefore, it appears to be necessary to characterise the dependence of the underestimation on fire type or size. We are exploring in the next section, if the underestimation can be characterised by fire size.

2.1.2 Size distribution of observed FRP

We analyse MODIS FRP observations during 2010-2012 that have been gridded with 0.1 deg and 1 hour resolution in GFASv1.1. The number of observations $N_{j,i}$ [-] are calculated for 50 logarithmically spaced FRP (j) intervals with $J+1=51$ border values ρ_j between 1 MW and 100 GW and $I=7$ equally spaced viewing angle intervals between 0 and 70 deg. Additionally, the number observations with FRP=0 are determined for each viewing angle interval and stored in the lowest FRP bin.

The FRP distribution function is calculated as

$$pdf_i\left(\ln \rho_j\right) = \frac{1}{\ln \rho_{j+1} - \ln \rho_j} \times \frac{N_{j,i}}{\sum_{j'=1}^{J} N_{j',i}}$$

A "reverse" cumulative distribution function is also calculated, that describes the probability of obtaining an observation larger than a given FRP value ρ_j:

$$f_i(\rho_j) = \frac{\sum_{j'=j}^{J} N_{j',i}}{\sum_{j'=1}^{J} N_{j',i}}$$

The average observed FRP in each viewing angle bin is calculated as

$$\overline{\rho_i} = \sum_{j=1}^{J} \frac{\rho_j + \rho_{j+1}}{2} \times \frac{N_{j,i}}{\sum_{j'=1}^{J} N_{j',i}}$$

These quantities are shown in Figure 5 for the hourly MODIS observations during 2010 – 2011. The gridded observations display an increasing detection threshold with viewing angle and a reduced observation frequency for larger FRP values. The drop-off of the average observed FRP with viewing angle is consistent with the findings of the previous section, i.e. a reduction by ~55% near the swath edge compared to near the sub-satellite track.

The increased detection threshold has two distinct effects: Firstly, grid cells that contain only fires below the detection threshold are not classified as fire observations anymore. This results in a shift of the maximum of the PDF towards larger FRP values, in a reduction of the maximal value of the CDF, and in an onset of the FRP kernel at higher FRP values. This effect cannot be directly corrected because the affected grid cells cannot be identified amongst the other grid cells with FRP=0. We will refer to this effect as "grid cell elimination" when we discuss how it could be compensated.

The second effect is a reduction of the recorded FRP value in a grid cell with at least one satellite pixel with a strong fire that is even recorded with a higher detection limit and at least one other satellite pixel with a weak fire that is recorded only with low detection limit. This effect leads to a reduction of the PDF, CDF and kernel values. It can be corrected on average because such grid cells are detected in both the low-viewing angle reference observations and the higher-viewing angle observations that are to be corrected. The correction should have the effect of making the distributions for the large FRP

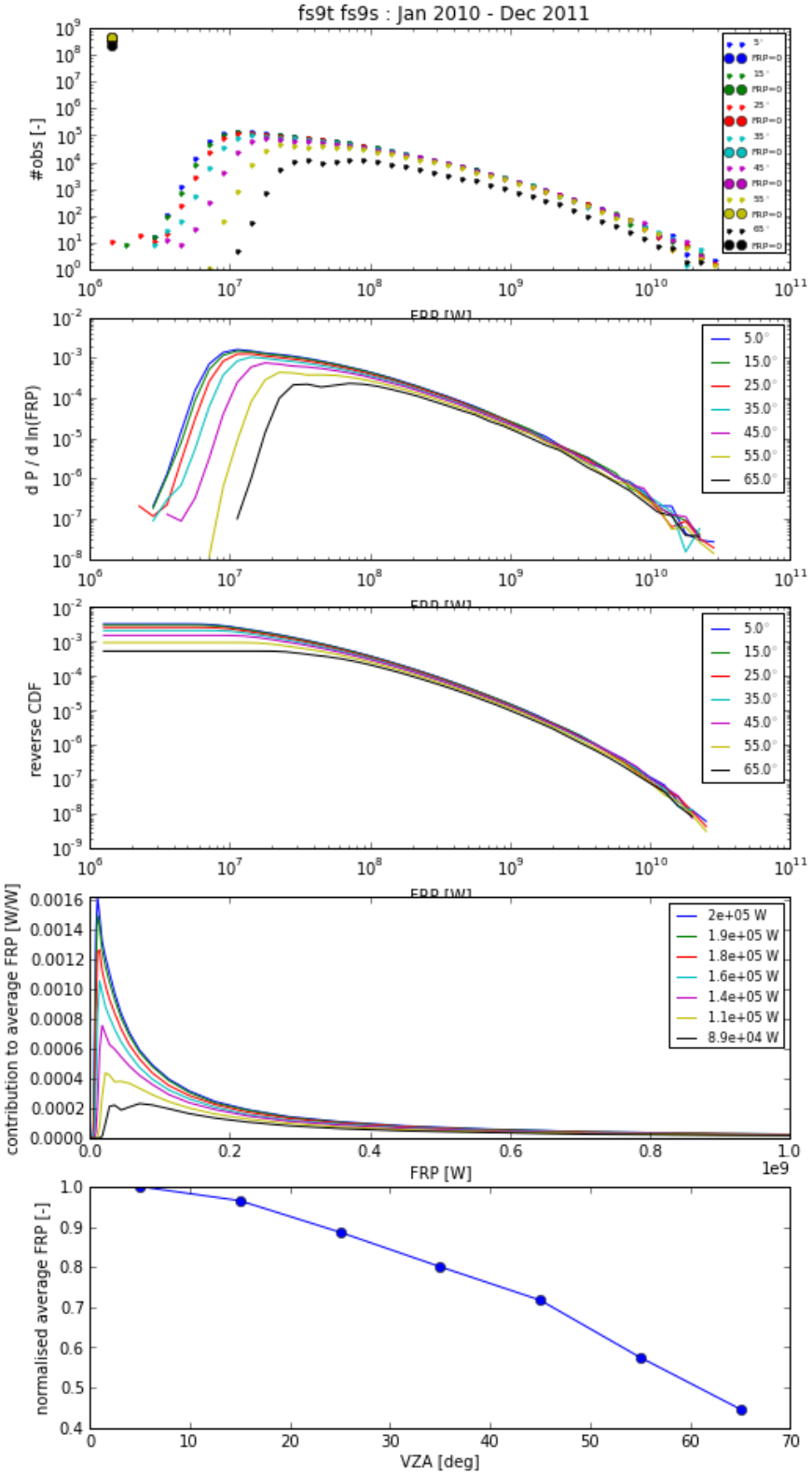

Figure 5: Statistical properties of gridded MODIS FRP observations during 2010 and 2011 depending on viewing angle (VZA): number of observations in each FRP bin, FRP probability distribution function, "reverse" cumulative distribution function, kernel of integral for average FRP calculation, relative average FRP depending on viewing angle (top to bottom).

values identical for all viewing angles. In particular, the correction function ϱ needs to shift the CDF for each viewing angle rightward such that it coincides with the CDF observed at the sub-satellite track (for larger FRP values):

$$f_i(\rho) = f_0(\varrho)$$

Since the cumulative distribution functions f_0 is monotonous, it can be inverted to calculate the correction functions:

$$\varrho_i(\rho) = f_0^{-1}(f_i(\rho))$$

These correction functions are depicted in Figure 6. It appears that the functions are approximately made up of two straight lines in log-log space i.e. $\varrho_i(\rho)/\rho$, exhibits a dependency of the type

$$\varrho_i(\rho) = 1 + e^{a - b \log \rho} + e^{c - d \log \rho}$$

for each viewing angle bin.

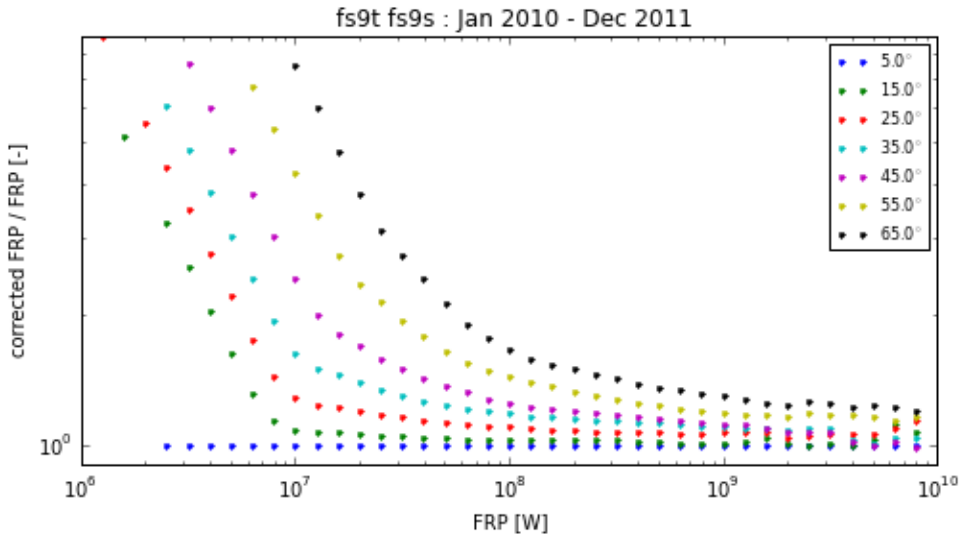

Figure 6: FRP correction functions calculated from gridded MODIS observations in 2010 - 2011.

In order to test the effectiveness of the correction functions, they are applied to the number of observations, i.e. the FRP positions are adapted according to the correction functions shown in Figure 6 and then the distributions are recalculated. The resulting values are shown in Figure 7 and confirm that the PDF, CDF and FRP kernels become independent of the viewing angle above certain threshold values as intended. The average FRP is only weakly dependent on the viewing angles < 40 deg. For larger viewing angles, the underestimation is less pronounced than without correction, but still significant.

In order to test the applicability on an independent data set, the corrections derived for 2010-2011 are applied to the MODIS observations of 2012, cf. Figure 8. It shows the same behaviour as for 2010-2011. Therefore, the correction approach appears to yield the correct distribution of fires as far as they are detected on the GFAS grid.

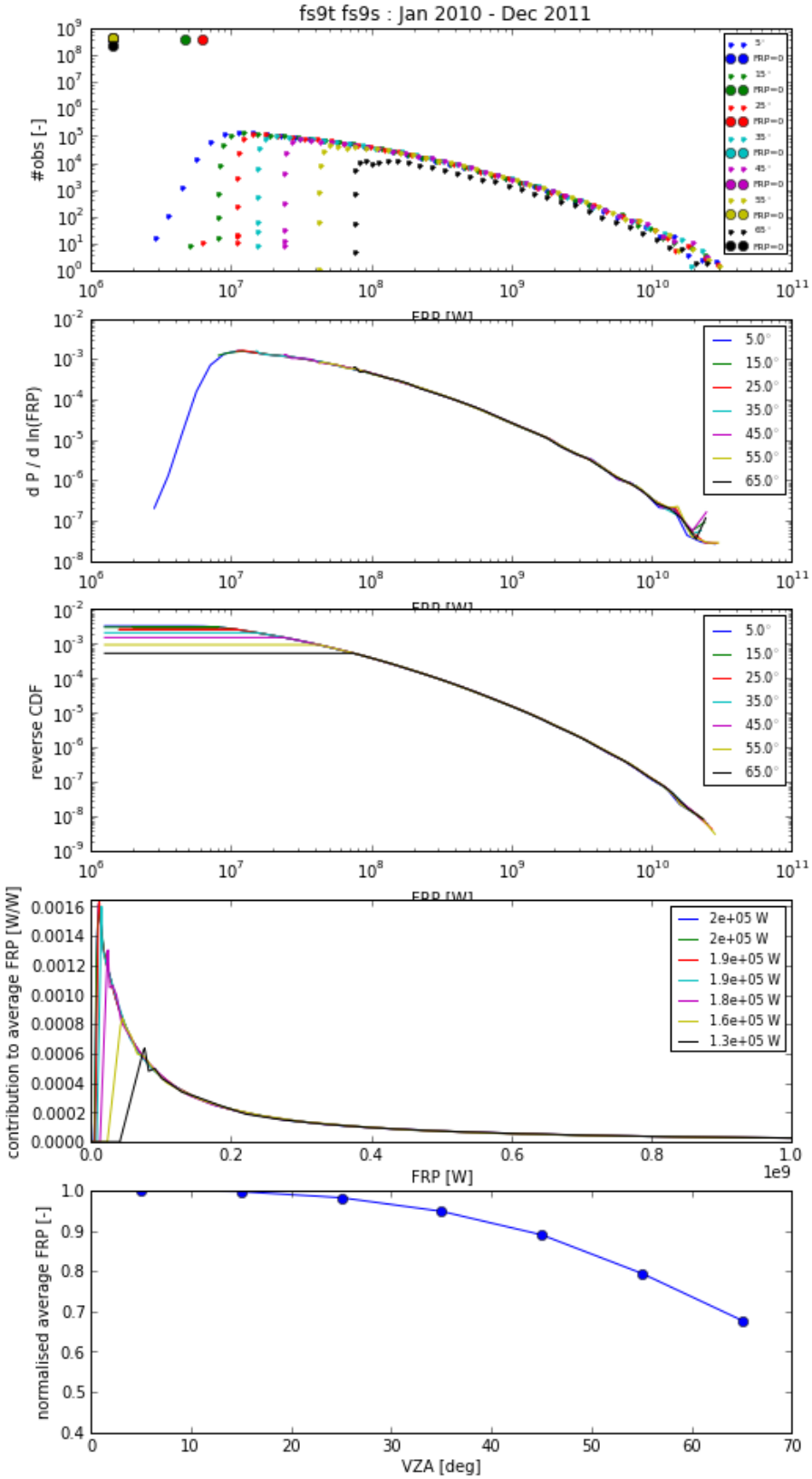

Figure 7: As Figure 5, but with corrected FRP.

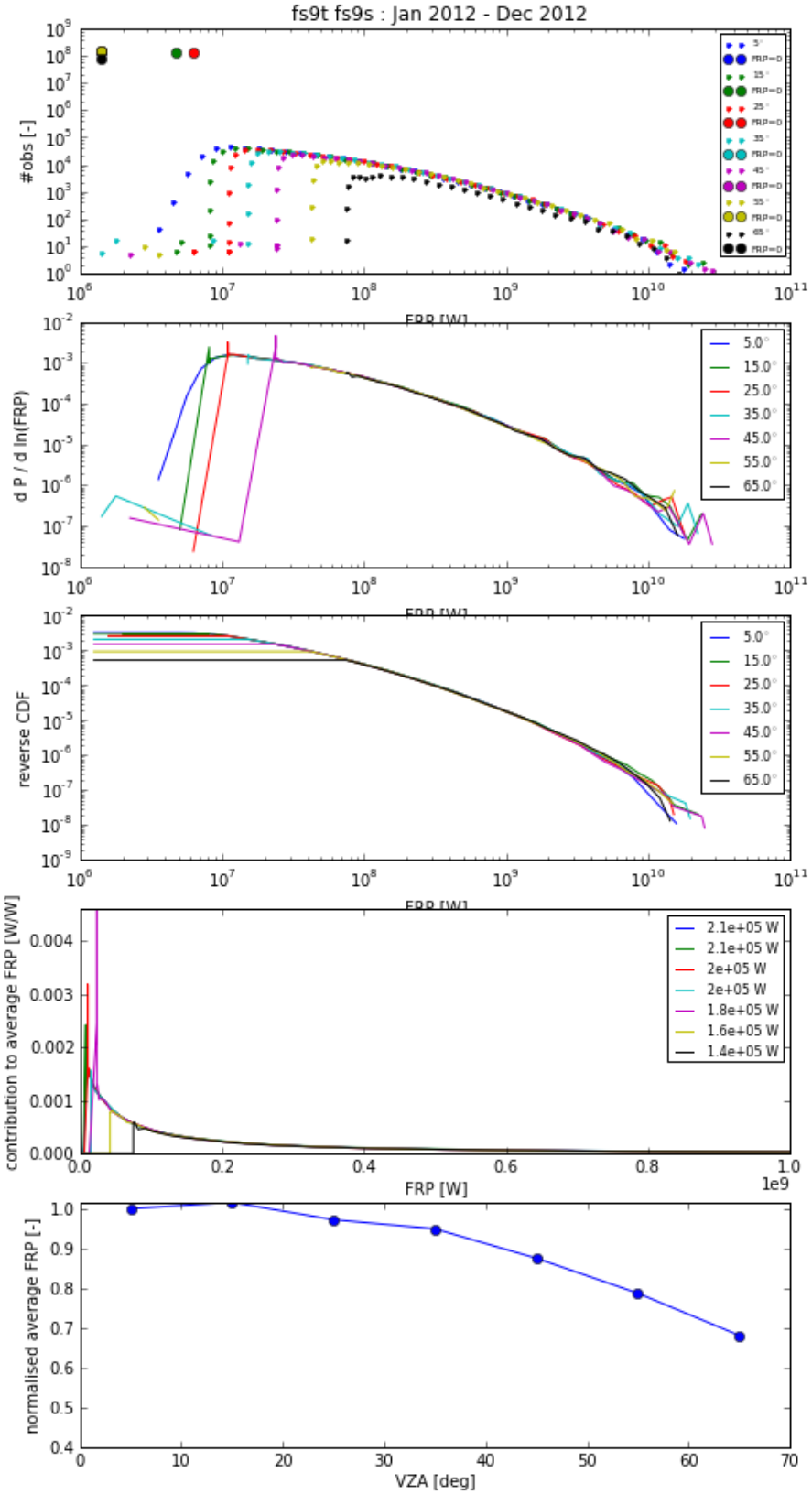

Figure 8: As Figure 5, but for 2012 and with corrected FRP.

There remains a significant viewing-angle dependent underestimation due to the "grid cell elimination" where all fires in a grid cell fall below the satellite pixel detection threshold. It cannot be corrected directly. Instead, we propose to

1. represent the corrected grid cell detection threshold in observations variance of the FRP data assimilation, or

2. compensate for it by increasing the FRP of observed fires by more than is realistic.

The later approach might be done by

a. deriving the correction above on a coarser grid than 0.1 deg, or

b. multiplying all corrected FRP values by a viewing-angle-dependent factor as suggested in the previous section, or

c. adding a viewing-angle-dependent FRP offset, which would affect smaller FRP values more than larger ones, i.e. target regions with low fire intensity. An example is given in Figure 9. It exhibits an unrealistic distortion of the PDF and CDF of fire intensities. (A similar corrective effect could be achieved with a multiplicative correction factor that is parameterised as 1/*frp*.)

Figure 10 and Figure 11 show the original and corrected distributions of MODIS observations gridded with 0.5 deg and 1 deg resolution, respectively. The average FRP values observed near the swath edges are only 13% and 5% below the values observed near the sub-satellite track, respectively. 5% is well below the inaccuracy of fire emission estimation. Therefore, it seems feasible to apply a multiplicative correction that depends on viewing angle and FRP observed at 1 deg resolution to GFAS. This will mostly affect regions with low-intensity fires, e.g. agricultural waste burning, where detected fires will be over-estimated somewhat to compensate for missing fire detections in the vicinity, i.e. with typically up to ~100 km distance.

In conclusion, the following procedure for the correction of the viewing angle-dependent bias of the MODIS FRP products in the operational production system is recommended:

1. regrid FRP observations with 0.1 deg resolution to 1 deg resolution

2. determine FRP- and VZA-dependent correction factor from

    a. pre-calculated look-up-table of ϱ/ρ, or

    b. a parameterisation of the look-up-table

3. apply correction factor to FRP with 0.1 deg resolution

4. increase relative variance of FRP observation errors in the GFAS assimilation system according to detection threshold of corrected FRP values at 0.1 deg resolution.

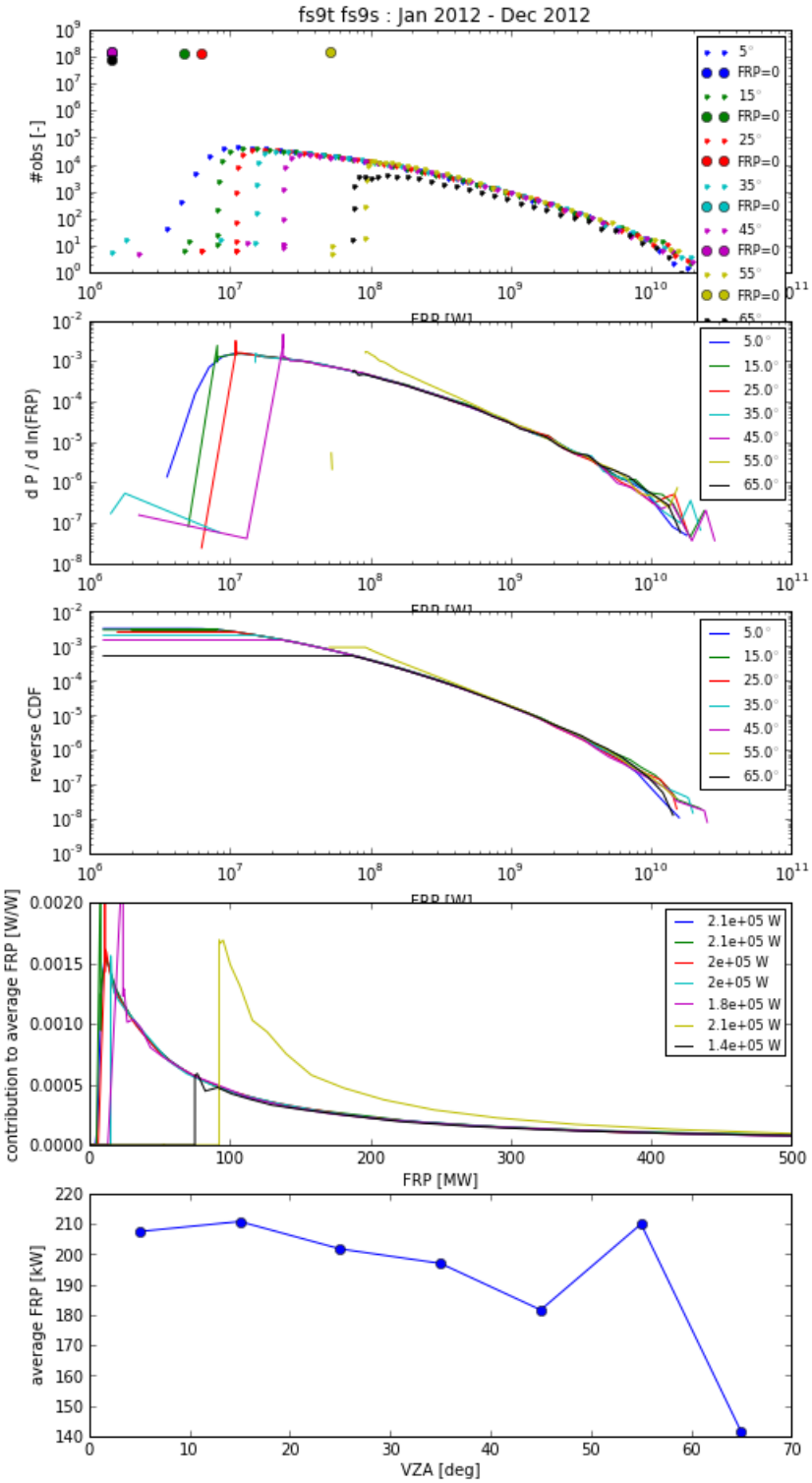

Figure 9: As Figure 7, but with additionally 50 MW added to all fire observations between 50 and 60 deg, and absolute average FRP per grid cell instead of the relative one in the bottom panel.

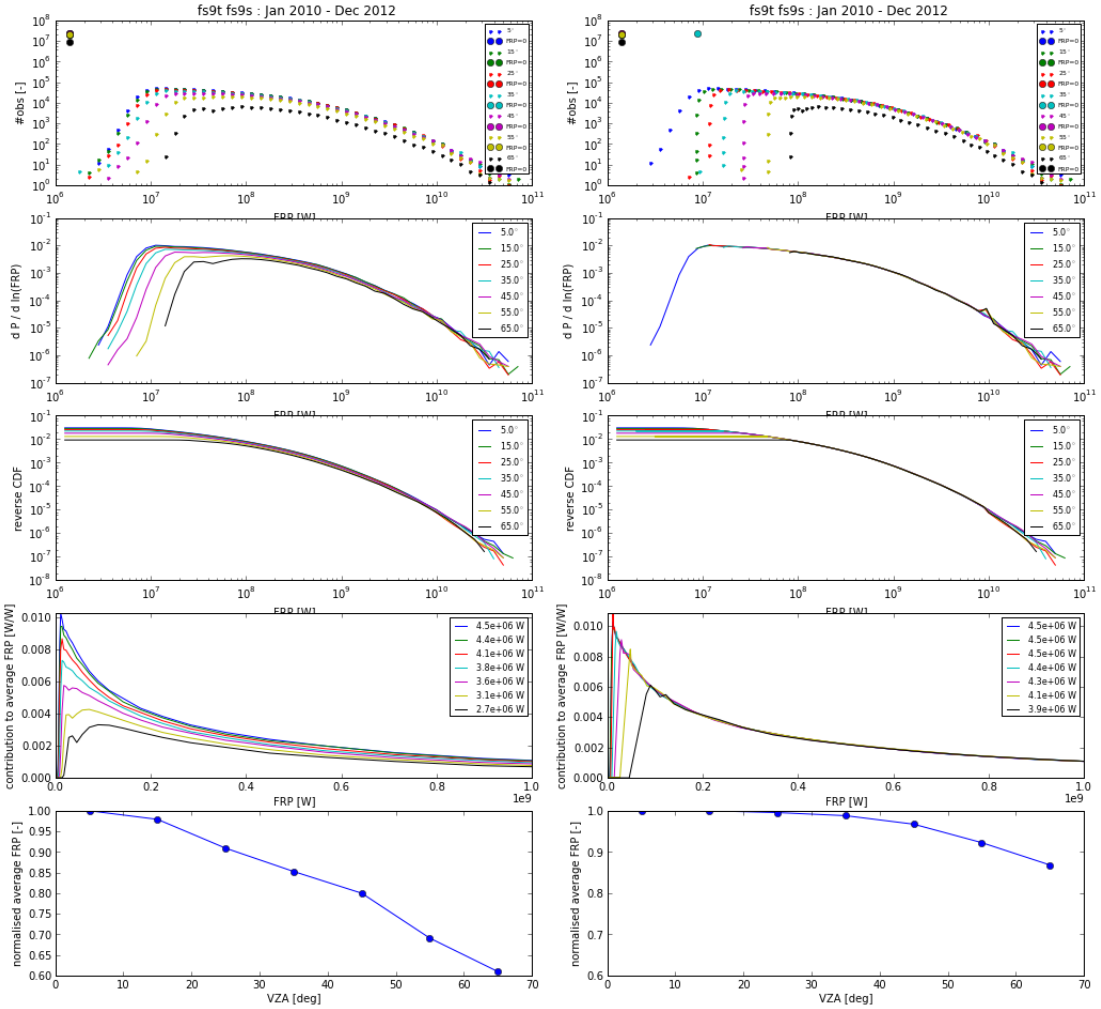

Figure 10: Distributions for three years of MODIS FRP observations with 0.5 deg resolution (left) and corrected (right).

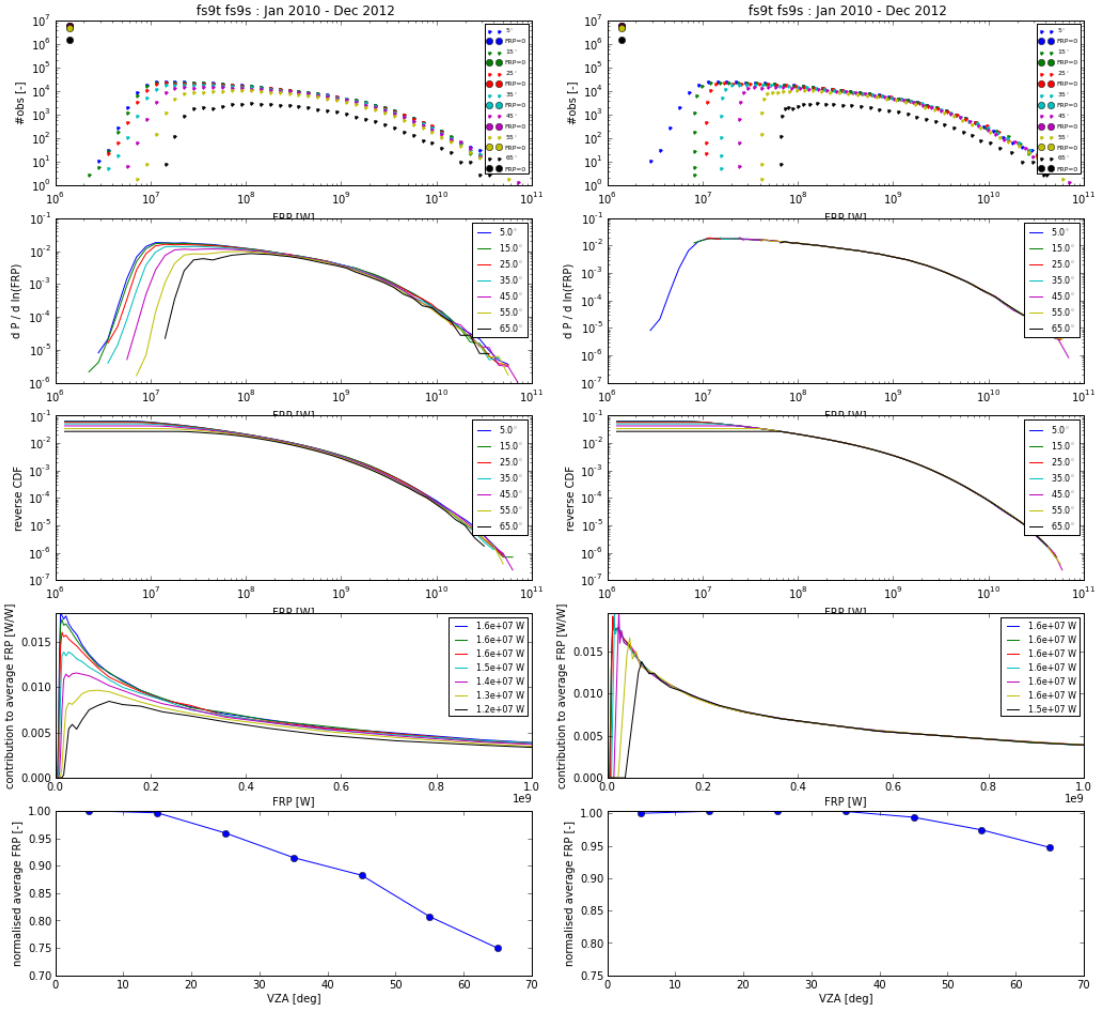

Figure 11: Statistics for three years of MODIS FRP observations at 1 deg resolution (left) and with corrected FRP (right).

2.2 Temporal resolution

2.2.1 Merging of GEO observations

The consistent merging of FRP observations from polar orbiting (MODIS) and geostationary instruments (SEVIRI, GOES) remains a task for which no solution has been found by any of the interested research groups worldwide. Thus attempts to use the geostationary FRP observations for emission estimation remain qualitative rather than being quantitatively useful, e.g. Zhang et al. 2012. Near the edges of the satellite disks, the FRP products may contain severe omission errors, e. g. SEVIRI FRP near Moscow during the fire event of 2010, and also severe commission errors, e. g. spurious SEVIRI FRP over the Amazon as seen in the early GFAS version 0. The geostationary FRP observations from SEVIRI and the GOES instruments generally have a larger detection threshold than those from the MODIS instruments due to larger satellite footprints, cf. Hyer et al. 2013, Roberts et al. 2011. As with the MODIS instruments, the detection thresholds vary with viewing angle. However, each location is observed with a fixed viewing angle. Therefore, the FRP products from geostationary instruments have relative biases that vary in space (different regions) and time (different parts of the diurnal cycle and fire season). The accuracy of the geostationary FRP products has not been comprehensively characterised, partly due to a focus on Africa of

the vast majority of investigations that use SEVIRI. The few known attempts to characterise the biases as functions of space and time have failed (e.g. Kaiser et al. 2013). Therefore, cross-calibration with independent observations will be needed.

As a preliminary test, the consistency of MODIS and SEVIRI fire observations is assessed for different global grid resolutions. For this analysis, the original GFASv1.1 data with 0.1 deg resolution is aggregated in coarser grids. Figure 12 shows that only for GFAS resolutions > 0.5 deg, the fire patterns observed by SEVIRI and MODIS are sufficiently consistent for a meaningful characterisation of the bias of the SEVIRI observations. To be on the safe side, the following analysis will be performed with 1 deg resolution, which is also in line with the resolution of the proposed correction for the MODIS bias correction, cf. Section 2.1.2.

The discrepancy on viewing angle at finer resolutions might also partially be introduced by the assignment of SEVIRI observations with footprints ≥ 25 km^2 to individual grid cells. This could ultimately only be resolved by working on the native SEVIRI observations grid.

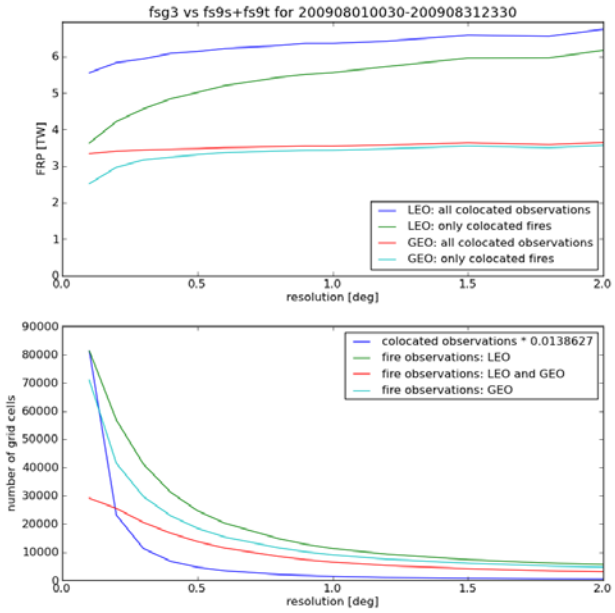

Figure 12: Top panel; Total FRP in MODIS observations that are co-located with valid (FRP≥0) SEVIRI observations and with actual fire observation (FRP>0) of SEVIRI, and the corresponding values for SEVIRI, all for different resolutions. Bottom panel; Numbers of grid cells with (blue) co-located valid observations of MODIS and SEVIRI, (green) fire observations by MODIS, (magenta) fire observations by SEVIRI, and (red) fire observations in both.

The results of the preliminary study are shown in Figure 13 to Figure 15. Figure 13 displays the number of co-located observations in various bins of SEVIRI FRP, MODIS FRP, their ratio (the desired correction factor), the local time and the distance from the sub-satellite point (a proxy for the viewing angle). Many important details are hidden because of the large ranges of the values. Therefore, Figure 14 shows the same values normalised within each bin on the x-axis. Thus the columns can be interpreted as conditional observation frequencies, or probabilities, for given the given values on the x-axis. The top left panel shows

a correlation of MODIS and SEVIRI FRP, mostly for small MODIS FRP values. The relationship becomes clearer in the top middle panel, which shows the ratio of SEVIRI FRP over MODIS FRP depending on MODIS FRP: The underestimation by SEVIRI is systematically more severe for smaller fires and it becomes almost constant, albeit with large scattering, for larger FRP values. This is a qualitatively similar dependence on FRP as discovered for the MODIS correction in the previous section.

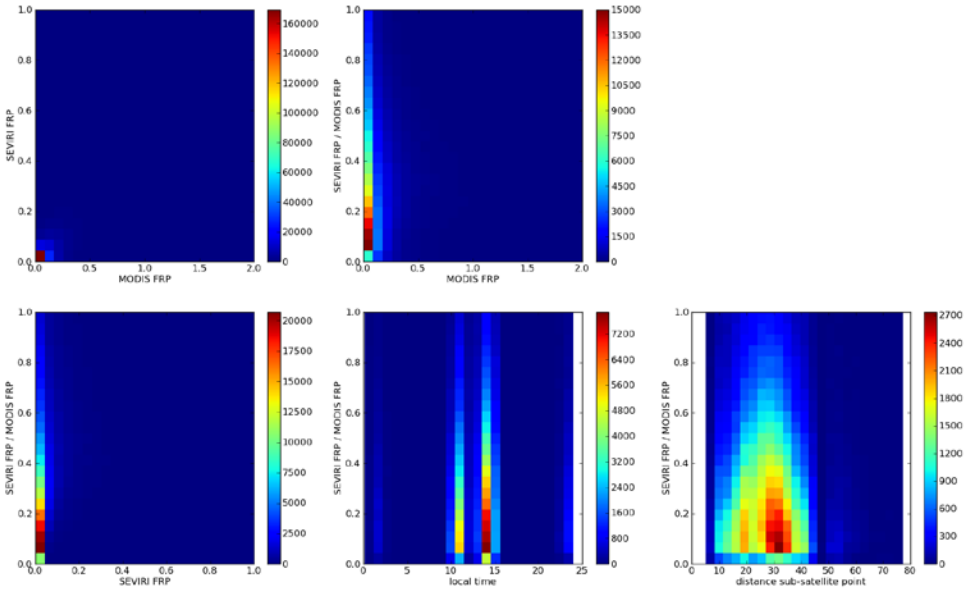

Figure 13: Number of colocated -within 1-hour time slot- FRP observations by MODIS and SEVIRI (top left). Distribution of observed FRP ratio for different MODIS FRP values (top middle). Distribution of observed FRP ratios for different SEVIRI FRP values (bottom left). Distribution of observed FRP ratio over local time (bottom middle). Distribution of observed FRP ratio over distance to SEVIRI sub-satellite point (bottom right))

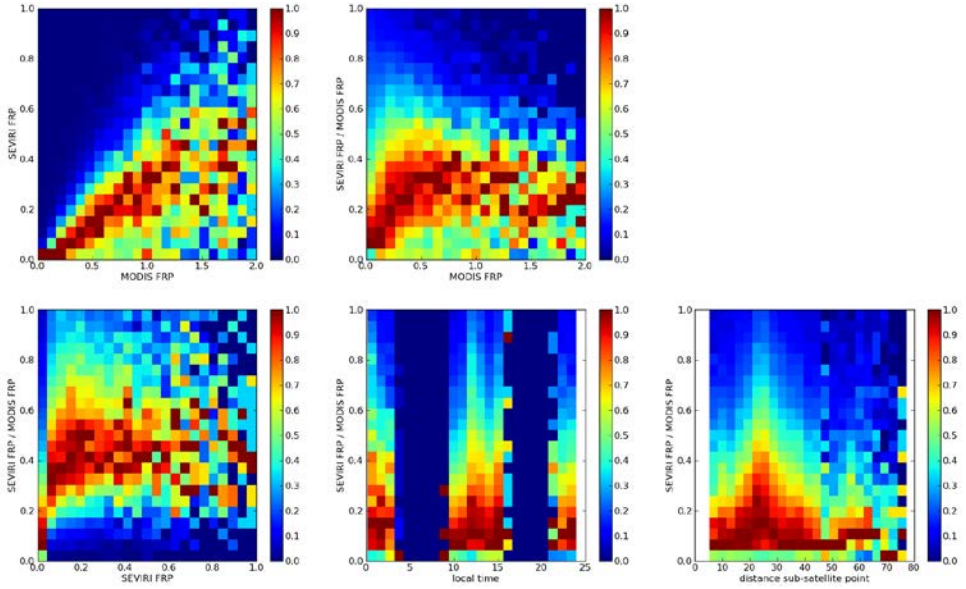

Figure 14: Same as previous figure but each column is normalised to its maximal value.

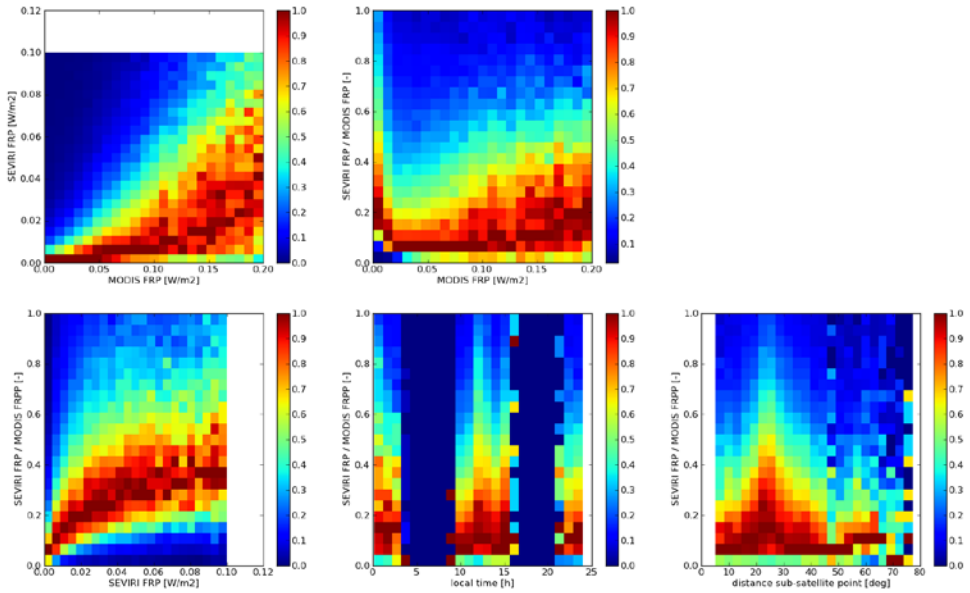

Figure 15: Same as previous figure but x-axis zoom into small FRP values.

Figure 15 provides a zoom into the regions with smaller FRP values. The bottom left panel displays a systematic dependence of the ratio of SEVIRI and MODIS FRP also on the SEVIRI observations. This proves the fundamental possibility of correcting the SEVIRI bias without the availability of co-located MODIS observations.

The figures do not show a systematic dependence of the SEVIRI FRP bias on local time, which is somewhat unexpected because the fire size distribution is expected to vary with local time. Interpretation of the dependence on distance from the sub-satellite point is inconclusive because effects from the regional distribution of fire types and the viewing angle of the SEVIRI observations are mixed.

Since obtaining consistent reference observations is a prerequisite to characterising and correcting the geostationary observation, the developments in MACC-II have first focused on the correction of the viewing angle dependence of the detection thresholds within the MODIS observations, see previous chapter. Furthermore, the functional form of the detection threshold correction derived for MODIS, depending on viewing angle and gridded FRP value, may be used as model for the detection threshold correction to be derived for SEVIRI and the GOES instruments.

A parameterisation for the bias correction of MODIS observations with different viewing angles has been suggested in the previous section. For SEVIRI observations, the same functional dependency on viewing angle and FRP may be assumed because they employ the same measurement principle as MODIS. However, the values of the parameters cannot be determined with the same methodology because different fire regimes are observed with different viewing angles. Instead, we will perform a parameter fit procedure that is constrained by co-located hourly gridded observations of MODIS (corrected) and SEVIRI.

2.2.2 Representation of the diurnal cycle of fires

With the upcoming GFAS update, the daily time resolution shall be changed to hourly, increasing suitability for atmospheric models. For regions where geostationary satellites are available this is likely to result in a better representation of fire activity during the day, and daily FRE estimation will be estimated using geostationary high temporal resolution observations scaled to MODIS. For large parts of the world geostationary observations are however not available and the daily fire activity has to be described using the typically four daily MODIS observations.

Therefore, there is a need to explore how diurnal fire activity can be described best at an hourly resolution using MODIS data. On a regional scale, it has been demonstrated that a Gaussian function describes the diurnal cycle well (e.g., Vermote et al., 2009; Ellicott et al., 2009). Here, we present some preliminary results on the potential of a Gaussian function to describe daily fire activity in northern Africa at 1° resolution. For a start, we use SEVIRI continuous (15-min interval) data and see how SEVIRI data at MODIS overpass times is able to predict the complete time-series.

A Gaussian function

In recent literature it has been shown that daily fire activity generally shows a diurnal cycle that can be described by a Gaussian function:

$$RP(t) = FRP_{peak} \times \left(b + e^{-\frac{(t-h)^2}{2\sigma^2}} \right)$$

Where FRP_{peak} is the daily peak in FRP (or amplitude), h the peak hour of fire activity, b the base or minimum daily FRP and σ controls the width of the curve. Vermote et al., 2009 found that the four MODIS observations provide information on the parameters used within the Gaussian equation and determined regional values. This study was however based on monthly mean values and large study areas. We found that when studying 1° daily fire activity the MODIS daytime observations are related to FRP_{peak} and night-time observations are related to b. However, the moment of peak burning and σ are not related to daily MODIS observations. For these parameters, regional estimations depending on, for example, vegetation type should be made. Geostationary satellites can be used to derive optimal parameters for the Gaussian function and to study causes of their spatial variation. Figure 16 shows that hour of peak burning at this scale seems to be related to the fire intensity, where large intense fires are likely to continue longer and peak later, and σ is relatively constant for northern Africa.

To set up the Gaussian model for northern Africa, the hour of peak was expressed as a function of longitude (constant at local time) and a mean regional σ was used (σ = 8.5). FPR_{peak} was expressed as a function of the daily sum of MODIS observations (FRP_{peak} = 0.77*($Terra_{1030}$+$Aqua_{1330}$)+22), and b is was not included yet as this factor is expected to be mostly important when studying forest and peat fires, that generally continue in the night. Figure 17 shows the results for a study pixel, for this particular pixel the Gaussian function describes daily fire activity well. Figure 18 shows a scatter plot of daily estimated FRE using the current GFAS assumptions (left) and by the Gaussian function (right), results are encouraging as the slope between actual FRE and estimated FRE is much higher (0.91) using the Gaussian than using the GFAS assumptions (0.65; a slope of 1 is perfect).

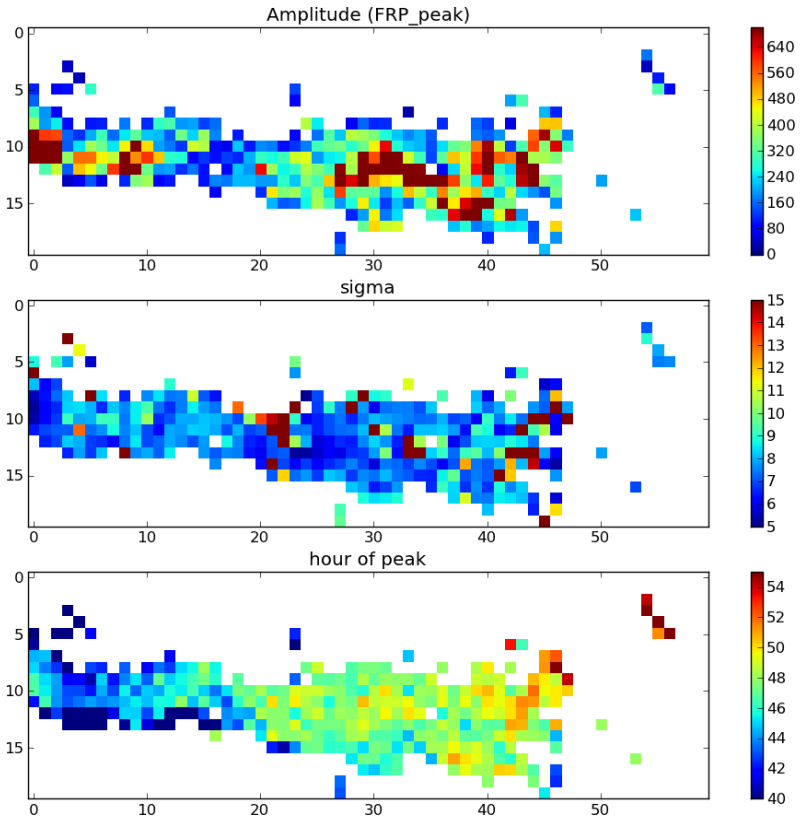

Figure 16: Mean daily amplitude (FRP_{peak}), σ and h (hour of peak activity) for northern Africa. The amplitude (FRP_{peak}) is expressed in Watt m^2 and σ and hour of peak in 15-min SEVIRI intervals (e.g., 4 is one hour). This is an optimal fit for 15 min interval SEVIRI data.

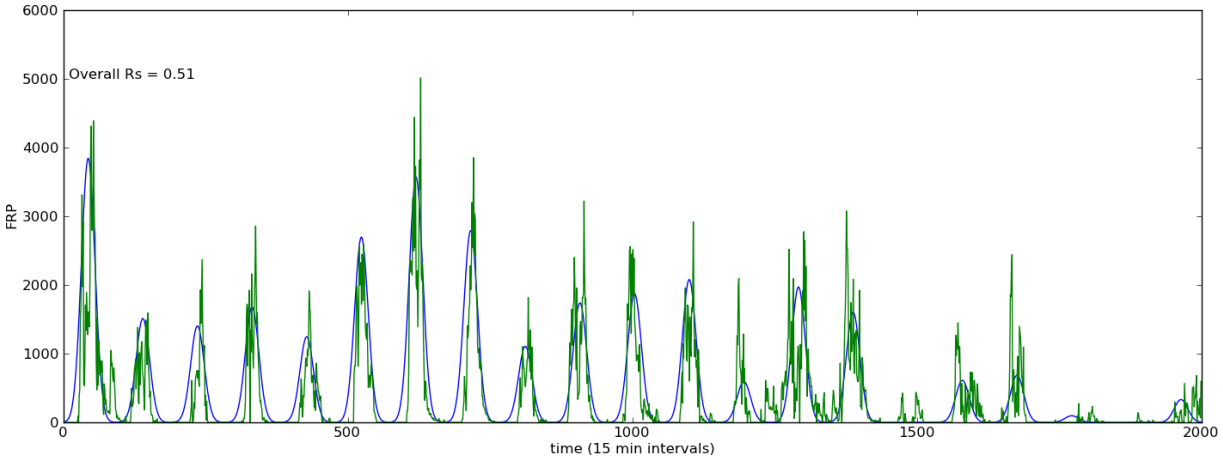

Figure 17: An example (first 20 days) of a fitted Gaussian function for a 1°x1° study region in Northern Africa (h = 43.5, σ=8.5 and FRP_peak = function of MODIS observations, b = 0).

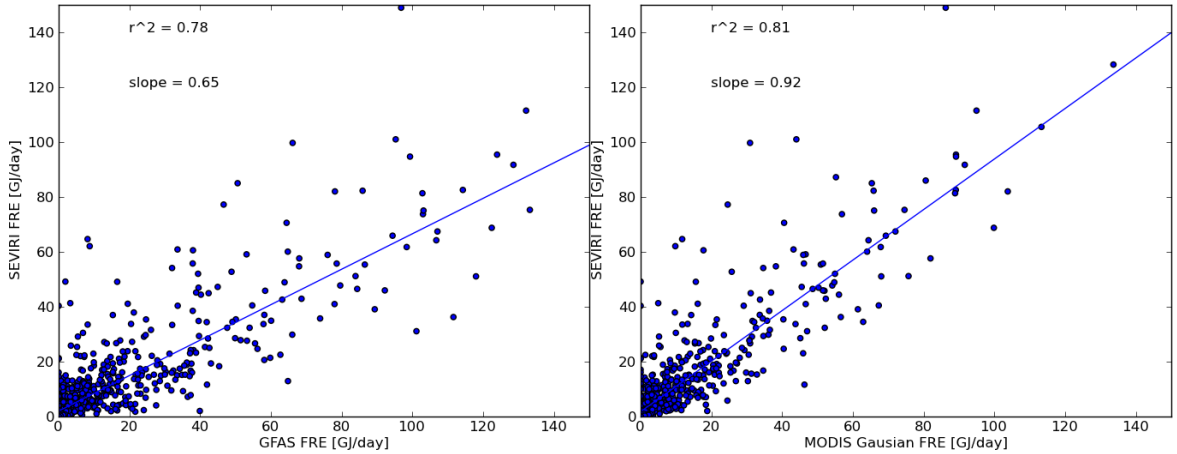

Figure 18: Left: Relation between daily SEVIRI FRE and FRE estimated by GFAS (using SEVIRI data at MODIS overpass times only). Right: A scatter plot showing daily SEVIRI estimated FRE and FRE estimated by a Gaussian function (h = 43.5, σ=8.5, b = 0, $_{FRP\_peak}$ = 0.77(Terra$_{1030}$+Aqua$_{1330}$)+22).*

Finally, we show a map of estimated mean daily FRE for northern Africa (Figure 19). As already seen in Figure 18, using the GFAS assumptions structurally overestimates FRE for the region, and the Gaussian function seems to be an improvement.

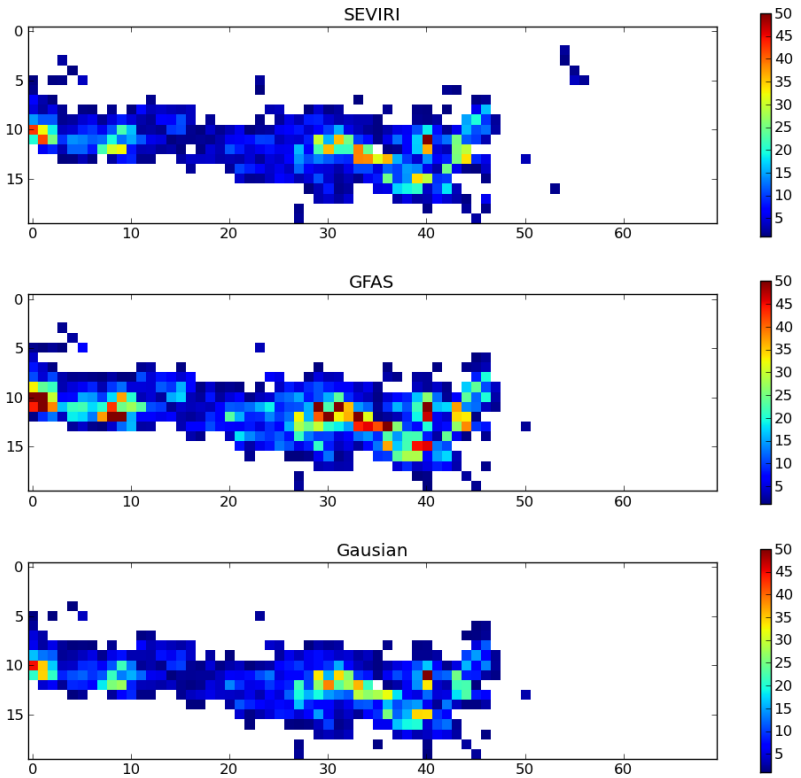

Figure 19: Gridded mean daily FRE, as estimated by SEVIRI, GFAS and the Gaussian function.

Global estimation of Gaussian parameters at 0.1° spatial resolution

Preliminary results suggest that using a Gaussian function can improve daily FRE estimations at a 1° spatial resolution when using MODIS observation only for northern Africa. The next GFAS version will however use a 0.1° spatial resolution and global parameterization is needed. Figure 20 shows that a Gaussian function also has potential to describe savannah and forest fires at a 0.1° resolution. It is however also observed that MODIS observations are not always representative for the daily fire activity. Additionally an error in the SEVIRI data seems to be present in the data for Greece in the afternoon.

In the coming months we will further explore if a Gaussian or related function driven by MODIS observations is a realistic option to represent fire activity at a 0.1° daily resolution globally. For northern Africa, we concluded that using the parameters derived from SEVIRI and a Gaussian function improves daily FRE estimations using MODIS observations only (at 1° resolution). For regions that are not monitored by geostationary satellites however we cannot determine the best parameters of the Gaussian so easily. Therefore we will use data from GOES and SEVIRI to study how parameters of the Gaussian are related to the updated biomes and fire types used in GFAS (see Sect. 3.1) and physical aspects of the fire regime, like fire size. While parameters FRP_{peak} and b, can be estimated from the four daily MODIS observations, σ and h will be estimated using these globally derived static maps. The only remaining biomes that cannot be observed well by geostationary satellites (located above the equator) are boreal forest and tundra. Polar orbiting satellites like Terra and Aqua often provide about double the daily observations in these regions close to the pole, and allow therefore a better characterisation of daily fire activity and will be used to find unknown parameters of the Gaussian for these regions.

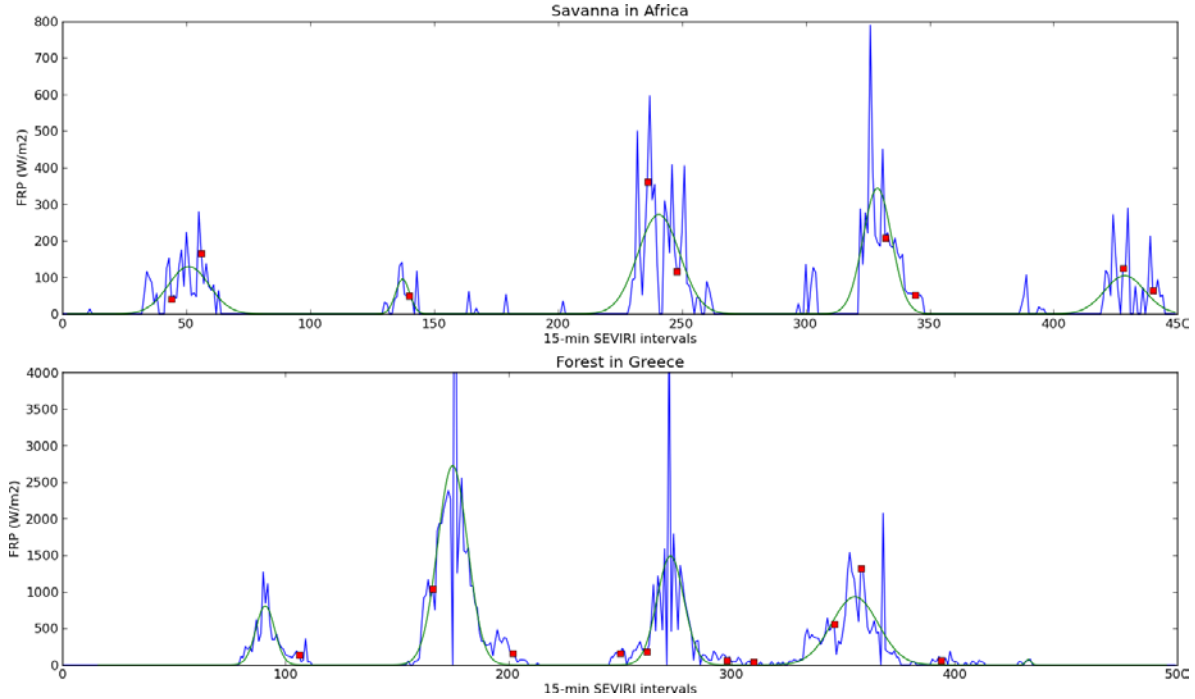

Figure 20: Example of fires as observed by SEVIRI (blue), MODIS (red squares), and an optimal fitted Gaussian (green). Two study regions are shown: above, active fires in a 0.1° grid cell in the African savannah, and below active fires in a 0.1° grid cell in a forest of Greece.

2.3 Operational status

2.3.1 Short-term resilience against failure of MODIS

Terra has been active since 1999 and Aqua since 2003. As the recent failure of ENVISAT in April 2012 showed, a sudden breakdown of a satellite is a very real possibility. As an adequate replacement data doesn't yet exist, contingency plans need to be made in case of a failure of Terra or Aqua.

Figure 21 exhibits a constant ratio for annual global average FRP observed from MODIS aboard Terra and Aqua. If this ratio is also sufficiently constant for regional monthly observations (after swath-bias correction), then each of the MODIS instruments could be scaled towards the "merged" dataset as an additional "bias correction" for the daily MODIS observation. Then we could live with the sudden death of one of the MODISes, as processing the scaled FRP data from a single satellite wouldn't entail a large bias as compared to processing data from both satellite.

Despite this being directly applicable only to daily average processing, not GFAS with 1-hour resolution, it would be reassuring to have this kind of resilience until we switch to hourly resolution. Also, MOD14 data from Terra is available from February 2000, while Aqua data is available only from July 2002, which is why the GFAS emissions are currently available from 1st of January 2003 onward. Devising a method to run GFAS only with Terra input data would then allow us to extend the GFAS data archive to the years 2000, 2001 and 2002.

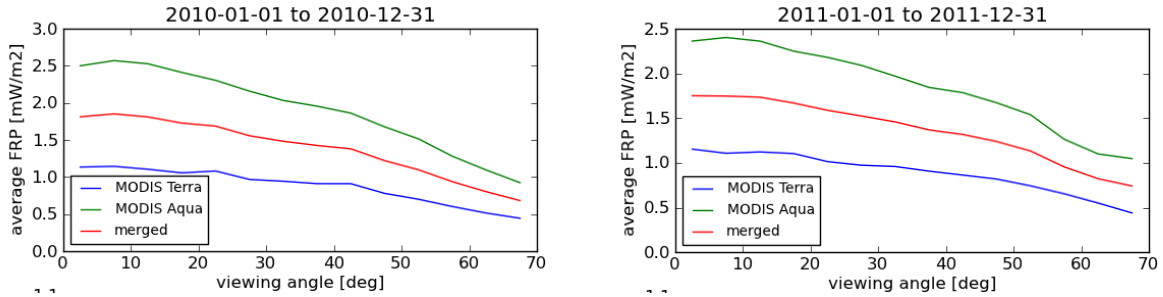

Figure 21: Average FRP for Terra (Blue), Aqua (green) and merged Terra-Aqua (red) as a function of viewing angle, for 2010 (left) and 2011 (right).

The possibility to scale either Aqua or Terra towards the merged observations of Terra and Aqua was tested using a learning dataset of gridded daily FRP from 1/1/2003 to 31/12/2011. The correlations between Terra/Aqua and the merged data was checked for every 2x2 degrees tiles for which more than 400 fires were observed in the period. Linear regression and several kind of non-linear regression formulae were tried out on these samples, and for most of the case a good degree of correlation was reached, as shown by Figure 22.

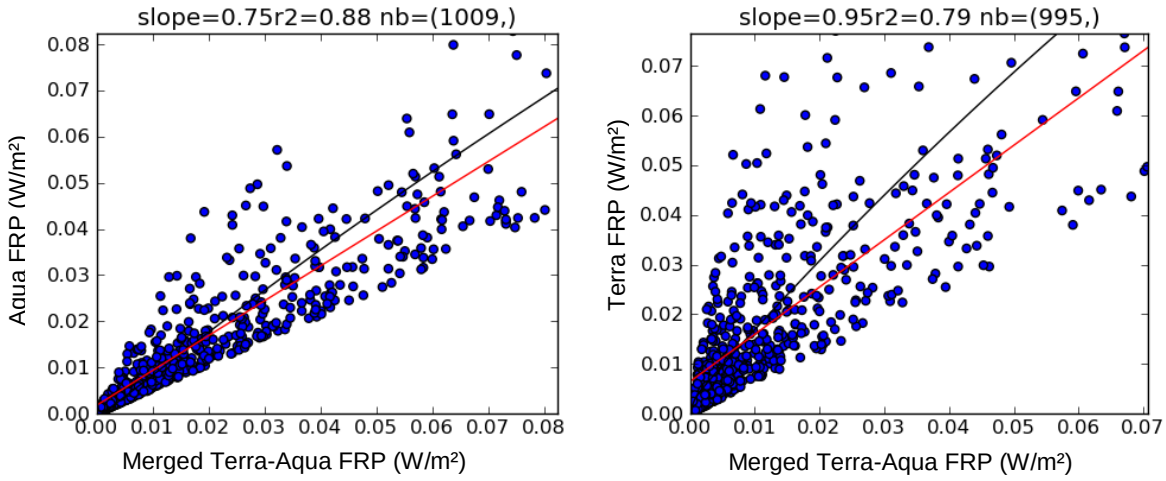

Figure 22: Scatterplot of gridded daily FRP (W/m²) for an area comprised between 138 and 140 degrees of longitude and 28 and 30 degrees of latitude. The X axis shows the values for Aqua (left) and Terra (right), the Y axis shows the values for merged Terra-Aqua. In red is a linear regression between the two datasets and black a polynomial regression. The size of the data set and the squared correlation coefficient between X and Y are also indicated.

Linear and nonlinear regressions had different advantages: the nonlinear regression was in general better, but less stable for values of FRP that are very large or small. A good example of how non-linear regression can provide better values and diverge is given in Figure 23:

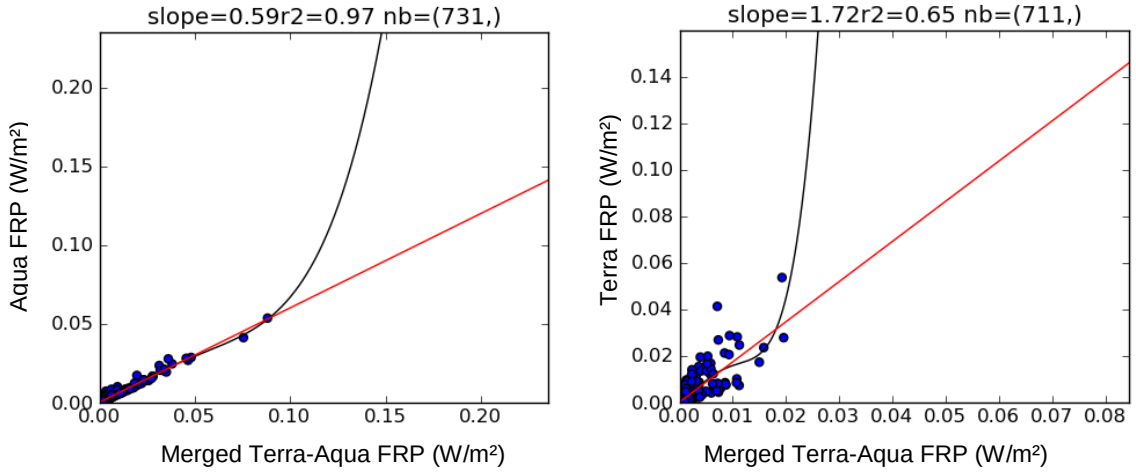

Figure 23: Same as Figure 22, but for an area comprised between 278 and 280 degrees of longitude and 4 and 6 degree of latitude.

It can be seen clearly from Figure 23 that if large values of Terra or Aqua FRP are scaled to a value closer to the merged observations using a nonlinear fit then the error could be very large. In view of this, a method combining both linear and nonlinear approaches was used: the nonlinear fit was preferred when values were “not too large” and the linear fit was preferred otherwise. What “not too large” meant in terms of FRP was derived by minimising a cost function over the learning dataset.

The regression formula was then applied to the daily gridded satellite data that is used prior to the assimilation process in GFAS. The results of this scaling of gridded data were assessed for the period ranging from 1/1/2012 to 30/4/2013 as shown in Table 1:

Merged obs.	Aqua	Scaled Aqua	Terra	Scaled Terra
220	295	221	144	205

Table 1: mean daily global FRP (µW/m²) for each entry, from 1/1/2012 to 30/4/2013.

This shows that the chosen approach was efficient in ensuring that the globally emitted FRP won't be biased when using the scaled FRP from either Terra or Aqua. It also shows, and this is confirmed by the individual tile correlation factors, that the fit works better for Aqua than for Terra. This can be explained by the simple fact that Aqua FRP being generally superior to Terra FRP because of their respective overpass times, the former contributes more (and is as a consequence more correlated to) to the merged data as compared to the latter. The Root Mean Square Error (RMSE) between the scaled and merged FRPs is rather important, in the order of 68 µW/m² for Terra and 43 µW/m² for Aqua. This shows the limit of this approach, which works rather well when considering a global budget, but shows rather large errors when considering individual fires. As our objective is to ensure that the fire emissions are globally consistent when using scaled FRP as compared to when using merged FRP, this approach gave satisfactory results. The GFAS dataset is now in the process of being extended to the years 2000, 2001 and 2002.

Also, this regression work has been carried out independently of the swath correction algorithm described in paragraph 2.1. This algorithm may alter the way Terra and Aqua gridded data relate to each other, as the swath dependency of Terra and Aqua data are not the same. Once the algorithm to alleviate the dependency of MODIS data to viewing angle, the fit between one satellite data and the mean of the two satellites data will have to be reviewed again.

2.4 Other aspects

2.4.1 Spurious signal map

Masking of non-biomass burning signals from gas flaring and volcanic activity

Oom and Pereira (2013) identified gas flares and volcanic signals from the MODIS Collection 5 active fire dataset using an extensive screening procedure. The authors kindly provided the longitude latitude coordinates of these non-biomass burning (NBB) signals on a daily basis for the period July 2001 to July 2012.

We used the 2003 to 2011 NBB time series, gridded to 0.1deg and 0.5deg, in

- *NBB1)* the native daily temporal resolution and temporally aggregated over
- *NBB2)* each month
- *NBB3)* each year.

We then intersected these masks with the daily mean GFASv1.1 FRP dataset (fl6z) and tested the effect of masking out the intersected grid cells on annual global total FRE, FRP maxima and on spatial patterns.

Figure 24a shows that NBB signals are prominent in the oil-producing regions of Western Siberia, in the coastal areas of the Gulf of Guinea and the Arabian Peninsula as well as in Northern Africa. In these regions, there are clusters of frequent NBB signals related to gas flaring, most of which are quasi-stationary (recurring in the same grid cell over several years) (e.g. Figure 24b).

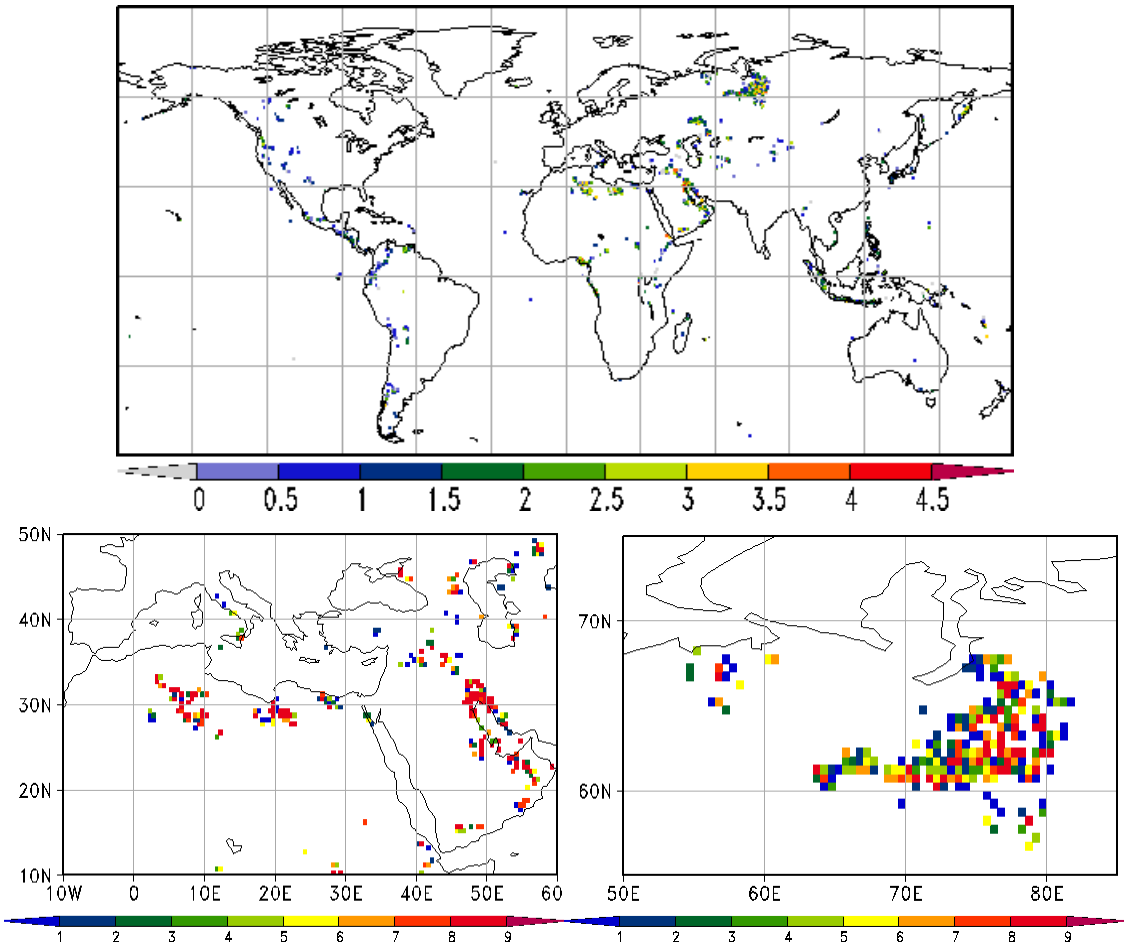

Figure 24 (a) Total counts of non-biomass burning signals per 0.5deg [log10] over 2003 to 2011 (in total 3287 days) (top) and (b) number of years with any NBB signal during this 9 year period i) in North Africa and the Arab Peninsula and ii) in West Siberia (bottom).

The effect of masking out NBB signals on global FRE budgets is largely independent of the temporal aggregation of the NBB mask (scenario NBB 1 to NBB3), removing on average 0.7% of the annual global total FRE.

In the enhanced GFAS system, we will mask out NBB signals using annually aggregated NBB masks (NBB3). Because the Oom and Pereira (2013) inventory only reaches until June 2012, we will mask out NBB signals in the near-real time GFAS system using NBB data aggregated over the period July 2011 to June 2012.

GFAS: Yearly global fire radiative energy [EJ a-1]					
Year	fl6z	fl6z.NBB1	fl6z.NBB2	fl6z.NBB3	% nbb3/fl6z
2008	5.15	5.12	5.12	5.12	-0.7%
2009	4.45	4.42	4.42	4.41	-0.8%
2010	4.88	4.85	4.85	4.85	-0.6%
2011	5.07	5.03	5.03	5.03	-0.9%
2012	5.28	5.27	5.26	5.24	-0.7%
Mean 2008-2011	4.89	4.86	4.85	4.85	-0.7%

Table 2: Effect of masking out non-biomass burning (NBB) events on yearly annual global total FRE in fl6z. Since the Oom and Pereira (2012) NBB dataset only goes until July 2012, NBB1 and NBB2 in 2012 only removes NBB until July, explaining the larger difference of this masking to NBB3 when compared to other years.

We checked the performance of the NBB3 mask by visually inspecting aerial photography of the grid cells with the highest daily mean FRP values in the 0.1 degree gridded product (fl6z) over the period 2008 to 2012. The analysis shows that the new NBB mask satisfactorily removes grid cells with very high daily mean FRP values caused by spurious signals (see Appendix).

Yet, the Oom and Pereira (2013) dataset does not cover spurious signals from industrial sites such as steel smelters, which typically do not produce very high daily mean FRP values, but which occasionally show up as biomass burning in GFAS (e.g. in Western or Central Europe, see also Andela et al., (2013)). In a follow up study, we will visually inspect aerial photography (e.g. Google Earth or Bing maps) of individual grid cells having an “urban” FRP signals to exactly identify the source of the signal. Urban grid cells are defined as FRP signal occurring in 0.1 degree grid cells classified as predominantly “urban and built up” in the MCD12Q1.051 data. Because this approach is very time-consuming, the focus will be on Europe first, to account for the spurious smoke plumes from industrial complexes observed in Central Europe by one reactive gas modeller in MACC-II (Andela et al., 2013). We will further explore if FRP signals, which were clearly identified as industrial, have unique characteristics in terms of temporal patterns and/or magnitude/range. Such characteristics could then potentially be used to globally automatically mask out these NBB signals in a follow-up GFAS version.

Despite several still exploitable options to increase the level of automatic masking of NBB signals, manual screening for and masking of NBB signals has to be an on-going quality control activity within GFAS. On the one hand, we need to regularly control that the automatic masking scheme performs with sufficient stability over time, removing most of the NBB, but no “true” biomass burning signals.

The Oom and Pereira (2013) dataset only covers the period 2001 to June 2012, and thus does not cover newly erupting volcanoes and recently or newly constructed gas flaring sites. We therefore plan annual updates of the NBB mask in the future.

For this purpose, a database will be established which contains the geographical coordinates of all identified spurious signals complemented by ancillary information about the source type, the source strength and the specific temporal patterns. The source type will be categories into volcanoes, industrial

gas flares, metallurgical industry, other anthropogenic heat sources, natural gas-based flames, coal mine fires and unidentifiable FRP signals. The update of this database is an on-going task; on a longer term, this database could also be used to improve the statistical characterisation of individual source categories - and thus automised masking options. It could also provide valuable information to other MACC partners to improve emission estimates of anthropogenic and volcanic source sectors.

2.4.2 Satellite data quality control

a) Effect of corrupt MODIS granules in GFASv1.1 on FRE budgets

During the detailed quality check for spurious signals which we performed on the GFASv1.1 product at 0.1 degree horizontal resolution (experiment ID fl6z starting from 2008 to now and fx5h starting from 2005 to 2011), it was confirmed that the quality control, which is active in the 0.5 degree product (GFASv1.0, experiment ID ffxr), had been disabled in the products with 0.1 deg resolution. This does not affect the real time service because no corrupt MODIS granules have been found in the real time data since 2009.

Since the existing quality control is applied to daily representations of the MODIS observations instead of individual granules, it unnecessarily discards many observations taken on the same day as a corrupt granule. Therefore it should be updated to be more specific and also to include tests designed for geostationary products.

In the year 2008, the fl6z product still contains two corrupt granules, which are masked out in the ffxr product. These two dates are listed as suspicious data in the description of GFASv1.0 in Tab. 1 of Kaiser et al. (2012).

a) Corrupt granule on December 8, 2008 (see Figure 25a and Figure 26, and *Fig. 4 in Andela et al., 2013)*

The maximum FRP value in the core domain of the corrupt MODIS granule (defined as 45°-70°E, 44°-52°N, red rectangle) is 6.54 W m^{-2}. The area integral over this core domain is 65.3PJ on Dec 8, 2008. The corrupt granule contributes 85% of the global total FRE of 77.1 PJ calculated for this day. There is widespread scattered fire activity in the greater vicinity of the corrupt granule.

Due the cloud-cover correction scheme applied in GFAS, the signal of the corrupt granule persists until the Dec 22, 2008. Over the period Dec 8 to Dec 22, the FRP values of the corrupt granule sum up to 82PJ, and thus contributes 16.3% to the global total FRE of the entire month.

Figure 26 illustrates that GFASv1.0 (ffxr) successfully masks out this corrupt granule.

b) Corrupt granule on February 16, 2008 (see Figure 25b)

The maximum daily mean FRP value of this corrupt granule on Feb 16 is 45.84 W m^{-2}. This is also highest FRP value globally on this day in fl6z. With an area integral of 17.3 PJ, it contributes 64% of the daily global total FRE. There is no obvious biomass burning activity in the greater vicinity of the corrupt granule. In the fl6z product, the signal of the corrupt granule persists until

Feb 23. Over the period Feb 16 to Feb 23, the FRP values of the corrupt granule sum up to 132 PJ, which is 34.4% of the global total FRE of the entire month.

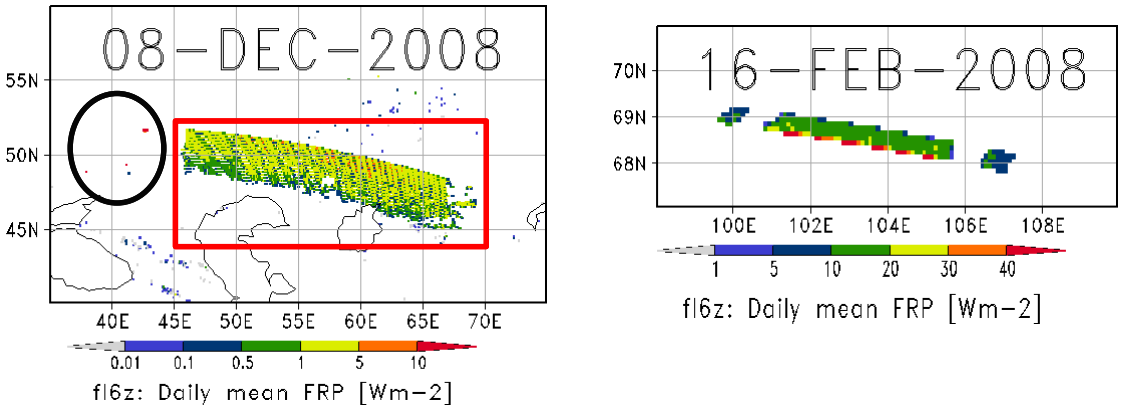

Figure 25: a) (left) Daily mean FRP on December 8, 2008 in the domain 40°-75°E and 40°-60°N with an obvious corrupt MODIS granule. b) (right). Daily mean FRP on February 16, 2008 in the domain 98°-110°E and 67°-71°N with an obvious corrupt MODIS granule. Please note the different scales.

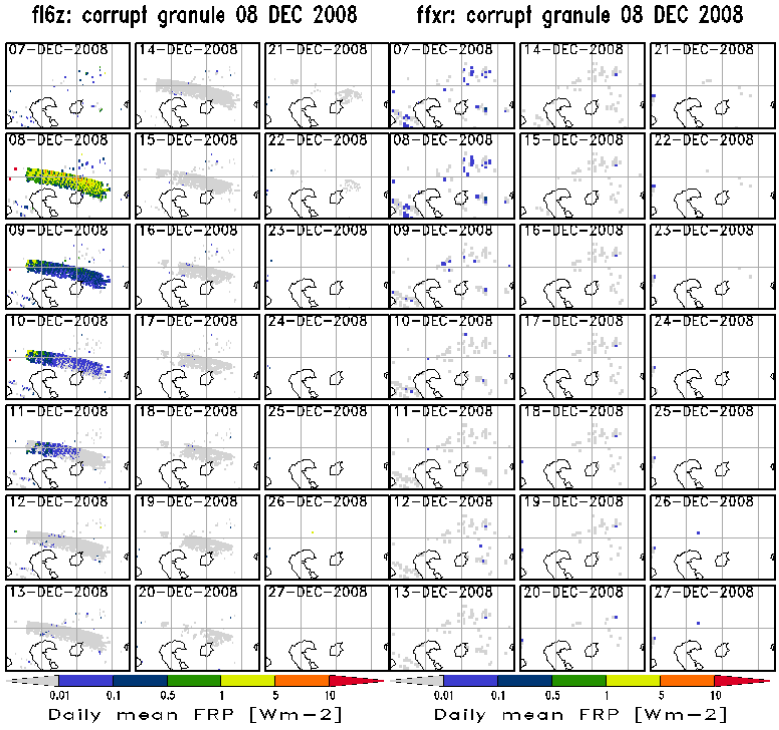

Figure 26: Daily mean FRP in the domain 40°-75°E and 40°-60°N from December 7 to December 27, 2008. The shape of the corrupt MODIS granule is apparent from December 8 onwards in fl6z (left), but not in ffxr (right). Due to the persistency assumptions implemented in GFAS, the signal of the corrupt granule decreases only over the subsequent days.

The FRP signals of the two corrupt MODIS granules on Feb 16, 2008 and Dec 8, 2008 sum up to 215 PJ and thus contribute 4.2% to the global annual total FRE in 2008 in the fl6z product. The failed masking of these granules in GFASv1.1 largely explains the differences in the global annual FRE budget between ffxr and fl6z, and thus also controls the differences in emission budgets (Table 3). For example, in the year 2008, global annual total FRE in fl6z 5.8% higher than in ffxr, but only 1.4% higher when fl6z is corrected for the two corrupt MODIS granules.

GFAS: Yearly global fire radiative energy							
Year	ffxr	fl6z	fl6z*	Δ fl6z-ffxr		Δ fl6z*-ffxr	
	[PJ]	[PJ]	[PJ]	[PJ]	(% of ffxr)	[PJ]	(% of ffxr)
2008	4,871	5,154	4,940	283.3	(5.8%)	68.7	(1.4%)
2009	4,238	4,448	-	210.3	(5%)	-	-
2010	4,652	4,877	-	224.9	(4.8%)	-	-
2011	4,885	5,069	-	183.8	(3.8%)	-	-
2012	5,046	5,279	-	232.9	(4.6%)	-	-

Table 3: Annual global total FRE in the different GFAS versions. fl6z denoted the fl6z product corrected for two corrupt MODIS granules (FRP from corrupt granule 20080216 and 20081208).*

Clearly, corrupt MODIS granules, although very limited in space and time, have strong impact on regional and even global emission budgets and it is very important to develop algorithms that automatically detect and mask out these spurious signals. This aspect is addressed in the next section.

b) Enhanced algorithms to control for corrupt MODIS granules

The potential problems affecting the data are specific for each satellite; as a consequence a satellite-specific approach has been preferred for the implementation of quality control, instead of a common algorithm.

It was shown by a careful analysis of the GFAS dataset from 1/1/2005 to 31/12/2010 that MODIS (Terra and Aqua) data contained only two corrupt granules, on 16th of February 2008 and 8th of December of the same year. These two corrupt granules were used to devise a quality control algorithm which would allow not to take them into account, and which criterion would not be reached by other MODIS granules.

Figure 27 shows the impact of the corrupt granule of 8th of December 2008 on a gridded FRP product that is merging Aqua and Terra.

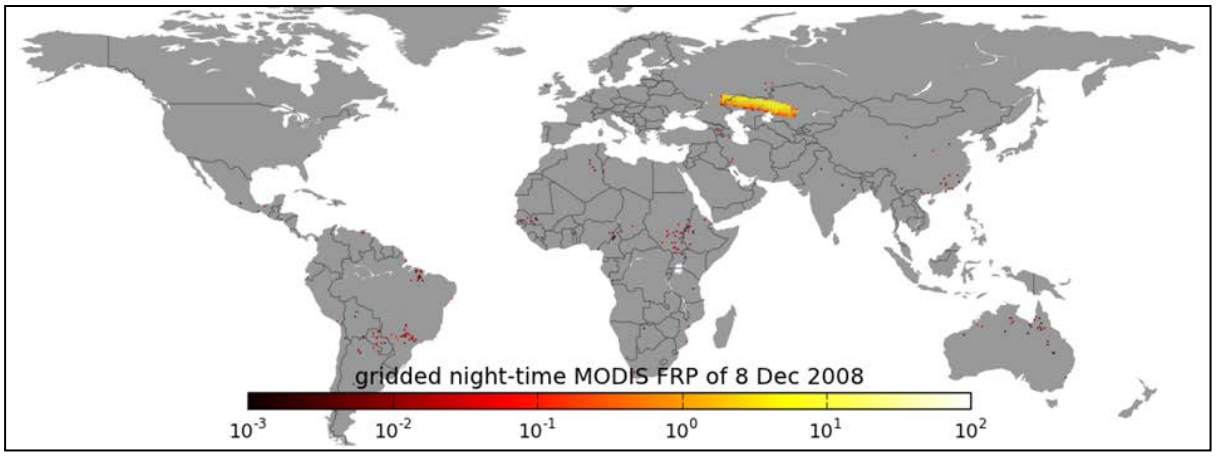

Figure 27: Gridded night-time (21 to 9 local time) Fire Radiative Power on the night of 8th to 9th of December 2008, W/m².

For each MODIS granule, a test was implemented that deemed data faulty if more than 3 per cent of the observed pixels correspond to active fires, i.e. with nonnull FRP, and if the granule contains more than 1000 pixels with positive FRP. This test rejected the 8th of December corrupt granule. It was tested for the period ranging from 1/1/2005 to 31/12/2009 and was not activated on any other occasion.

The second corrupt MODIS granule occurred on 16th of February, as shown by Figure 25b. It was caused by a failure in the colocation of a great number of pixels, using the MOD03 product. As a consequence, a quality control test has been added that rejects a granule if more than one thousand of its pixels cannot be satisfactorily geolocated with a precision of more than ten kilometres. This test rejects the corrupt granule of 16th of February 2008 but was not activated in other cases during the 1/1/2005 to 31/12/2009 period.

c) Enhanced algorithms to control for corrupt SEVIRI products

The SEVIRI FRP data provided by Land SAF can occasionally be affected by quality problems.

Figure 28 shows an example for the morning of 4th of August 2008. The corrupt granule of 5:45 UTC displays many more fires than the one at 5:30 and the total Fire Radiative Power for the shown area is more than 50 times larger at 5:45 than at 5:30.

To prevent such faulty data, a filter was implemented that compares raw SEVIRI FRP to the previous available data. If a large variation between the two is noted then the latter SEVIRI (i.e. a more than 20-fold increase) on a great number of pixels (i.e. more than a thousand), then FRP data is discarded. The efficiency of this filter has been checked, in order to verify that the 4th of August 2008 situation is removed. SEVIRI quality control has been run for the year 2010 without the criterions being met a single time.

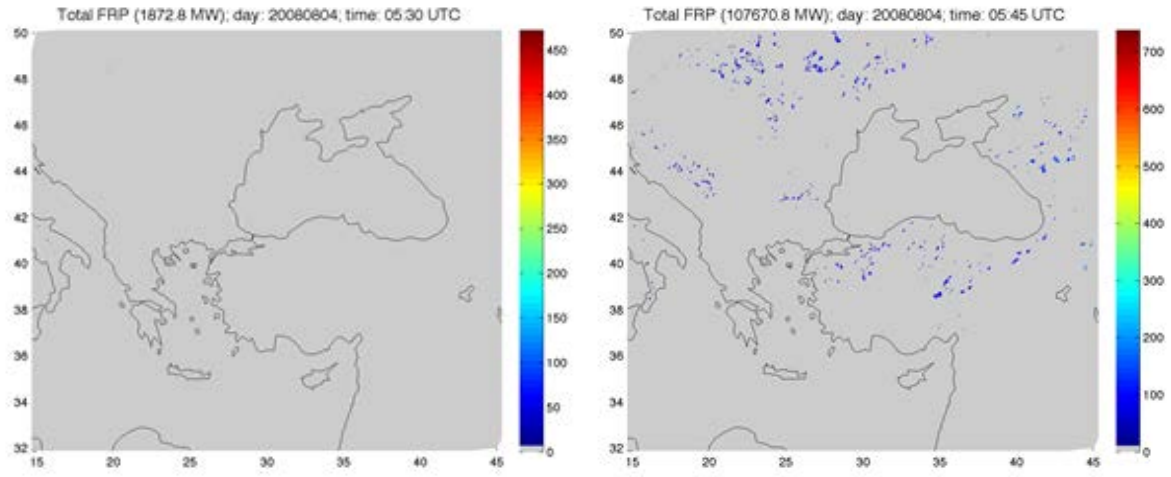

Figure 28: SEVIRI FRP in MW over Europe at 5:30 UTC on the left and at 5:45 UTC on the right. The right panel contains widespread fire activity that is isolated in this individual measurement frame and thus suspicious. (courtesy of Giuseppe Baldassarre, Istanbul Technical University)

3 Emission Calculation

3.1 GFAS fire type map

3.1.1 Emission factors and fire types

GFASv1.0 and GFASv1.1 (here summarised as GFASv1) have eight different fire type ("fuel") classes. Of these eight classes, four are surface land cover categories, namely savannah (SA), agriculture (AG), tropical forest (TF) and extratropical forest (EF). The spatial resolution of the GFASv1 fire type map is 0.5 degree.

For a next release of GFAS, a refinement of the fire type map is envisaged, not only in terms of a higher spatial resolution (0.1 degree) but also in terms of fuel categories. The benefits from such a refinement could be i) the application of more appropriate (i.e. more fuel-type specific) emission factors, ii) the development of more realistic conversion factor that better reflect the "true" combustion and emission characteristics, and iii) a more realistic representation of the seasonality of fire emissions.

To date, two peer-reviewed comprehensive emission factor compilations exist, namely the compilation by Andreae and Merlet (2001) [A&M01] and the more recently established compilation by Akagi et al. (2011) [AK11]. The GFED3 and GFASv1 inventories used the A&M01 compilation. The A&M01 compilation covers the fuel categories savannah, tropical forest, extratropical forest, agricultural residues. It aggregates emission factors measured by field measurements of fresh and aged smoke plumes. So far, it is the most widely used in biomass burning emission inventories.

In contrast to A&M01, the more recently established AK11 compilation only includes emission factors measured in fresh, photochemically unaltered smoke plumes. Furthermore, it has additional fuel types as it subdivides extratropical forest into temperate forest and also provides emission factors for a) chaparral

burning and b) pasture maintenance burning. Finally, it is regularly updated (latest version v3, released in January 2013)[1], thus incorporating the most recent measurement results published. Due to these advantages, it seems reasonable to recommend the AK11 compilation for GFASv2. Table 4 shows the fire-type categories used in AK11.

"natural fire-types"			
#	Category	Abbrev.	Definition by AK11
1	**Tropical forest**	TROFOR	This category includes tropical evergreen forest deforestation fires, tropical dry forest deforestation fires, and tropical dry forest understory fires. Tropical dry forest is also called "seasonal" or "monsoon" forest. Tropical dry forests (TDF) differ from "woody" savannah regions in that TDF are characterized by a significant (>60%) canopy coverage or closed canopies.
2	**Boreal forest**	BORFOR	This category includes all extratropical forests north of 50°N.
3	**Temperate forest**	TEMFOR	This category includes all extratropical forests south of 50°N.
4	**Savanna**	SAVA	This category includes the savanna, woody savanna, and grassland categories contained in the detailed MODIS land cover products (Friedl et al., 2002). More generally, savannah regions are qualitatively described as grassland with an "open" canopy of trees (if any).
5	**Chaparral**	SHRUB	This category is representative for a type of temperate shrubland fire which is important in the southwestern US, and, more generally, for shrubland fires globally.
6	**Peatlands**	PEAT	This category is representative for fires in peatlands (with assumed tropical forest overstory).
"anthropogenic fire-types"			
1	**Crop residue**	CROP	This category includes all burning of crop residues (excluding the combustion of crop residues as biofuels). Crop residue may be burned 1–3 times a year on a single site depending on the rate of annual harvest and yield short-lived, relatively small fires.[2]
2	**Pasture maintenance**	PAST	This category includes burning of pastureland which is performed every 2–3 year to prevent reconversion of pasture to forest. These fires frequently include residual smoldering combustion of large logs that can burn for weeks after the flames have ceased.

Table 4: Fire-type categories used in AK11. Text largely adapted from AK11.

[1] Downloadable from http://bai.acd.ucar.edu/Data/fire/.

[2] On a longer term, it would make sense to separate areas by crop type because AK11 noted that the EFs for different agricultural burning types are very different and that it would be preferable to apply the specific EFs for each type of agriculture. Spatial maps on for various crop types are available e.g. at http://kids.fao.org/agromaps/.

Table 5 shows that some emission factors differ strongly between the various fire types. For example, the CO emission factor for TEMFOR is 31% lower than for BORFOR while the NOx emission factor is 110% higher. Similarly, the emission factors for SHRUB are very different from those of SAVA, especially for species such as OC and BC. Due to the large fraction of residual smouldering combustion occurring in PAST burning, the CO emission factor of PAST is more than two times higher than SAVA or SHRUB burning. The differences illustrate the importance of treating fire type categories separately when applying emission factors.

EF in g kg^{-1}	**AK11 (Akagi et al. 2011, ACP; Version 3 (January 30, 2013))**							
Species	TROFOR	BORFOR	TEMFOR	SAVA	CROP	PAST	SHRUB	PEAT
Carbon Dioxide (CO2)	1643	1489	1647	1686	1585	1548	1681	1601
Carbon Monoxide (CO)	93	127	88	63	102	135	67	106
Methane (CH4)	5.1	6.0	3.4	1.9	5.8	8.7	3.0	6.4
NOx (as NO)	2.6	0.9	1.9	3.9	3.1	0.8	3.6	n.a.
PM2.5	9.9	15.3	12.6	7.2	6.3	14.8	7.1	n.a.
Total Particulate Carbon	5.2	n.a.	n.a.	3.0	3.1	10.6	5.0	7.4
Organic Carbon (OC)	4.7	n.a.	n.a.	2.6	2.3	9.6	3.7	6.8
Black Carbon (BC)	0.5	n.a.	n.a.	0.4	0.8	0.9	1.3	0.6
Methanol (CH3OH)	2.4	2.8	1.7	1.2	3.3	5.8	1.4	3.0
Propane (C3H8)	0.1	0.4	0.2	0.1	0.3	0.2	0.5	n.a.

Table 5: Emission factors for selected species according to AK11, version v3.

3.1.2 Translation of land cover classes into fire types (Translation 1, Default)

In the following, we assign the UMD land cover classes (Land Cover Type 2 (LCT2)) to the AK11 fire type classes. For this purpose, we use the annual MCD12 (version v5.1)[3] land cover dataset of the year 2005 to map the spatial extend of each land cover class (Figure 29). We use the UMD legend because it corresponds most closely to the AK fire type classes. The IGBP legend (LCT1), for example, which is available in the MCD12 data, has the class “permanent wetlands” which cannot be translated into an AK11 fuel class. Furthermore, this choice ensures consistency with GFED3, which also uses MCD12 along with the UMD classification.

[3] Originally, this analysis was done with MCD12C1 version v5.0. Due to critical errors in the discrimination between evergreen needleleaf forest and shrublands contained in the version v5.0, the MCD12C1 product was updated to version v5.1 in April 2011 (see also http://landval.gsfc.nasa.gov/pdf/MCD12Q1_c5.1_doc.pdf). The area coverage of LC1 and LC3 decreased by 50% in version V5.1 while LC5, 9 and 10 increased by 15 to 33%. GFED3 and hence GFASv1 uses MCD12 v5.0; it is therefore likely that the areal extend of needleleaf forests, which are most prominent in the boreal regions, are strongly overestimated.

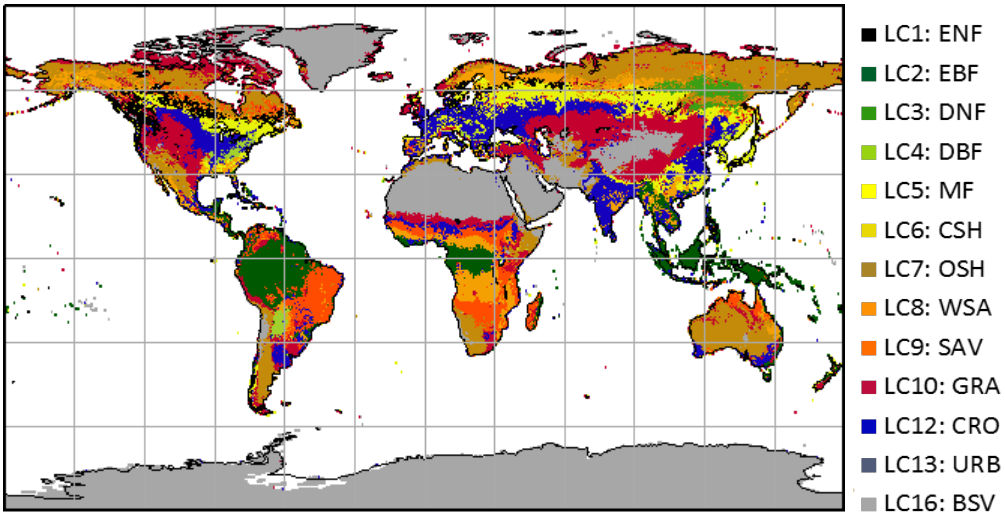

Figure 29: Map of MCD12 (v5.1) land cover of the year 2005 (UMD classification) remapped to 0.1 degree using largest area fraction approach (see also Table 6)

LCCAT	LC	Description	MCD12C1: 2005				
			All	%	TRO	TEMP	BOR
ENF	1	Evergreen needleleaf forest	2.8	2%	0.1	0.7	2.1
EBF	2	Evergreen broadleaf forest	13.5	9%	13.1	0.4	0.0
DNF	3	Deciduous needleleaf forest	1.5	1%	0.0	0.0	1.5
DBF	4	Deciduous broadleaf forest	1.9	1%	0.8	1.0	0.1
MF	5	Mixed forest	8.2	6%	1.2	3.2	3.9
CSH	6	Closed shrublands	0.3	0%	0.2	0.1	0.1
OSH	7	Open shrublands	20.7	14%	7.5	4.9	8.4
WSA	8	Woody savannas	12.7	9%	7.9	1.4	3.4
SAV	9	Savannas	11.4	8%	9.7	0.3	1.4
GRA	10	Grasslands	20.2	14%	5.3	10.5	4.5
CRO	12	Croplands	16.5	11%	6.4	7.5	2.7
URB	13	Urban and built-up	0.6	0%	0.2	0.4	0.1
BSV	16	Barren or sparsely vegetated	34.2	24%	13.0	5.9	15.3
Sum		**mio. km^2**	**144.8**	**100%**	**65.3**	**36.2**	**43.3**

Table 6: Area [in mio.km2] and area contribution of the UMD land cover classes in the MCD12 dataset of the year 2005. The columns TRO, TEMP and BOR provide area statistics for the tropical, temperate and boreal zone.

In the UMD legend, all forested classes (LC1 to LC5) are defined as lands dominated by trees with a canopy cover exceeding 60% and heights exceeding 5 meters. The shrubland classes (LC6 and LC7) are defined as lands dominated by bushes or shrubs with (LC6) shrub canopy cover >40% and shrub heights <5 m and (LC7) shrub canopy cover between 10-40% and shrub heights <2 m. The shrub foliage can be either evergreen or deciduous. The tree canopy cover is less than 10%. All savannah classes (LC8 and LC9) are defined as lands with herbaceous or woody understories and tree canopy cover of 40-60% (LC8) and of 10-40% (LC9), respectively, with tree cover heights exceeding 5 meters. Grasslands are defined as lands with continuous herbaceous cover and <10% tree or shrub canopy cover.

As specified in AK11, we used latitudinal zones to translate forested UMD land cover classes into the AK11 fire type classes tropical forest (TROFOR) (LAT ≤|30°|), temperate forest (TEMFOR) (30°N-50°N and 30°S-50°N) and boreal forest (BORFOR) (LAT >|50°|) (Table 8). We made exceptions from this rule to avoid misclassifications:

1. The forest cover classes LC1 to LC4 typically occur in given zones: The needleleaf classes (LC1 and LC3) predominantly occur in the boreal zone, while evergreen broadleaf forests (EBF (LC2)) are prominent in the tropics and deciduous broadleaf forests (LC4) are most common in the temperate zone. More than 95% of the area of the forested land cover classes (LC1 to 4) occurs within two neighbouring zones. For example, evergreen needleleaf forest (ENF (LC1)) is treated as BORFOR at latitudes >|50°| and within 50°S and 50°N as TEMFOR. There are marginal areas of ENF that occur in the tropics (2.5% of global ENF area). These are subsumed into the TEMFOR category. In the tropics, ENF primarily occurs around Tibet (i.e. north of 17°N), and these high-altitude evergreen needleleaf forests are more similar to TEMFOR or BORFOR in terms of fuel and burning characteristics than to TROFOR. In order to assign each forest class to the most representative zonal fuel class, we only allowed each forest cover class to span over two neighbouring zones. Mixed forests (MIF (LC5)), whose geographic distribution is more scattered around the globe, are translated into all three zones.
2. We treated WSA (LC8) in the boreal zone as BORFOR. AK11 did not specify a lower bound TC for the BORFOR or TEMFOR fuel class, leaving it largely up to the users what legend (i.e. what TC cut-off) to apply (B. Yokelson, personal communication, Aug. 1, 2013). Boreal forests generally have a lower tree cover (TC) density than temperate or tropical forests (b). The AK11 BORFOR emission factors are calculated as a weighted mean of the emission factors measured in smoke plumes of individual boreal fires.
3. Table 7 provides the geographical coordinates of these fires and a) the predominant MCD12 LC of the corresponding 0.05deg grid cell and b) the mean MOD44B TC in the corresponding 0.1 deg grid cell. The TC of the fires included into the AK11 BORFOR category is distinctively lower than the definitional threshold for forests in the UMD legend (i.e. 60% TC). Mean TC is between 12 - 16% (fires measured by Goode et al. (2000)) and 38% (fires measured by Simpson et al. (2011)). Only the latter are classified as forest (LC1 ENF) while all fires in Goode et al. (2000) are classified as OSH (LC7). In contrast, the TC of the fires included into the TEMFOR and TROFOR fuel categories is distinctively higher[4], and the MCD12 dataset maps the corresponding grid cells as forest (LC 1 – 5). It appears that the TC threshold for forests in the UMD legend does not lead to a representative mapping of the AK BORFOR fuel category in the boreal zone, and that it is more appropriate to include also more sparsely tree covered areas into this category. For this reason, we included all lands classified as woody savannah (LC8 WSA, defined as having a tree canopy cover between 40 and 60%) at latitudes >|50°| into the BORFOR fuel category.
4. We replace the AK11 fuel category CHAP by the more general term shrublands (SHRUB). This fuel category comprises all shrublands (LC 6 and LC7) globally. We also include areas covered by WSA (LC8) in regions with Mediterranean-type climates into this category to improve the representation of areas covered by chaparral vegetation.

[4] see also Fig. 5 in van Leeuwen and van der Werf (2011).

Reference	ID	Fire	Characteristics	LON	LAT	LC 0.05d	TC 0.1d
Goode et al. (2000)	**1**	Wildfire B349	mosaic of black spruce, shrub, and bog	-157.1	63.6	OSH	12%
	2	Wildfire B349	black spruce forest with crown fires	-151.2	67.1	OSH	16%
	3	Wildfire B309	open black spruce forest/shrub/bog mosaic	-158.4	63.6	OSH	15%
Nance et al. (1993)	**4**	Wildfire A121	old black spruce forest: low-intensity ground fire that burned through the top layer of needles on the ground with occasional torching of tree crowns	-147.8	66.6	OSH	16%
Simpsons et al. (2011)*	**5**	Fire captured by plume 2&3	Saskatchewan fire plumes	-107	56.5	ENF	38%
*Simpson et al. (2011) does not specify which biomass burning plumes they included into their emission factor calculation and what exact location of the actual fire they correspond to. The flight track information is available at http://www.espo.nasa.gov/arctas/docs/flight/2008-6-30_p3_report.pdf							
Radke et al. (1991) is omitted here because it is unclear which four prescribed boreal fires from Radke et al. (1991) were included into Akagi et al. (2011). Also no precise LON-LAT information of the fires are given in Radke et al. (1999), only a vague region information such as "Montesano, Washington".							

Table 7: Longitude and latitude information of the fires included into the AK11 BORFOR category and corresponding predominant land cover (LC 0.05d) and mean tree cover density (TC 0.1d). The numbers are calculated from the MC12C1 UMD and the MOD44B data of the year 2005, remapped to 0.05 and 0.1 deg, respectively.

Class (LC)	UMD land cover (Type 2)	Corresponding "Akagi" fuel-type
1 ENF	Evergreen needleleaf forest	BORFOR (LAT >|50°|); else: TEMFOR
2 EBF	Evergreen broadleaf forest	TROFOR(LAT ≤|30°|); else: TEMFOR
3 DNF	Deciduous needleleaf forest	BORFOR (LAT >|50°|); else: TEMFOR
4 DBF	Deciduous broadleaf forest	TROFOR(LAT ≤|30°|); else: TEMFOR
5 MIF	Mixed forest	TROFOR(LAT ≤|30°|);TEMFOR (30 -50°N/S); else BORFOR
6 CSH	Closed shrublands	SHRUB
7 OSH	Open shrublands	SHRUB
8 WSA	Woody savannas	BORFOR (LAT >|50°|);else: SAVA. Exception: SHRUB for domains with Mediterranean-type climate Domain — Latitude and longitude bounds California: 32°N-43°N, 125°W-115°W Chile: 40°S-30°S, 75°W-68°W Mediterranean Basin: 30°N-42°N, 10°W-45°E Cape: 36°S-32°S, 16°E-28°E Australia: 40°S-28°S, 112°E-146°E
9 SAV	Savannas	SAVA
10 GRA	Grasslands	GRAS (EF for SAVA)
12 CRO	Croplands	CROP
13 URB	Urban and built-up	GRAS
16 BSV	Barren or sparsely vegetated	GRAS (EF for SAVA)

Table 8: MCD12C1 UMD land cover classes and corresponding AK11 fuel types (Translation scheme 1).

3.1.3 Variations in the translation schemes

In order to test the effects of varying translation schemes on conversion factors and global and regional budgets of emission fluxes, three more translation options are created in addition to the default translation scheme T1 defined in Table 8.

Translation scheme	Description
T1	default translation as defined in Table 8
T2	same as T1, except that WSA is not treated as BORFOR at LAT >|50°|, but as SAVA
T3	same as T1, except that all SHRUBS are treated as SAVA
T4	same as T3, except that WSA is not treated as BORFOR at LAT >|50°|, but as SAVA

Table 9: Translations schemes.

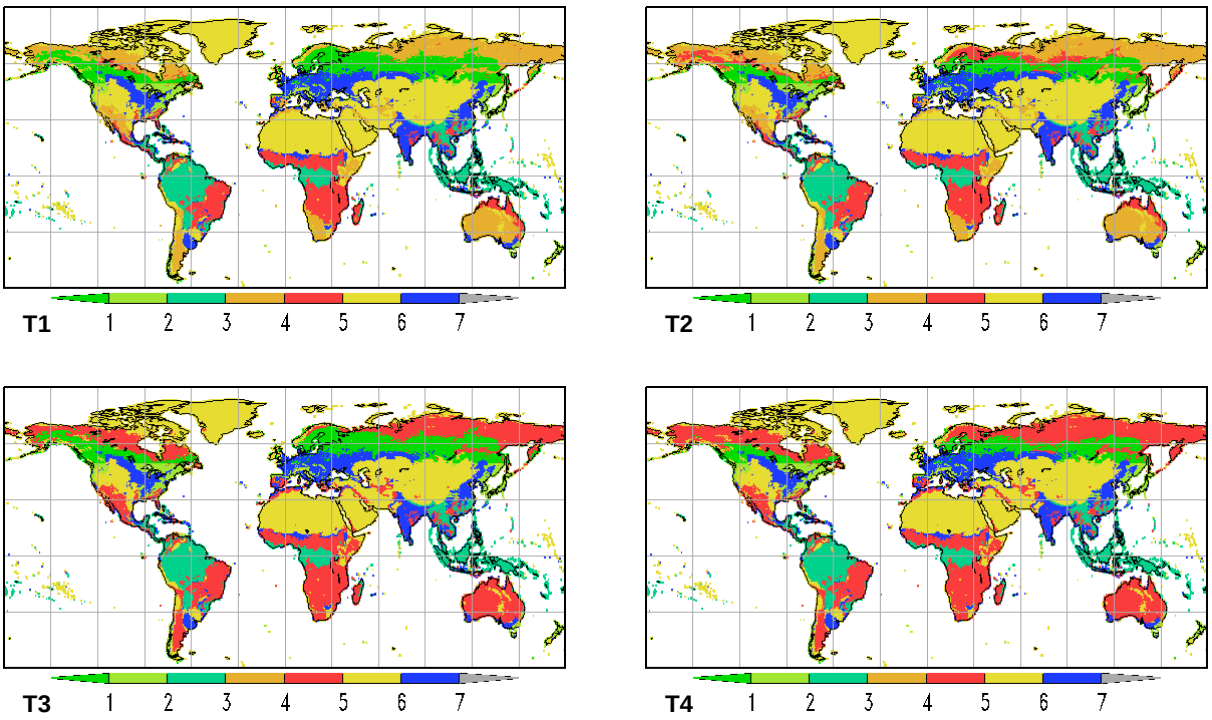

Figure 30: Spatial pattern of the AK11 fuel types when varying the translation scheme (T1 to T4). (1=BORFOR;2=TEMFOR;3=TROFOR;4=SHRUB;5=SAVA;6=GRAS;7=CROP)

The variations in the four translation schemes reflect the definitional range of the AK11 fuel categories. The fuel categories are most imprecisely defined in the boreal regions because of the unclear tree cover density threshold for the category boreal forests. The interpretive uncertainty is also high in areas classified as UMD class shrublands (OSH and CSH), as it is unclear if they are best treated as individual class or savannah. Figure 30 illustrates that the effect of varying translation schemes on the spatial patterns of the AK11 fuel categories; each translation is a realistic representation of the AK11 fuel types. Yet, the

definition of the fuel categories in AK11 is more precise than in the A&M01 compilation, which misses, e.g. the category temperate forest and shrublands.

The different translation schemes aim at demonstrating the magnitude of the uncertainty in the emission estimates linked to the interpretive uncertainty, which is only one of many sources of uncertainty.

3.1.4 Dominant or fractional fire type versus dominant or fractional land cover

GFASv1.0 uses a dominant fire type map at 0.5 degree horizontal resolution to calculate conversion factors and to apply fire-type specific emission factors. Surface vegetation and soil organic matter are treated as separate layers, except for peat, where no surface vegetation characteristics are taken into account.

The aim is to create new fire "or fuel" type maps for the enhanced GFAS system that will be produced at 0.1° horizontal resolution. To improve consistency, we define a surface vegetation – or surface fire type – at any grid cell globally. Potential burning of soil organic matter (including peat) below this surface vegetation cover will be parameterised separately and is a still subject of on-going research.

Here, we explore different options of creating an enhanced surface fire type map using annual MCD12Q1.051 data over the period 2001 to 2012 and the UMD-classification translated into the 7 new GFAS surface fuel types (see also Section 3.1.2).

Four options are considered:

(1) Dominant LC, a dominant land cover (LC) map (Figure 31).

(2) Dominant Fire, a dominant fire type map (Figure 32).

(3) % LC, a relative land cover map for each GFAS biome.

(4) % Fire, a relative fire type map for each GFAS biome.

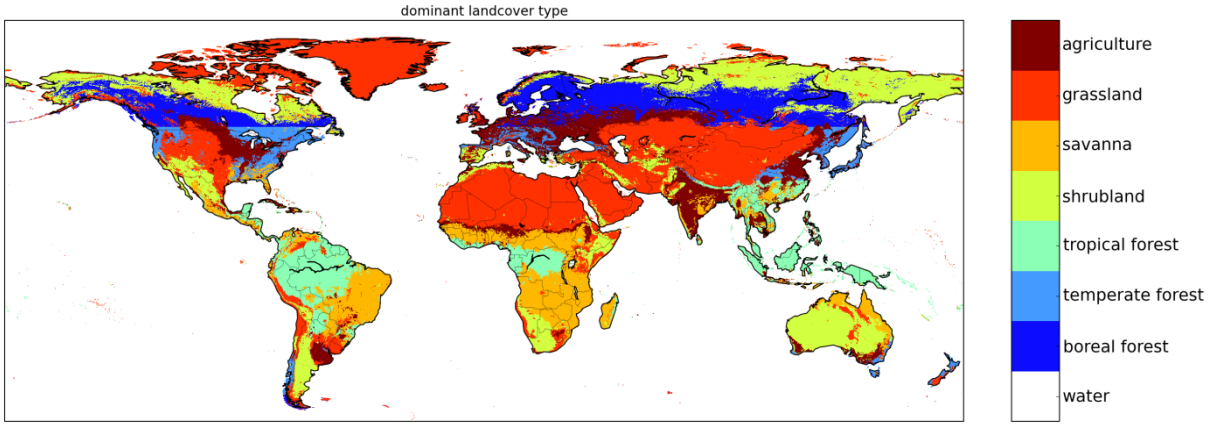

Figure 31: Dominant land cover at 0.1°, based on the mean of 0.05° MCD12C1.051 UMD-classification land cover (2001-2012) rescaled to the 7 GFAS classes.

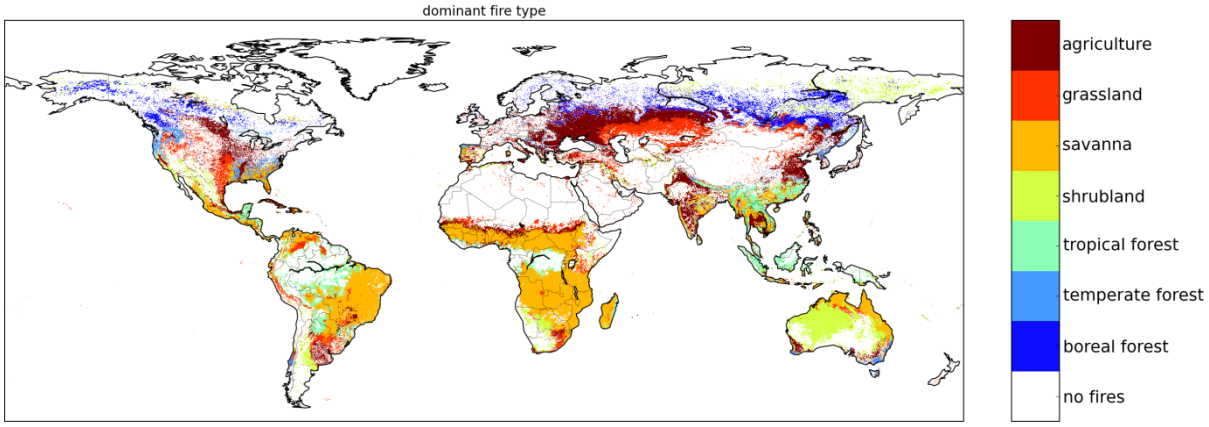

Figure 32: Dominant fire type, based on MOD14 1km resolution data (2001-2012) and the 7 GFAS land cover classes at 1km resolution (rescaled 500-m MCD12Q1.051 UMD-classification). Dominant fire type is equal to that land cover (at 1km-resolution) that showed the highest FRP within the 0.1° grid cell. This map is based on 2001-2012 fire data only; areas without fires in these years remain white.

Globally, the dominant land cover and the long-term mean dominant fire type exhibit largely similar spatial patterns (Figure 31 and Figure 32). At a higher level of temporal and spatial and detail, however, there are clear differences between both options. Figure 33 illustrates these differences for the year 2001 for areas categorised as having savannah as dominant fire type, i.e. in these 0.1 degree grid cells, most of the fire radiative energy in 2001 is released by fires in savannah. The figure shows that in a substantial number of these grid cells, the dominant land cover is tropical forest. This phenomenon is strongest in the tropical deforestation regions of South America and Africa.

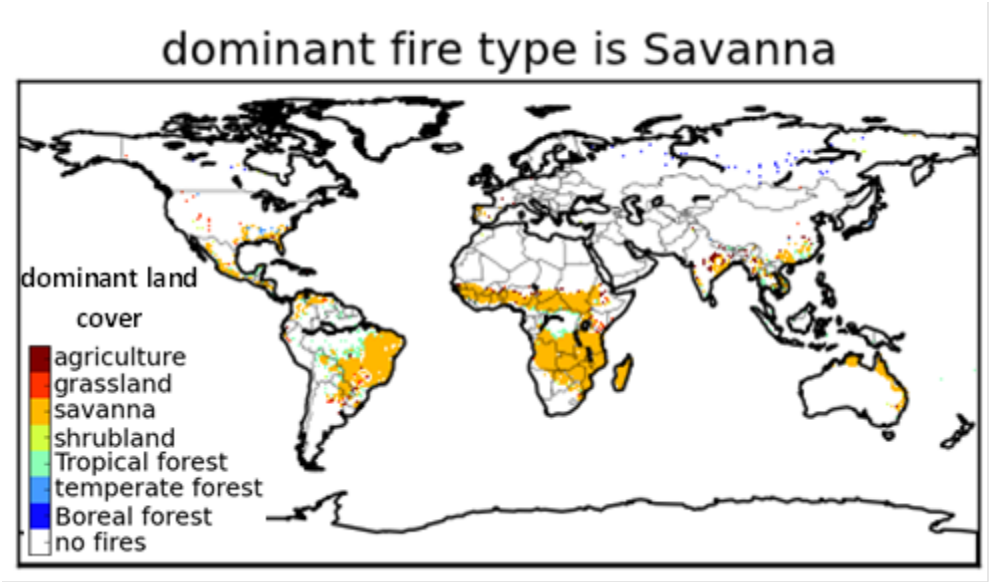

Figure 33: Dominant fire type compared to dominant land cover at 0.1° degree. The plot shows the dominant land cover in areas categorised as having the dominant fire type "savannah". This map is based on 2001 fire data, only.

Table 10 provides summary statistics of the mean annual (2001-2012) fire radiative energy attributed to each surface fuel type using the four fire type mapping options described above.

Land cover (LC) type	(1) Dominant LC	(2) Dominant Fire	(3) % LC	(4) % Fire
Boreal Forest	6.0	6.2	5.1	5.6
Temperate forest	1.8	1.9	1.7	1.8
Tropical forest	6.9	5.8	6.7	5.8
Shrubland	10.3	9.9	10.3	10.1
Savannah	37.3	38.5	35.8	36.5
Grassland	7.5	7.8	9.2	9.0
Cropland	6.6	6.4	7.7	7.7
Sum	**76.4***	**76.5****	**76.5*****	**76.5******

*Table 10: Mean of observed FRP (MOD14; 2001-2012; Terra Watt yr-1). Four different ways of calculating the sum are compared using 0.1° maps. (1) All FRP within a grid cell is attributed to the dominant land cover (*excluding water); (2) all FRP within a grid cell is attributed to dominant fire type (**which is defined such that it cannot be water); (3); For each grid cell FRP is distributed over the different land cover classes within that grid cell according to their % occurrence (excluding water); and (4) like 3, but now all FRP is attributed to actual fire type. *** In option 3, at 0.1° if grid cells were partly covered by water, all fires were attributed to the other land cover classes, depending on their occurrence. **** In option 4, if fire burned in a pixel classified as water, the FRP is distributed over the remaining fire type, depending on their occurrence.*

Typically, the differences in the relative contribution of individual fuel classes to the mean annual fire radiative energy (FRE) released is small (within around 1%) between the different options. As already illustrated in Figure 33, larger difference between dominant land cover (Option 1) and dominant fire type (Option 2) are observed for tropical forest and the savannah biome: The contribution of savannah fires increases from 48.8% (Option 1) to 50.3% (Option 2) while, at the same time, the contribution of the tropical forest fires decreases from 9.0% to 7.6%. This tendency towards more savannah fires also shows up in the comparison of the relative land cover map (Option 3) and the relative fire type (Option 4), and gives reason to the following interpretation: It is expected that for tropical regions with mixed land cover, savannah grasses are more likely to burn than tropical forest. This can be explained by the fuel that dries much quicker, but also by the fact that fire is often used as a tool to prevent trees from growing in grasslands and to maintain pasture. The tendency of depicting more savannah fires in areas with a mixture of forest and savannah could also point to a bias in the detection of the FRP signal: Possibly, the FRP signal is more strongly obscured in forested than in savannah areas due to a greater tree canopy cover density.

Calculating the summary statistics in Table 10 without correcting for areas classified as inland water (UMD land cover class WAT) in the UMD legend of the MCD12Q1.051 data may lead to a systematic omission of fires occurring in wetlands. For example, without this correction, 0.3 % of the 2001-2012 mean annual FRE released in Option 4 is omitted because the fire burned in a pixel classified as water. Dependent upon the year, these “fire-in-water” pixels can make up to 0.9% of the annual global FRE.

A more detailed analysis showed that many of these “fire-in-water” pixels actually occur in wetland areas (such as swamps, marshes, bogs and fens), and hence are “true” vegetation fires and not spurious signals. Fires in wetlands are not uncommon during dry seasons (Jones et al., 2013) and need to be taken into account in fire emission estimation.

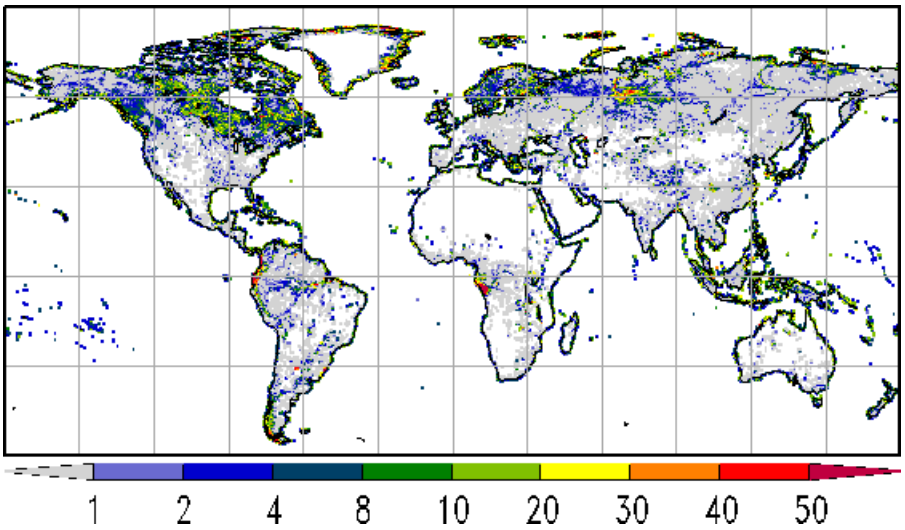

Figure 34: Percent area contribution of the UMD land cover class water over land. The MCD12Q1.051 data of the year 2005 are 0.5 degree horizontally gridded.

In contrast to the IGBP legend, the UMD legend does not comprise a separate wetland land cover class, and therefore tends to classify them as water. As a result, the area covered by inland water in the MCD12Q1.051 data of the same year is more than 10% larger in the UMD legend than in the IGBP legend. Figure 34 shows that in the boreal belt, most notably in Canada, the UMD land cover class water contributes 10 to 30% (and more) over large areas.

In order to avoid the omission of “fire-in-water” signals, we introduced a correction scheme for all four options (see also Table 10). In case of the dominant fire type and land cover maps, we simply did not allow water to be the dominant class (unless 100% water cover), but rather picked the second dominant class. For the relative land cover, mixed pixels of water and other land cover classes are corrected such that non-water land cover classes together make up 100% (so that no fires ‘occur in water’). For the relative fire types, the same approach was used, and fire types with corresponding vegetation classes (no water) were rescaled so that they always cover 100% of the pixel.

GFASv1.0 uses a dominant fire type map. The interpretability of the dominant fire type or dominant land cover is very constrained in areas with strong spatial heterogeneity of the vegetation cover. We analysed this aspect using the MCD12C1.051 data (UMD legend) of the year 2001, gridded to 0.5 degree horizontal resolution.

Figure 35 illustrates that the maximum fractional contribution of any land cover class in a 0.5 degree grid cell varies strongly across the regions, and that several land cover classes may occur within the same grid cell (Figure 36a). Strong heterogeneity in the vegetation cover characterises the boreal belt in particular: Here, the maximum area contribution of any vegetated land cover class frequently does not exceed 30%, and typically, four different land cover classes contribute more 10% to the total grid area. In a substantial

number of grid cells, two land cover classes contribute more than 30% each to the grid cell area (Figure 36b). In these regions, the dominant fire or land cover class is of limited use to fully characterise the actual fire and emission behaviour since it ignores the contributions of the subsequently dominant classes.

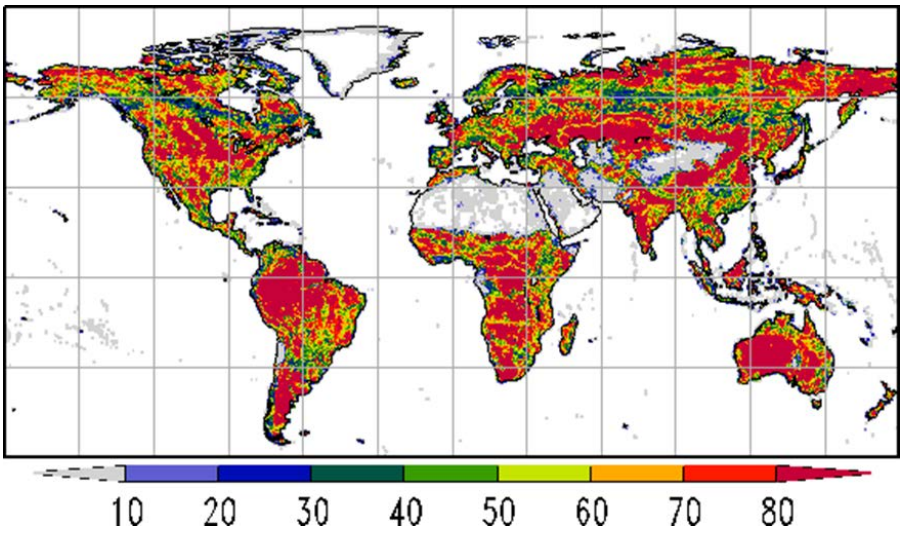

Figure 35: Maximum % area contribution of any UMD land cover class (excluding water) in a 0.5 degree grid cell.

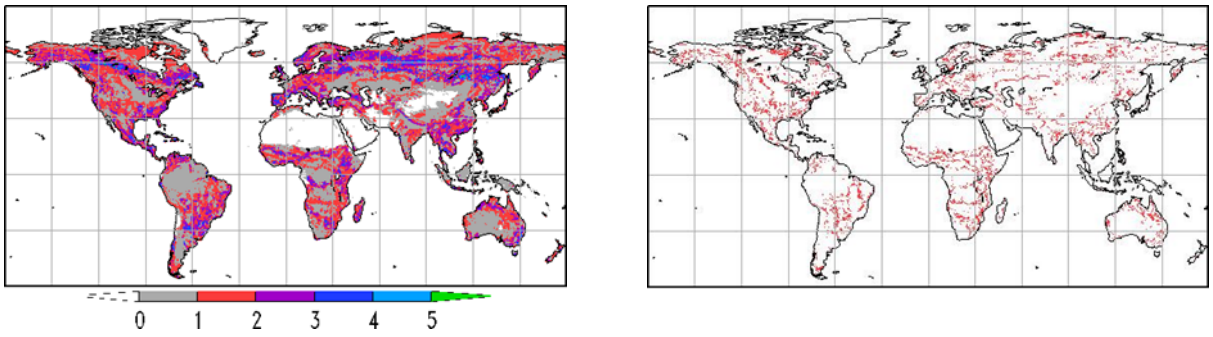

Figure 36: a) Number of UMD land cover classes with an area contribution greater than 10% (left) and b) grid cells where two land cover classes contribute at least 30% to the grid cell area (marked in red) (right).

From our detailed analysis, we conclude that the percentage fire type map (Option 4), derived by attributing MODIS FRP to a vegetation cover type at the native resolution (1 km), appears to be the best solution to realistically estimate actual fire emissions. A disadvantage of the fire type approach is that areas without fire occurrence cannot be adequately mapped. At this resolution however, the differences between the relative land cover and relative fire type are small (Table 10). Therefore, the relative land cover type, corrected for water, will be used to map areas of no fire occurrence.

For the enhanced GFAS version, the fire biome map will be updated annually. Due to instabilities in satellite-derived land cover products, we will use a 3-yr running mean, rather than the data of the single last year. For grid cells with fire occurrence in only one or two out of the three years, the missing year(s) will be filled in by the land cover fraction, so for these grid cells a mean of fire type and land cover fraction will be calculated.

3.1.5 Improved representation of peat areas

The Harmonized World Soil Database (HWSD) combines regional and national updates of soil information worldwide (European Soil Database, SOTER, Soil Map of China, WISE) with information from the FAO-UNESCO Soil Map of the World (FAO-DSMW). HWSD Version 1.21 (March 7, 2012) contains recent updates for the bulk densities from WISE/SOTWIS/ESDB[5].

For each mapping unit, the HWSD soil attribute database contains information on the soil classification and various soil properties, subdivided into top- and subsoil. The soil classification information comprises a) the major soil groupings ($HWSD_{msg}$) and b) the original classifications in the FAO 1974, 1985 and 1990 legends.

Figure 37 shows the spatial extent of areas classified as histosols using the $HWSD_{msg}$ classification and the additional histosol areas when all mapping units classified as histosols in any legend ($HWSD_{all}$)[6] are taken together. The figure shows that the reclassification of the original FAO legends into $HWSD_{msg}$ leads to a drastic change in peatland areas globally, depicting how strongly the mapping of peat areas depends upon the legend used. For example, in the original FAO legend, large areas in Alaska are mapped as histosols (roughly 0.07 mio km^2). None of them are represented as histosols using the $HWSD_{msg}$ data. Yet, according to Lappalainen (1996), there are indeed more than 0.1 mio. km^2 of peat areas in Alaska.

Globally, the histosols make up an area of 2.66 mio. km^2 in the $HWSD_{msg}$ classification and 4.82 mio. km^2 in $HWSD_{all}$ approach. For comparison: The most commonly cited estimate of the global area of peatlands is 4 mio. km^2 (Strack 2008). A more recent study by Yu (2012) gives this number as the best estimate for the northern (boreal and subarctic, or circum-Arctic) peatlands, alone. Together with the area estimate of tropical peatlands of 0.44 mio. km^2 by Page et al. (2010), the global area of peatlands more likely approximates 4.5 mio km^2. It thus appears that the $HWSD_{all}$ approach, at least in terms of global area estimates, more realistically represents the actual peatland areas than the $HWSD_{msg}$ classification, which results in a distinctively lower area extent.

[5] The inventory is downloadable from http://webarchive.iiasa.ac.at/Research/LUC/External-World-soil-database /HTML/HWSD_Data.html?sb=4 as 0.0083 deg rasterised data.

[6] HWSD soil attributes query = ([Su_symbol] = "HS") or ([Su_sym74] = "O*") or ([Su_sym90] = "HS*") or ([Su_sym85] = "O*")

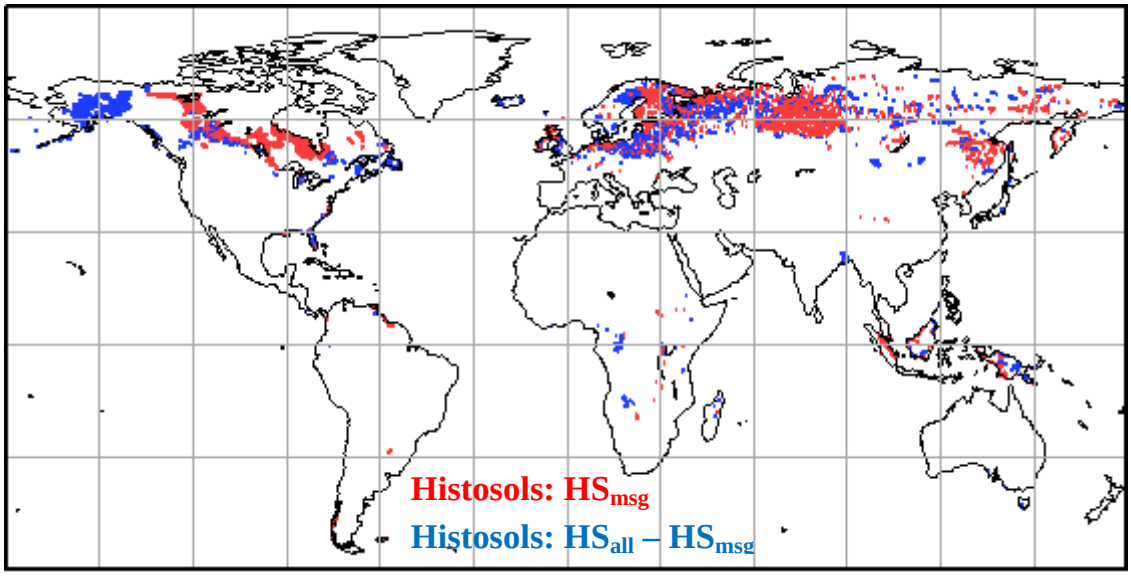

Figure 37: Distribution of mapping units classified as histosols (peat soils) in HWSD dataset i) the using the major soil groupings histosol (HS_{msg}) legend (red) and ii) additional histosol areas when all mapping units characterised as histosol (in any soil legend) are included (HS_{all}) (blue).

A comparison with the PEAT and OS areas used in GFASv1.0, however, is limited because of the different approaches used. The areas mapped as PEAT in GFASv1.0 cover 1.4 million km^2, and they only occur in Indonesia and Russia. In GFED3, peat areas are only explicitly parameterised for Indonesia. For the other peat areas of the world, peat fires are treated together with any burning of soil organic matter.

3.2 Conversion of FRP to dry matter burnt and emissions

Using monthly time series of GFED3 dry matter burned and GFASv1.0 ffxr FRP estimates over the period 2003 to 2011 (both cleaned for NBB signals, see also section 2.4.1), conversion factors for the four translation schemes defined in Table 9 have been calculated using the similar approach as in Heil et al. (2010). For this exploratory analysis, the predominant land cover of the year 2005 at 0.5 degree was used. As a next step, the percent fire type map in combination with the percent land cover map (Section 3.1.4) will be used to calculate a refined set of conversion factors for the enhanced GFAS system.

As in GFASv1.0 (see also Heil et al., 2010 and Kaiser et al., 2012), the zero-forced slopes of the regression of monthly GFED dry matter burned rates with GFAS FRP yield the lowest conversion factors for areas with no or relatively sparse tree cover, such as grass-, crop- and shrublands. At the same time, they yield the highest conversion factors for boreal forest (Table 11). The BORFOR conversion factor from this calculation is 18% lower the EFOS conversion factor in GFASv1.0, but 160% higher than the EF conversion factor. For EFOS, GFED3 assumes a substantial amount of soil organic matter to burn in addition to the surface fuels, which partly explains the higher conversion factor. Because of the much larger definitional range for the fuel category EF in GFED3 and GFASv1.0, a substantial fraction of the areas classified as EF are now treated as GRAS, which has a 57% lower conversion factor than BORFOR.

The changes in the conversion factors between the different translation schemes are relatively small (within 4% with respect to T1). As in GFASv1.0, the fuel types boreal forest and savannah show the highest fit to the linear regression model (R^2 of 0.82 and 0.88, respectively) (not shown).

ID	Fuel type	Conversion factor [kg dry matter per MJ FRP]				GFASv1.0*
		T1	T2	T3	T4	
1	BORFOR	1.27	1.23	1.27	1.23	1.55/0.49
2	TEMFOR	0.62	0.62	0.62	0.62	-
3	TROFOR	1.04	1.04	1.04	1.04	-/0.96
4	SHRUB	0.45	0.45	-	-	-
5	SAVA	0.90	0.91	0.87	0.88	0.26/0.78
6	GRAS	0.55	0.55	0.55	0.55	-
7	CROP	0.41	0.41	0.41	0.41	0.13/0.29
Global	GLOBAL	0.86	0.86	0.86	0.86	(w/o OS)

*Table 11: Slope of the linear regression of GFED3 dry matter burned and GFASv1.0 FRP over the period 2003 to 2011. GLOBAL refers to the result of the calculation without segregation into fuel types. *For comparison, conversion factors used for GFASv1.0 as described in Kaiser et al. (2012) are presented (with OS/without OS).*

Table 12 demonstrates that the dry matter burned estimates from the four translation schemes yield relatively similar results (largest deviation from T1 is within 0.6%); and all of them are only between 0.9 and 0.3% lower than the corresponding GFASv1.0 estimate. The lower estimate can be in one part attributed to the omitted representation of soil organic matter burning (PEAT and OS) in this calculation, but also to the masking of GFAS FRP for spurious signals prior this analysis. PEAT and OS typically yield higher conversion factors than "pure" surface fuel fires (Heil et al., 2010).

ID		Mean annual dry matter burned [Tg dry matter per year]			
		T1	T2	T3	T4
1	BORFOR	226	166	226	166
2	TEMFOR	52	52	52	52
3	TROFOR	828	828	828	828
4	SHRUB	133	133	0	0
5	SAVA	2631	2693	2786	2849
6	GRAS	145	145	145	145
7	CROP	125	125	125	125
Global	SUM	4140	4143	4162	4165
Corresponding global GFED3 estimate:			*3960*		*Tg per year*
Corresponding global GFASv1.0 estimate:			*4179*		*Tg per year*

Table 12: Estimated mean annual total dry matter burned in the four translation schemes.

We tested the sensitivity of the conversion factors and the estimated dry matter burned estimates for the default translation schemes T1 when using the improved peat representation (Section 3.1.5). This representation increases global dry matter burned estimate by 1.3% compared to the translation scheme without differentiation between peat and non-peat areas. The estimated dry matter burned estimate is 0.3% higher than in the GFASv1.0 version.

On a global scale, the changes in estimated annual dry matter burned rates introduced by a) modifying the surface fuel map and/or b) the representation of peat areas are relatively small (within around 1% when compared to GFASv1.0). However, regionally and at higher temporal resolution, the changes are of greater relevance, notably in boreal regions.

We also tested the changes introduced by modifying the translation scheme and the emission factor compilation on the global total CO emissions.

ID	Conversion factor [kg dry matter per MJ FRP]			
	Fire type	T1	T1 PEAT	T1 NOPEAT
1	**BORFOR**	1.27	1.29	1.26
2	**TEMFOR**	0.62	0.44	0.64
3	**TROFOR**	1.04	4.77	0.93
4	**SHRUB**	0.45	2.70	0.40
5	**SAVA**	0.90	1.16	0.90
6	**GRAS**	0.55	0.46	0.55
7	**CROP**	0.41	0.45	0.40
Global	**GLOBAL**	0.86	1.74	0.84

ID	Mean annual dry matter burned [Tg dry matter per year]				
	Fire type	T1	T1 PEAT	T1 NOPEAT	T1 PEAT+NOPEAT
1	**BORFOR**	226	48	181	229
2	**TEMFOR**	52	3	50	53
3	**TROFOR**	828	180	709	889
4	**SHRUB**	133	22	116	138
5	**SAVA**	2631	57	2579	2636
6	**GRAS**	145	2	143	145
7	**CROP**	125	9	114	123
Global	**SUM**	4140	284	3909	4193
Corresponding global GFED3 estimate:		*3960*			*Tg per year*
Corresponding global GFASv1.0 estimate:		*4179*			*Tg per year*

Table 13: Estimated conversion factors and mean annual total dry matter burned in the translation scheme T1 when differentiating for peat and non-peat areas.

ID	EF: A&M09	Mean CO emissions [Tg per year]			
	Fuel type	T1	T2	T3	T4
1	**BORFOR**	23.9	17.6	23.9	17.6
2	**TEMFOR**	5.3	5.3	5.3	5.3
3	**TROFOR**	83.5	83.5	83.5	83.5
4	**SHRUB**	8.2	8.2	0.0	0.0
5	**SAVA**	161.7	165.6	171.3	175.1
6	**GRAS**	8.9	8.9	8.9	8.9
7	**CROP**	11.5	11.5	11.5	11.5
Global	**SUM**	303.0	300.5	304.3	301.9

ID	EF: AK11	Mean CO emissions [Tg per year]			
	Fuel type	T1	T2	T3	T4
1	**BORFOR**	28.6	21.1	28.6	21.1
2	**TEMFOR**	4.6	4.6	4.6	4.6
3	**TROFOR**	76.9	76.9	76.9	76.9
4	**SHRUB**	9.0	9.0	0.0	0.0
5	**SAVA**	165.4	169.3	175.1	179.1
6	**GRAS**	9.1	9.1	9.1	9.1
7	**CROP**	12.8	12.8	12.8	12.8
Global	**SUM**	306.4	302.7	307.1	303.5
Corresponding global GFED3 estimate:			*328.2*		*Tg per year*
Corresponding global GFASv1.0 estimate:			*342.9*		*Tg per year*

Table 14: Estimated mean annual CO emissions in the different translations schemes without differentiating for peat and non-peat areas using (a) the Andreae and Merlet (2001, with updates 2009) emission factors (A&M09) (top) and (b) the Akagi et al. (2011) emission factors (AK11).

Modifying the translation scheme changes mean annual global CO emissions by up to 1.2% with respect to T1. Using the Andreae and Merlet (2001, with updates 2009) emission factor compilation instead of Akagi et al. (2011), results in a similar change.

To test the effect of differentiating between peat and non-peat areas on global annual CO estimates, we assumed that the Akagi et al. (2011) emission factor for peat applies to 90% of the dry matter burned in grid cells occurring in peat areas (and the remainder the corresponding surface vegetation emission factor). Compared to a default translation scenario without differentiating between fires in peat and non-peat areas, a differentiation leads to an increase in global CO emissions by 3.6%. However, the global CO emissions are still distinctively lower than in the GFASv1.0 estimate.

ID	EF: AK11	Mean CO emissions [Tg per year]			
	Fuel type	T1	T1 PEAT	T1 NOPEAT	T1 PEAT+NOPEAT
1	**BORFOR**	28.6	5.2	22.9	28
2	**TEMFOR**	4.6	0.3	4.4	5
3	**TROFOR**	76.9	18.8	65.8	85
4	**SHRUB**	9.0	2.3	7.8	10
5	**SAVA**	165.4	5.8	162.1	168
6	**GRAS**	9.1	0.2	9.0	9
7	**CROP**	12.8	0.9	11.7	13
Global	**SUM**	306.4	33.5	283.7	317.3
Corresponding global GFED3 estimate:			*328.2*		*Tg per year*
Corresponding global GFASv1.0 estimate:			*342.9*		*Tg per year*

Table 15: Estimated mean annual CO emissions in the translation scheme T1 when differentiating for peat and non-peat areas.

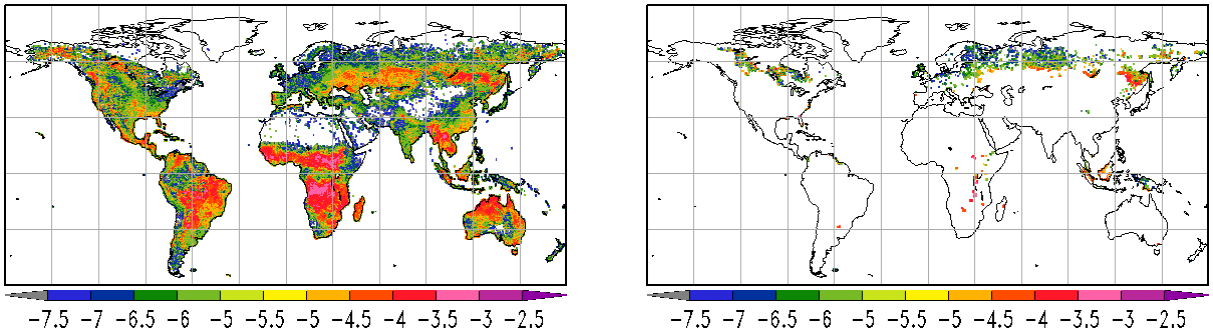

Figure 38: Mean annual CO emissions (log10 kg m^{-2} a^{-1}) in the T1 scenario with peat (left) and difference to the T1 scenario with no peat (log10 kg m^{-2} a^{-1}) (right).

Figure 38 illustrates that while the relative change of modifying the representation of peat areas are relatively small in respect to global total CO emissions, they lead to strong changes in the regional emission budgets, notably in the boreal regions.

The relatively small sensitivity of the global dry matter burned estimates to the translation schemes pinpoints the limits of the scaling approach: GFAS FRP for each fuel category is scaled to GFED3 monthly dry matter burned totals by linear regression; inevitably, the global totals will be largely similar to GFED3 totals. This simplistic, fuel-type average scaling does not resolve the influence of fuel moisture or the spatial heterogeneity in fuel loading and arrangement on the conversion factors. We therefore recommend in-depth studies focusing on the physical understanding of factors controlling the spatial and temporal variability in the conversion factors (see also Section 3.3). First exploratory studies showed that the fractional tree cover, the tree cover height and the relative contribution of peat burning are important parameters. Changes in the fuel and soil moisture conditions are likely influencing parameters, too. This will be analysed in more detail using multivariate regression statistics on a grid-cell level.

The scaling of GFAS FRP to GFED dry matter burned estimates inherently adopts the deficiency of the GFED3 approach, such as the underrepresentation of small fires and/or uncertainties in the CASA model and its input data. Understanding the physical processes such as the obscuring effects of tree cover will ultimately allow for physically more explicit parameterisations that make GFAS more independent from a scaling to GFED. For parameter optimization, such a model could - in the end - be dynamically linked to atmospheric observations.

3.3 Advanced approaches to estimate dry matter burned from FRP

3.3.1 Insights from combining burned area products with active fire information

Burned area products provide crucial information on fire size, and are less sensitive to cloud cover than active fire data. Therefore they are often used in combination with modelling to calculate total dry matter (DM)-burned (e.g. GFED). Active fire observations on the other hand have the advantage that they are observed in near-real-time, observe many small fires not observed by burned area products, and provide direct information about the energy release of fires. To date, MODIS sensors aboard the Terra and Aqua satellites provide highest quality global active fire observations at typically four moments of the day and are used for global DM-burned estimations (GFAS). The largest limitation to this method are a lack of continuous sampling by limited overpasses and cloud cover, and uncertainties on the relation between observed fire radiated power (FRP) and DM-burned. Therefore currently Fire Radiated Energy (FRE) is calculated using simplifications of the diurnal cycle and land cover specific conversion factors are needed to link FRE of to DM-burned, cf. Section 3.2.

A better understanding of the fundamental differences between burned area and active fire products can provide important insights on how to derive an updated, improved set of conversion factors. Here we provide the outline of research that will commence at VUA in spring 2014, and discuss some preliminary results.

Burned area and active fire products

Although both burned area (GFED) and active fire (GFAS) based emission products have been used widely in global and regional scientific studies, much remains unknown about the exact relation of both products. A better basic understanding of the relation between burned area and active fire products is required to understand the background of current conversion factors. Therefore we make a global comparison between burned area and active fire observations at a 1-km resolution. Preliminary results reveal that the ratio of active fire to burned area observations for a given area is related to speed and persistence of fire that in turn are dependent on fuel type and conditions (Figure 39). Additionally, we find that many active fires are observed for pixels without burned area observations; this is the result of the higher sensitivity of the active fire product to small fires. Observed FRP per fire count seems to be related to fire size, where large fires are often short in existence but are characterized high FRP (MW). Also, fire size is dependent on tree cover (or fuel type). These fire characteristics in combination with ignition policy are responsible for fire diurnal cycle that forms a crucial link between MODIS FRP observations and daily FRE. Errors in FRE estimation on their turn result in incorrect conversion factors between GFAS estimated FRE and GFED estimated DM-burned.

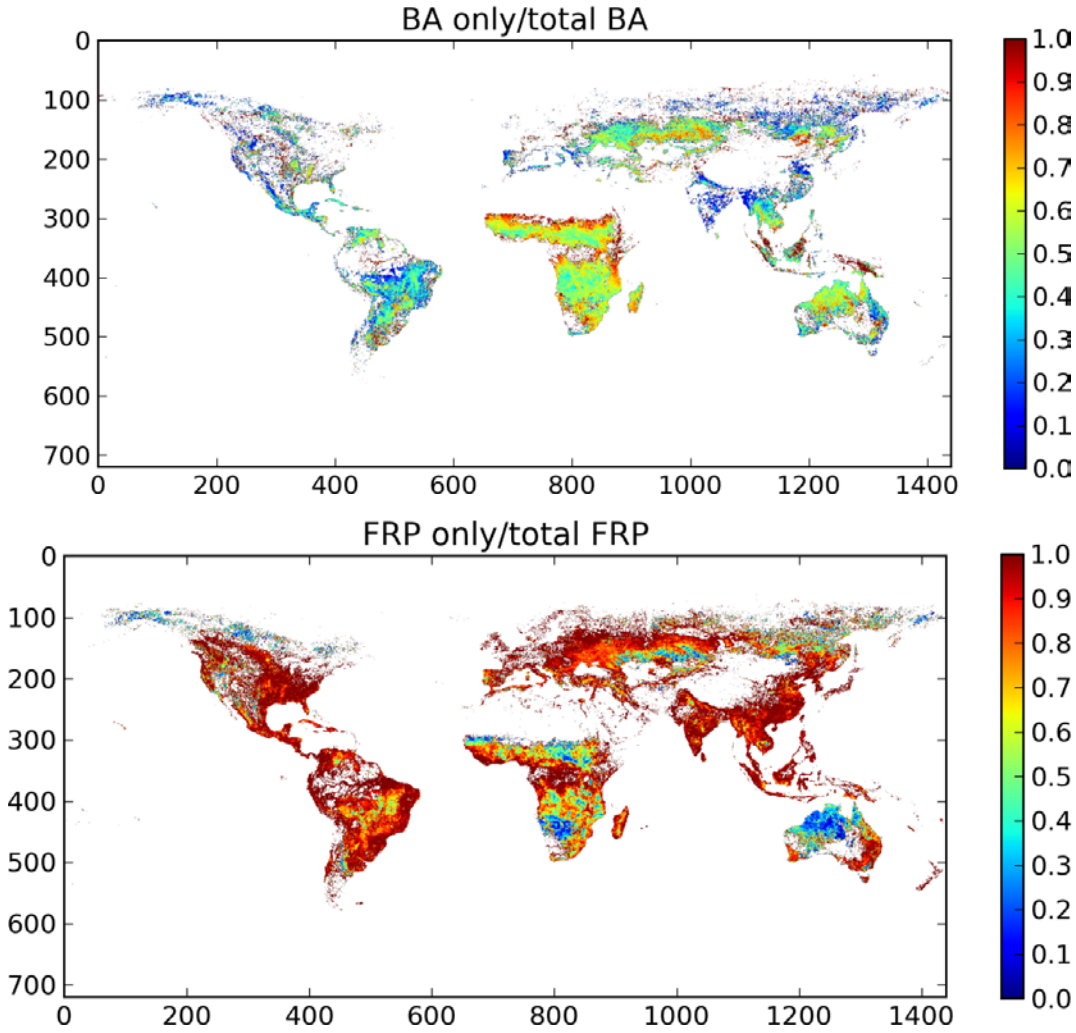

Figure 39: a) Burned area observations without corresponding active fire observation divided by total burned area (top) and b) FRP without corresponding burned area observations divided by total FRP (bottom).

3.3.2 Towards more comprehensive conversion factors

First we will make a new estimation of daily FRE for the MODIS data period, using the recommendations of the enhancements report. Main changes in calculation of FRE are the inclusion of a daily cycle model (see section 2.2.2), and a correction for the swath-dependence of MODIS fire observations (see section 2.1). Using our best estimate of FRE, we will calculate FRE for FRP observations with and without corresponding burned area observations. Preliminary results indicate that excluding small fires, undetected by the burned area product, provides new insights and clues on the origin of 'remaining' conversion factors. A clear relation between conversion factors and tree cover (or above ground biomass) was found (Figure 40 and Heil et al. 2010, Figure 4-6) however fire size that is negatively correlated with tree cover may also have a strong effect on FRP observations. Conversion factors may arise from erroneous FRP estimations by MODIS, caused by for example tree cover obscuring the fire or detection thresholds, but structural errors in one or both products (GFAS and GFED) processing chains may also play a role and will be subject to further investigations (or at least discussion). Overall the goal will be to structurally rule out possible causes of conversion factors resulting in increased insight of remaining conversion factors

and their causes and a better understanding of the quality of GFAS and the potential of MODIS observations to estimate daily DM-burned. When more physically based conversion factors are derived, and confidence in daily FRE estimations rises, the dependence of GFAS on GFED DM-burned estimations may be loosened. Top down approaches, using satellite column measurements in combination with atmospheric modelling may in the future also be used to derive conversion and emission factors.

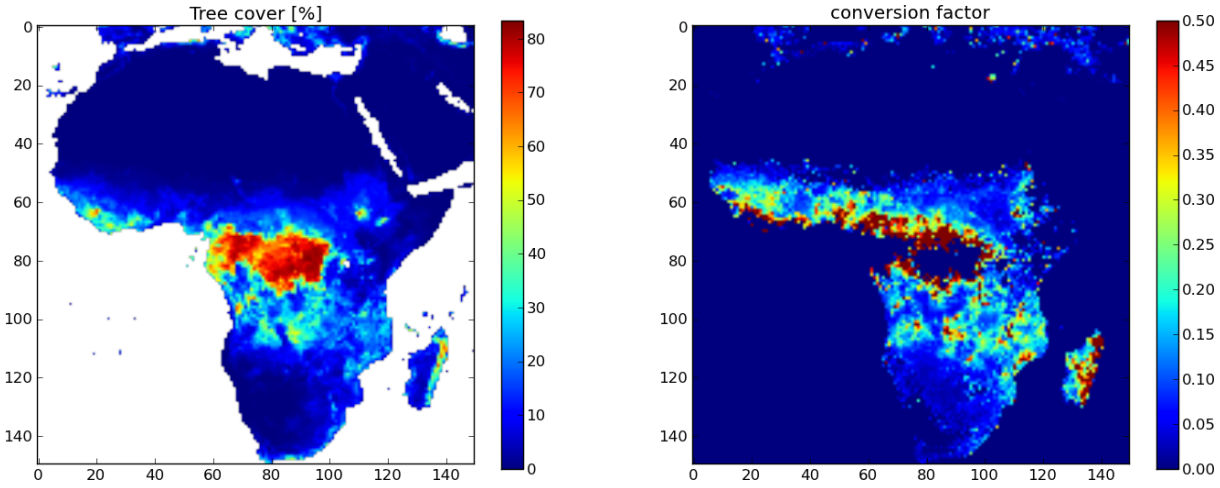

Figure 40: a) Tree cover of Africa (left) and b) Conversion factors for Africa when active fires outside burned area observations are discarded (note that these are preliminary results and cannot yet be compared to current GFAS conversion factors) (right).

3.4 Dynamic emission factors

The current version of GFAS relies on static emission factors (EFs) that are based on the arithmetic mean of field measurements. Biome-averaged EFs, compiled by Andreae and Merlet (2001) and updated by M.O. Andreae (Kaiser et al., 2012) were derived from measurements of fires in tropical forest, savannah and grassland, extratropical forest, tropical peat, and agricultural area. In addition to spatial variations due to vegetation types, the EFs that are currently used in GFAS neglect temporal variability that is often found. Several studies have shown considerable variability of EFs throughout the year (Hoffa et al., 1999; Hely et al., 2003; Korontzi et al., 2003), and they linked this to substantial seasonality of different environmental parameters found in most biomass burning regions, and also to variation in EFs across vegetation and different fuel types (Meyer et al., 2012; Wooster et al., 2011). Due to these findings, dynamic EFs should be explored within the GFAS modelling framework.

As a first step we will implement monthly varying EF fields – based on a global climatology – within the GFAS modelling framework. Specifically, for every biome an EF range (Table 10) is defined that is based on the EF compilation of Akagi et al. (2011) (See Sect. 2.1.1). Following a similar approach that is used in CASA-GFED (van der Werf et al., 2010) to scale the combustion completeness, we will use moisture conditions to scale between the minimum (arithmetic mean – 1SD) and maximum (arithmetic mean + 1SD) EF value that we set for each biome. The effects of seasonal changes in fuel moisture will be simulated by using the ratio of precipitation (PPT) over potential evaporation (PET) of the month of the fire and the previous month. To account for a longer memory of biomes with more coarse fuels (e.g. tropical and boreal forest) compared to biomes with a larger contribution of smaller-size fuels like grasses (e.g. savannas), the relative weighing of the current and previous month was different per biome (van

Leeuwen et al., 2013). Although, from a coarse resolution modelling perspective, exact relations between the fuel moisture values and EFs cannot always be extracted from the current body of literature, it likely explains a substantial part of the EF variability found (van Leeuwen and van der Werf, 2011).

Initially, we will focus on CO, CO_2 and CH_4 since for these main trace gases sufficient literature data is available to define a proper EF range. We also included seasonal variability for organic carbon (OC) and black carbon (BC), both important for the aerosol modelling community, but note that due to insufficient data available these estimates are quite uncertain. Besides expanding our work to other trace gases (like e.g. NO_x), a next important step in our work is increasing the temporal resolution from monthly to daily. Applying EF variability on a daily resolution will likely improve the representation of trace gas emission estimates, and moreover it allows us to explore the ratio of night- to daytime FRP from GFAS as a proxy for the modified combustion efficiency (MCE).

Species	Biome							
	TROFOR	BORFOR	TEMFOR	SAVA	CROP	PAST	SHRUB	PEAT
CO	66 – 120	82 - 172	57 - 121	44 – 80	69 - 135	97 - 173	54 - 80	122 - 242
CO2	1585-1701	1368-1610	1566-1708	1648-1724	1485-1685	1406-1690	1671-1749	1498-1628
CH4	3.1 - 7.1	2.8 - 9.1	1.5 - 6.3	1.1 - 2.8	2.3 - 4.1	3.4 - 13.7	1.8 - 3.2	4 - 19.6
OC	1.98 – 7.44	Na	Na	1.38 – 3.86	Na	5.30 – 14.0	Na	2.63 – 9.83
BC	0.24 – 0.80	Na	Na	0.17 – 0.57	Na	0.50 – 1.32	Na	0.09-0.31
MCE	0.89-0.94	0.84-0.93	0.89-0.95	0.93-0.96	0.88-0.94	0.94-0.92	0.93-0.95	0.80-0.89
Memory	50	50	30	10	20	50	10	10

Table 16: Overview of EF ranges (mean ± 1 SD) defined for 8 different biomes. The modified combustion efficiency (MCE) and memory function (van Leeuwen et al., 2013) — the contribution of the previous month's EF (%) – is also shown.

3.5 Emission factor update in literature

The current version of GFAS relies on emission factors compiled by Andreae and Merlet (2001, with updates, c.f. Kaiser et al., 2012). Because of several advantages (see also section 3.1.1), the more recent Akagi et al. (2011) (AK11) compilation will be used in the enhanced GFAS version. Table 17 shows the AK11 emission factors by AK11 fuel types.

EF in g per kg	BORFOR	TEMFOR	TROFOR	SHRUB	SAVA	CROP	PEAT
CO2	1489.4	1646.6	1643.20	1680.5	1685.8	1584.9	1601.0
CO	126.6	88.4	92.9	67.4	62.9	102.2	106.0
CH4	5.96	3.36	5.07	3.00	1.94	5.82	6.44
NMHC	5.69	3.69	1.70	**3.40**	3.40	9.89	5.69
H2	1.78	2.03	3.36	**1.70**	1.70	2.59	1.78
NOx	0.90	1.91	2.55	**3.65**	3.92	3.11	0.80
N2O	0.41	0.16	0.28	0.25	0.21	0.10	0.41
PM2p5	15.33	12.61	9.86	7.06	7.17	6.26	15.33
TPM	17.62	15.31	13.00	15.37	8.51	12.37	17.62
TC	8.28	6.76	5.24	5.01	3.00	3.05	7.43
OC	9.14	6.92	4.71	3.70	2.62	2.30	6.79
BC	0.56	0.54	0.52	1.31	0.37	0.75	0.64
SO2	1.00	1.10	0.40	0.68	0.48	0.48	1.00
Ethane	1.79	0.63	0.71	0.42	0.66	0.91	1.79
Methanol	2.82	1.73	2.43	1.35	1.18	3.29	2.95
Ethanol	0.05	0.10	0.05	0.06	0.05	0.05	0.05
Propane	0.44	0.22	0.13	0.54	0.10	0.28	0.44
Ethylene	1.42	1.17	1.06	1.01	0.82	1.46	1.31
Propylene	1.13	0.61	0.64	0.48	0.79	0.68	0.61
Isoprene	0.15	0.10	0.13	0.05	0.04	0.38	0.22
Terpenes	0.22	0.96	0.12	0.01	0.01	0.01	0.22
Toluene_lump	1.77	0.00	0.75	0.73	0.29	0.34	0.79
Higher_Alkenes	0.53	0.00	0.09	0.31	0.11	0.35	0.53
Higher_Alkanes	0.30	0.00	0.08	0.17	0.05	0.14	0.30
Formaldehyde	1.86	2.08	1.73	1.33	0.73	2.08	1.67
Acetaldehyde	0.98	0.77	1.55	0.56	0.57	1.24	1.55
Acetone	0.75	0.54	0.63	0.31	0.16	0.45	0.63
NH3	2.72	0.84	1.33	1.20	0.52	2.17	1.10
DMS	0.005	0.008	0.001	0.001	0.001	0.001	0.005
HCN	1.52	0.72	0.42	0.75	0.41	0.29	0.66

values from BORFOR

values from SAVA

values from mean of SA and EF

values from mean of BORFOR and TROFOR

values from mean of BORFOR and TEMFOR

letters in black: values from Akagi et al. (2011) v3

letters in red: values from Andreae&Merlet(2001, with updates 2009) because no Akagi et al. 2011 values are available

Table 17: Emission factors (g species per kg dry matter burned) to be used in the enhanced GFAS version for the AK11 fuel types defined in Table 8. When emission factors are not specified in AK11, they are complemented by the corresponding values of Andeae & Merlet (2001, with updated 2009). If no emission factors are specified in neither of them, they were estimated from the emission factors of other fuel types.

Table 18 demonstrates that applying the AK11 emission factors instead of the Andreae&Merlet (2001) compilation so far used in GFASv1.0 leads to strong changes in the global emission budgets of individual species.

	Yearly global totals in Tg				% change to GFASv1.0	
	GFASv1.0		GFASv1.0(AK11)			
SPECIES	2007	2008	2007	2008	2007	2008
CO	340.7	325.9	341.1	330.5	0%	1%
NOx	9.8	9.4	14.0	12.8	43%	37%
SO2	2.2	2.1	2.2	2.2	-3%	1%
NH3	5.3	6.2	4.7	5.2	-10%	-16%
H2	7.6	6.7	9.5	8.6	25%	28%
CH3OH	8.8	8.4	7.6	7.3	-14%	-12%
C2H5OH	0.08	0.07	0.24	0.22	211%	211%
C3H8	1.6	1.3	0.2	0.2	**-85%**	**-82%**
C2H4	4.6	4.3	4.1	4.0	-11%	-8%
C3H6	2.7	2.5	3.5	3.5	30%	39%
C5H8	0.5	0.5	0.4	0.4	-16%	-11%
Terpenes	0.3	0.3	3.0	3.1	1054%	1072%
Toluene_lump	2.8	2.9	2.6	2.9	-5%	-2%
Higher_Alkenes	1.7	1.5	0.9	0.9	**-47%**	**-44%**
Higher_Alkanes	0.7	0.7	0.4	0.5	**-41%**	**-32%**
CH2O	5.4	5.0	4.9	4.6	-10%	-8%
C2H4O	4.6	4.1	3.9	3.6	-15%	-11%
C3H6O	2.4	2.4	1.5	1.5	**-37%**	**-37%**
C2H6S	0.2	0.2	0.0	0.0	**-97%**	**-96%**
C2H6	2.5	2.3	3.3	3.3	31%	46%

Table 18: Annual global total emissions of individual species in the years 2007 and 2008 in a) GFASv1.0 and b) GFASv1.0 using the Akagi et al. (2011) instead of the Andreae & Merlet(2001, with updates 2009) emission factor compilation.

4 System Extensions

4.1 Forecast of fire activity: Analysis system to compute and compare global Fire Weather Indices to (GFAS) MODIS Fire Radiative Power observations

Introduction and science background

Wildland fire is a significant source of emissions of CO2 at the regional and global scale. The GFAS product [Kaiser et al., 2012] utilises satellite observations of Fire Radiative Power (FRP) to estimate gas and aerosol emissions by way of emission factors: linear multipliers that convert radiance to emissions via biomass burned. GFAS uses a Kalman filter to combine FRP measurements at multiple time-scales. The filter employs a unity operator to innovate FRP forward in time, such an assumption may lead to unrealistic estimates of emissions when there are few available observations. For example, if fires are extinguished in a particular area due to sudden changes in weather (e.g. heavy rain) the algorithm has no way of predicting this until a new observation is filtered.

The Canadian Fire Weather Index System (hereafter referred to as the FWI system) is a suite of empirical forest fire danger rating indices calculated from meteorological data [van Wagner, 1987]. There is evidence to support the hypothesis that fire weather indices have at least some predictive ability on the occurrence of fire as detected by active fire products. Pappenberger [2012] conducted a global analysis of the relationships between dry matter combustion rate, derived from GFAS FRP, and fire weather index (FWI). Pappenberger [2012] found regional scale relationships between the GFAS derived product and FWI of varying strength. Strong correlations were found in South America. Other regions such as Australia and the Mediterranean showed no such relationships; Pappenberger [2012] explained this as being due to human influence.

The code developed in this study was used to compare the FWI system to GFAS FRP observations (replicating the Pappenberger [2012] study). The code is designed as a modular codebase that can be run on a desktop computer at the global scale. The code provides the following opportunities for future development:

i. has the potential develop a tool to improve GFAS FRP by integrating fire weather into the filtering algorithm;
ii. be used to further explore relationships between active fire remote sensing observations and weather variables (see future work).

Although point i. was not addressed by the end of the preliminary study described herein (i.e. no system was developed to improve GFAS measurements), correlations were observed between FWI and FRP and the code is now being actively developed and used as part of Mark de Jong's (King's College London) PhD project (see Future work).

Methods and Codebase

After calculating FWI from weather data, FRP and FWI data were grouped in continental-like regions (see Figure 42 for region bounding boxes) and then the relationships between the variables were analysed.

The code consists of a mix of (mainly) python, FORTRAN (for speeding up some of the slower routines) and C++ code (Canadian Forestry Service FWI system code). The relationship between the various scripts is show in Figure 41.

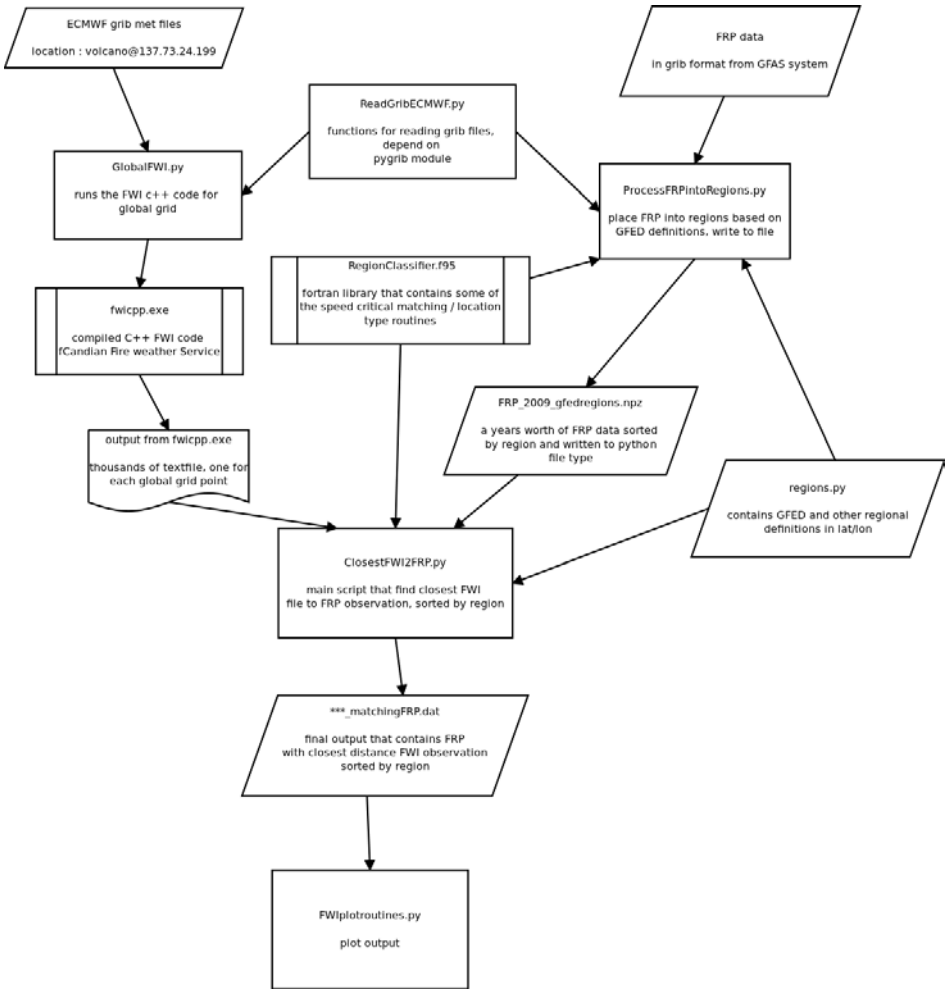

Figure 41: Flowchart describing system flow. The arrows represent dependencies and the order of processing. The python scripts are usually executed one at a time, i.e. there is not a single main' that controls the whole system.

There is no 'main' program, rather there are 3 main parts to the code:

i. FRP pre-processing

The world is divided into several continental-type Region Of Interest (ROIs). The ROIs are based on definitions used by the GFED system (http://www.globalfiredata.org/, see Figure 42). The code steps through each day of the year and sorts GFAS Fire Radiative Power data into the appropriate region.

ii. FWI processing

FWI (and associate indices) are calculated for a global grid for each day of the year using C++ code written by Alan Cantin at the Canadian Forest Service (CFS). The FWI code requires meteorological data as inputs (e.g. temperature, rain etc). GRIB files from ECMWF were downloaded and used for this purpose.

iii. Comparison of FWI to FRP

Once FRP has been processed into regions and FWI has been calculated, the system has the data available to make comparisons between FRP and FWI (or other sub-indices of the FWI system). Then regression analyses are performed.

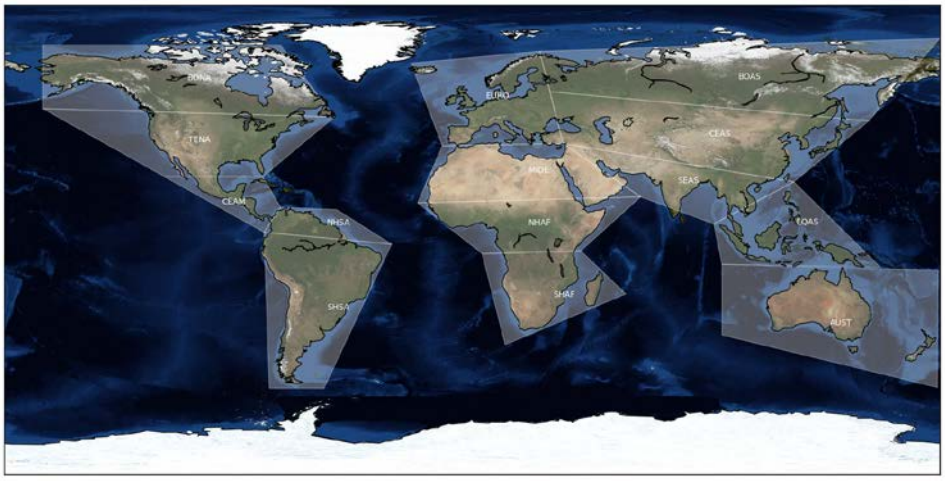

Figure 42: ROIs based on the GFED system.

Preliminary results

The relationships between simple FRP and FWI statistics (sum, mean) for ROIs were analysed for a year's worth of data (2009). Figure 43 shows the relationships between the daily sum of FRP and daily sum of FWI for each region. There is a clear relationship present for some regions, e.g. EURO (Europe), but in some regions sum FWI appears to have little predictive power, e.g. CEAS (central Asia). This suggests that the FWI system has the potential to be used as a predictor of low FRP values for some regions. Pappenberger [2012] also found a regional dependency on the predictive skill of the FWI system, which is to be expected as the FWI system was developed for a specific region/country (Canada). Unlike daily sums, there were no clear relationships between daily mean FWI and mean FRP (not shown) for the GFED like regions.

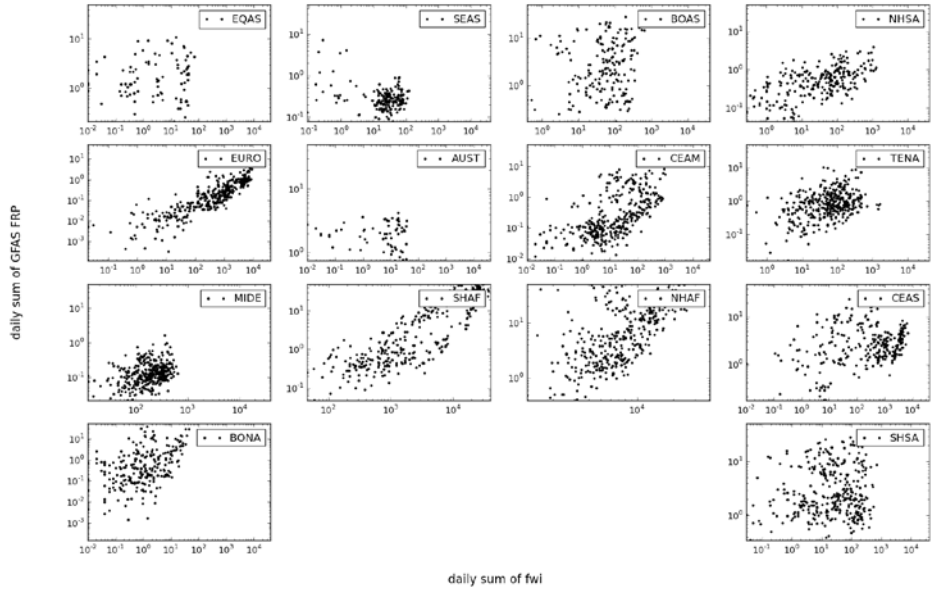

Figure 43: Daily sum of FRP versus daily sum of FWI for ROIs.

Current issues and areas for future development

There are a number of issues relating to the project in its current state, and these will be addressed in future work:

- Does the FWI system give the expected results?
- Are there any bugs or issues with i/o? There is a spreadsheet version of FWI system to validate the C++ code.
- Which is the most appropriate fire weather index to compare to FRP?

It is likely that the final FWI index from the FWI system is not actually the best fire behaviour predictor in all environmental settings. Different sub-indices of the FWI contain different amounts of information relating to soil moisture layers and meteorology. The Initial Spread Index, for example, may have greater predictive power than FWI in regions with shallow soils and non-forest vegetation, as this index is more strongly influenced by fine fuel moisture and wind speed.

Calibration of the FWI system for global data

The FWI system was designed for Canada, however it has been previously applied to many different regions around the world, including the USA, China, Argentina, Europe [Taylor & Alexander, 2006] and South East Asia [De Groot et al., 2007]. The rationale for applying an empirical model globally needs to be assessed, and an investigation will be made into incorporating region-specific parameters where possible.

FWI inputs

We currently use 0 hour data for all meteorological inputs to drive FWI except for rain where I use the 24 hr predicted value. This is because the total precipitation value at 0 hours is 0! It is probably not correct to use this value.

Processing time

A global dataset takes about 24 hr to process for a year's worth of driver data at 0.5 deg resolution. This could be sped up as the FWI processing is easily parallelised, as adjacent grid cells have no influence on each other.

4.2 Injection height

The biomass burning emissions that are provided by GFAS to the MACC forecasting system are currently being emitted at the surface. They are then vertically and horizontally transported by the MACC system. However, observations show that for large intense fires, emissions can be released above the boundary layer and even in the case of an extreme scenario in the stratosphere, as it happened during the large Colorado fires that occurred in June 2013 with emission measured up to 13 km. As wind patterns are usually rather different above the boundary layer as compared to below, this can result in a discrepancy between modelled and observed plume transport. An important development of the MACC FIR team is to try to estimate the injection height for large fires that release enough energy to trigger a strong updraft, which can send emission far above the boundary layer.

4.2.1 Plume Rise Model (PRM)

Our approach is based on the plume rise model (PRM) developed by Freitas et al (2007), which models both effects of atmospheric stability and latent heat. The original PRM was modified so that instead of using parametric value of energy flux released from a fire, the input data of convective heat flux and Active Fire area are directly defined from FRP data evaluated with a modified version of the Dozier algorithm (Dozier 1981) applied to the MOD12 product. Furthermore the dynamical core of the plume model is modified with a new entrainment scheme inspired from results in shallow convection parameterization (Pergaud et al 2009). Such convection scheme allows the PRM to estimate the detrainment of the plume. The emission can then be spread over a profile rather than being released at the top altitude of the plume as it was previously done in the PRM of Freitas et al (2007). The constants that are used in the convection scheme are determined through an optimisation algorithm based on (i) fire plume characteristics of single fire events extracted from the official MISR plume height project and (ii) atmospheric profile derived from the ECMWF analysis.

As shown in previous work (Freitas et al 2007, Val Martin et al 2009) the state of the atmosphere is an important factor of the plume dynamics, as it controls the entrainment and therefore the heat release by latent heat which is the main parameter responsible of the pyroconvection mechanism. To get the best information on the atmospheric local state, atmospheric profiles are evaluated at the location of the fire from the ECMWF forecasts at a 3h time resolution. The total column water vapour is also extracted from the ECMWF data to compute the transmittance of the atmosphere and correct the MODIS radiance used in the Dozier algorithm.

The aim of this new PRM is to predict the entrainment and detrainment profiles of the ground emissions from fires; it is based on the assumption that

- meteorological data are not affected by the fire and
- the fire and the plume are circular.

In the PRM, a fire is defined as a cluster of fire pixels and the FRP and the Active Fire Area are derived for the entire cluster. As we are only focusing on injection heights from large fires, the PRM is only run for the fires with an Active fire area greater than 1 ha. Validation of the PRM was carried out against MISR data and gave satisfactory results.

Figure 44 shows an example of the output of the PRM for a given fire.

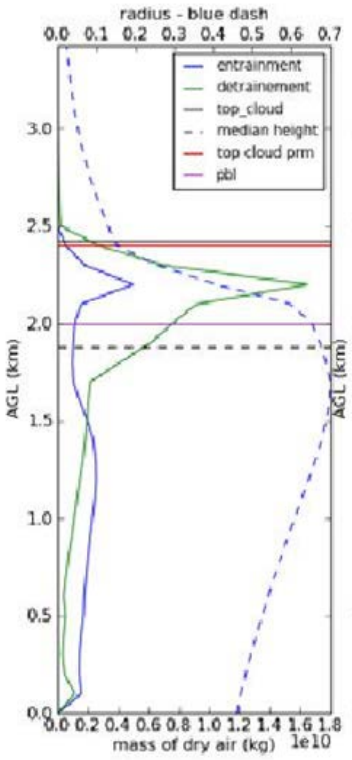

Figure 44: Example of an output of the PRM, showing the entrainment (blue) and detrainment (green) profiles of fire emissions as a function of height. The top of the boundary layer is indicated by a pink horizontal line at a two-kilometre height.

4.2.2 Coupling with GFAS

The Plume Rise Model was adapted to be run together with GFAS. The inputs of both systems are the same: raw satellite and land cover data. The output of the PRM was modified so that it could be treated by the gridding and averaging routines of GFAS. While FRP is averaged within each global grid cell with observation area as a weight, it was chosen to keep only the maximum values for injection heights in the averaging routines. This choice is justified by the fact that we want to concentrate on the largest fires. Out of the detrainment profile that was provided by the PRM, the height of the bottom of the plume, of the

maximum detrainment and of the top of the plume was kept for gridding in GFAS. These three parameters are then assimilated in GFAS in the same way as the FRP, so as to provide daily information about the injection heights.

Figure 45 shows an example of gridded daily assimilated maximum injection height for an intense fire. The height above which most emissions take place reached 6500m as computed by the PRM.

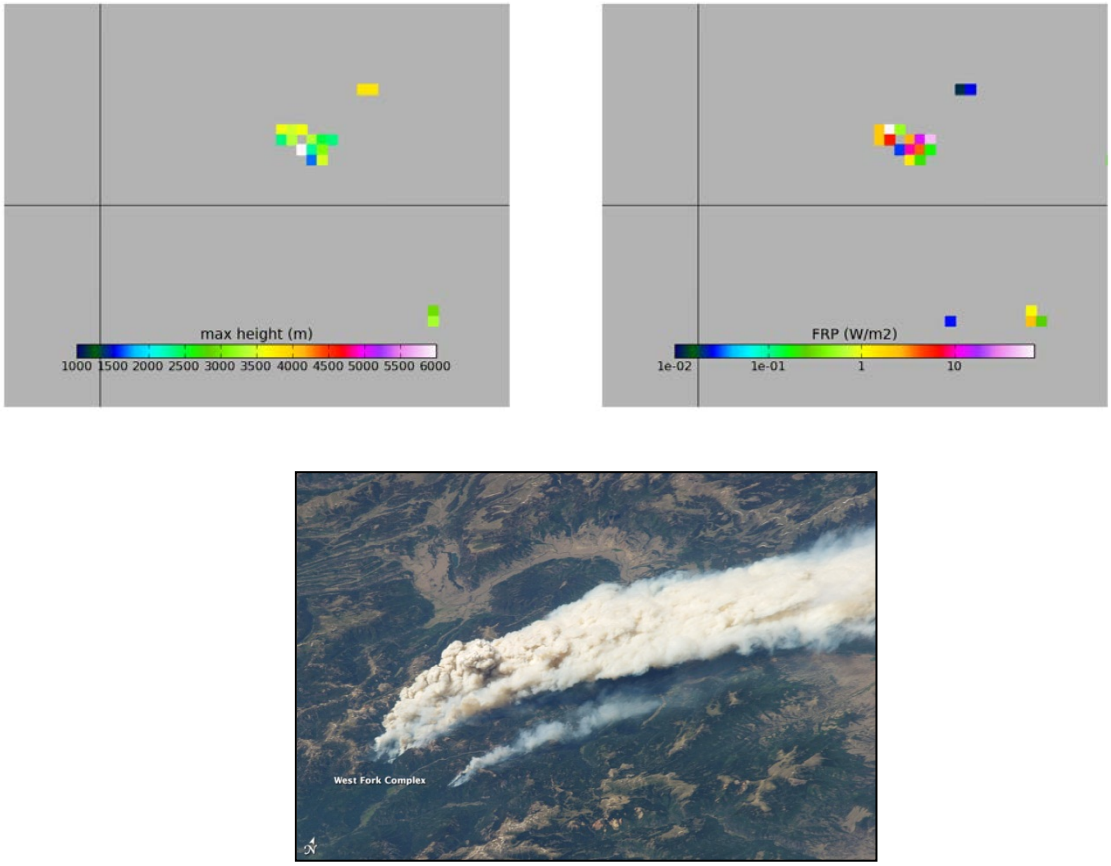

Figure 45: Height of maximum injection (top left), FRP (right) of the West Fork Complex fire on 22/6/2013 in South-West Colorado (US). On the bottom is a picture of the fire and the plume taken from the ISS (NASA/EarthObservatory).

4.2.3 Assessing the significance of injection heights

Injection heights follow a strong diurnal cycle, following both the diurnal cycle for FRP and of atmospheric stability. The PRM was run for the period of 1/6/2013 to 1/8/2013 and over this period, which saw several large fire events, biomass burning emissions above the boundary layer as computed by the PRM occurred much more frequently during the night than during the day, but the associated GFAS emissions, which depend on FRP, are much larger during the day, as shown by Figure 46.

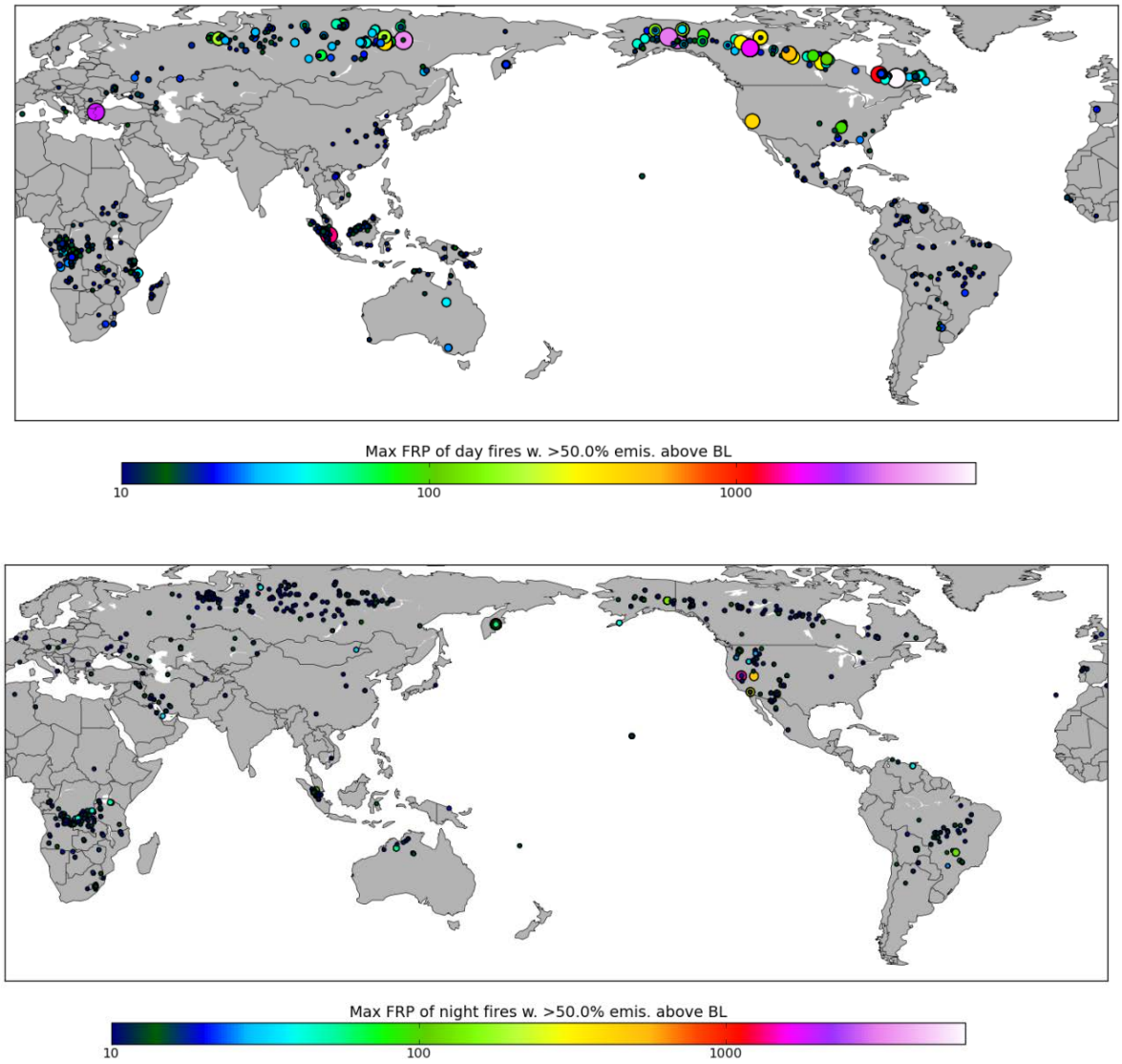

Figure 46: Aqua, maximum FRP (in MW) of fire that emit more than half of their emissions above the boundary layer, daytime fires above (9 to 21 local time), night-time fires below (21 to 9 local time).

The Plume Rise Model is essentially a convection scheme that is being forced with a fire. As the MACC forecasting system also contains its own atmospheric convection scheme, we need to ensure that the convective processes are not taken into account two times by these two schemes. That means that the relative contributions of the fire and of the atmospheric stability to the detrainment need to be assessed. To do that the PRM was run over the same period but without the forcing of the fire radiative power, and the "injection" heights (in that case, free convection of a particle from the surface) compared to the injection heights with the fire forcing. The scatterplot in Figure 47 shows that comparison.

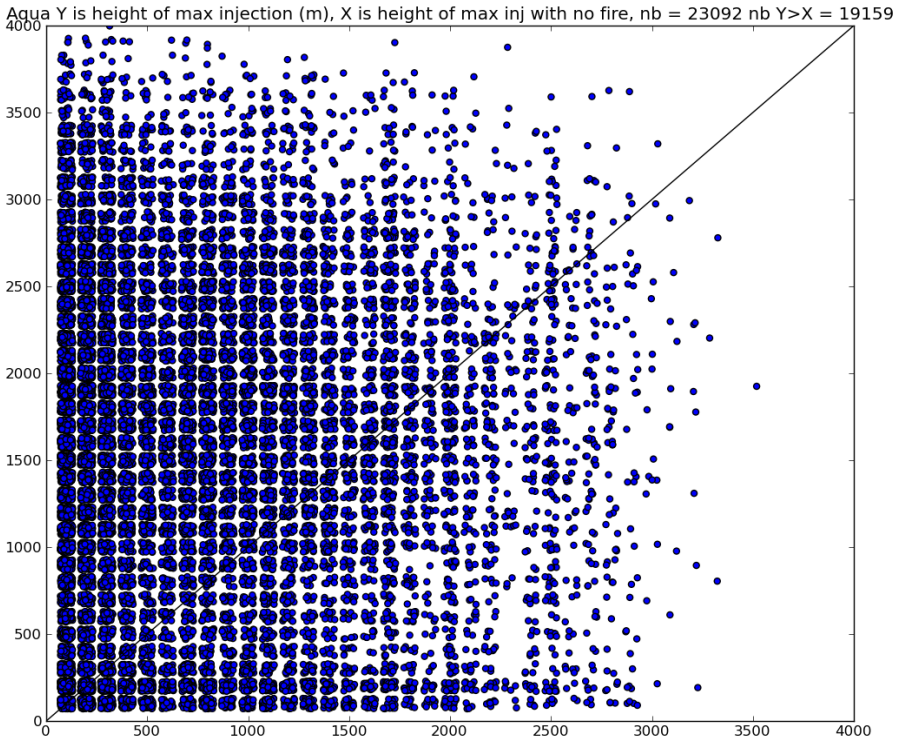

Figure 47: Aqua, Y axis is the height of maximum injection given by the PRM, in m; X axis is the height of maximum injection given by the PRM without fire radiative power forcing.

For a large majority of fires the fire forcing does contribute significantly to the maximum injection height. Figure 47 shows on the other hand that when the injection height is small, in the order of a few hundreds of meters, then quite often the injection height computed without fire forcing is actually larger. It means that for these cases, which corresponds mostly to night-time fires, the PRM output is more representative of atmospheric characteristics than of the fire power. As atmospheric characteristics are already taken care of in the global MACC system, we prefer not to take into account the injection height provided by the PRM for these particular cases. When these cases are removed, the proportion of night-time fires that emit more than half of their emissions above the boundary layer is reduced, as shown by Figure 48.

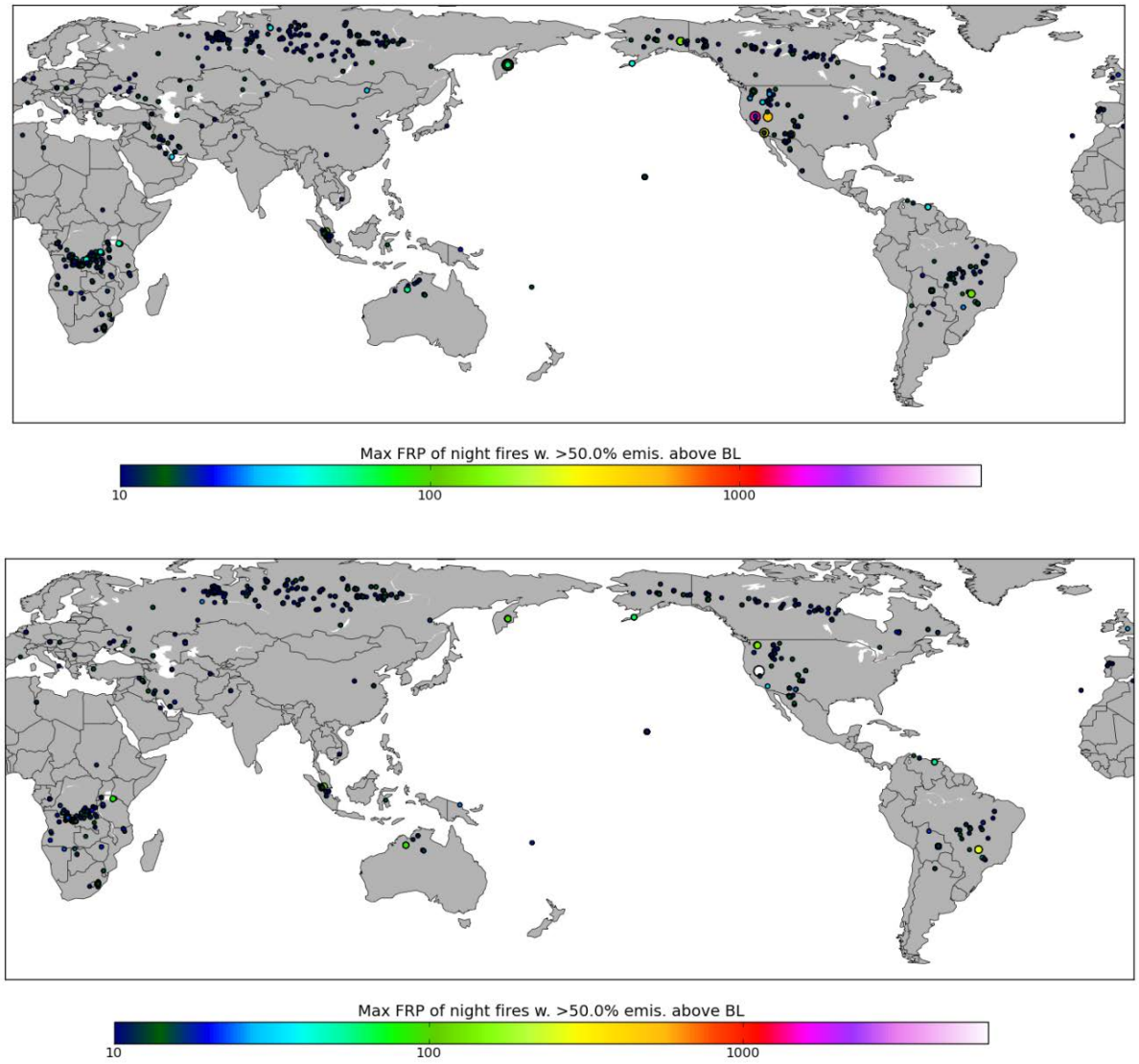

Figure 48: Aqua, maximum FRP (in MW) of night-time fire that emit more than half of their emissions above the boundary layer, no selection on top, only fires for which the maximum injection height is larger with fire forcing as compared to without fire forcing.

This test reinforces again the importance of daytime fires in terms of emissions above the boundary layer, as compared to night-time fires.

4.2.4 Available data for injection heights

The PRM produces profiles of entrainment and detrainment for every fire clusters on a 200-levels vertical grid. As this is clearly too large to keep, three parameters are kept and used out of these detrainment profiles: top and bottom height and also mean height of maximum injection. Mean height of maximal injection corresponds to the average of the heights for which the detrainment is above half of the maximal injection value. These three parameters are then gridded into the 0.1° GFAS grid and assimilated as described above in Paragraph 4.2.2. As explained in this paragraph, the temporal and spatial averaging take into account only the maximal values for each of these three parameters. The injection height according to Sofiev et al. (2012), i.e. using a simple fit to FRP and atmospheric stability, is also produced,

gridded and assimilated in the same way. Finally, the following parameters are available for users in GFAS archives:

- Height of bottom of the plume (grib id 210055)
- Height of the top of the plume (grib id 210056)
- Mean height of maximal injection, i.e. the average of the heights for which the detrainment is above half of the maximal injection value (grib id 210119)
- Injection height according to Sofiev et al. (210120)

4.2.5 Use of the injection heights in the MACC system

The global MACC system currently uses the biomass burning emissions provided by GFAS at surface level. Our aim is to modify the MACC system in collaboration with the global modelling and production sub-projects to take into account the maximum injection height for the biomass burning emissions of aerosols and reactive gases. A geographical operator was written so that injection heights can be used at the resolution of the MACC system without an interpolation stage that would provoke an important loss of information. The emissions will be injected around the mean height of maximum injection when it is higher than the height of the top of boundary layer, at the surface when it is lower.

5 Summary and Conclusions

This report presents the status in late 2013 of the development of upgrades to the Global Fire Assimilation System (GFAS) in the FIR sub-project of MACC-II. The accuracy of the production version of GFAS and user feedback on the service have been analysed in an earlier project report, Andela et al. 2013. This report summarises the research efforts that have gone into the topics that were identified in the earlier report. For several issues described in this report, the scientific investigations and algorithm developments are essentially concluded and implementation of code into the GFAS software environment has started. The following updates are expected to be incorporated into the GFAS production system in 2014:

1. The satellite data **Quality Control** (QC) scheme of GFASv1.0 is effective but blacklists a large number of “good” observations, thus leading to some unnecessary observation gap filling. It was changed to identify corrupt FRP products at the level of the MODIS granules (5 minutes of observation by one instrument) instead of at the level of daily merged MODIS products. Furthermore, a QC scheme for SEVIRI was developed. It operates at the level of single observation products, which are produced every 15 minutes.

2. The FRP observations by MODIS have a detection threshold that increases from about 4 MW under ideal observing conditions near the sub-satellite point to about 40 MW near the swath edge. This leads to an underestimation of the fire activity observed with larger viewing angles, and thus also the global FRP average calculated in GFAS. Since lower latitudes are often observed with alternatingly large and small viewing angles, a spurious oscillation with a period of about two days is introduced. In order to correct for the general FRP underestimation and the spurious oscillation, a bias correction algorithm has been developed from the MODIS observations during 2010-1012. The **correction for missing**

small fire detections by MODIS takes the observational situation, i.e. viewing angle, and fire type, i.e. FRP, into account. In addition to correcting the FRP signal, the observation error model is updated to represent to the observational situation. Thus observations with larger viewing angle receive less weight during the assimilation than those with smaller viewing angles.

3. The current version of GFAS is based on observations from the two MODIS instruments aboard the Terra and Aqua satellites. Since they sample different parts of the diurnal cycle of vegetation burning, they observe different average FRP. Thus the average FRP and fire emission rates would become biased if one instruments failed. In order to **guard against the failure of one of the MODIS instruments**, we have developed a bias correction scheme for the daily FRP estimations from each of the two MODIS instruments. It also allows extending the GFASv1 inventory by about three years to the period when only the Terra satellite was in orbit. The inventory is currently being extended back to February 2000, instead of January 2003. However, GFAS will be noisier with observation input from only one satellite. Therefore, the upcoming availability of FRP products from Suomi VIIRS and Sentinel-3 SLSTR still needs to be monitored.

4. Satellite observations of FRP include detections of thermal radiation irrespectively of the source. Vegetation fires are the vastly dominating source. However, detections of volcanoes, gas flares and other industrial installations like smelters are also reported. They need to be excluded from the further processing in GFAS. A new **spurious signal mask** for gas flares and volcanoes has been generated using published data. It is an improvement over the spurious signal map used in GFASv1 in that it (1) includes more small gas flares, (2) has a better spatial resolution of 0.1 deg, and (3) represents annual changes.

5. In order to allow for a more fire type-specific emission model, the **land cover map** underlying GFAS has been fundamentally updated: The number of basic land cover classes has been increased from four to seven. They are now based on annual observations by MODIS and are planned to be updated annually instead of the use of temporally invariant land cover map in GFASv1. In addition to the basic land cover types, a suitable peat map with global coverage has been identified and regridded. The resolution has been increased from 0.5 deg to 0.1 deg. Variability on a finer scale will be taken into account by a newly developed approach that combines percentage fire type with percentage land cover in each grid cell instead of the fixed single fire type used in GFASv1.

6. **Updated conversion factors** (FRP to dry matter burnt) have been calculated provisionally using the new land cover map. They show the strong regional influence of the dedicated peat treatment on top of the seven base land cover classes.

7. The currently static emission factors for carbon dioxide, carbon monoxide and methane by land cover will be replaced by a climatology of **emission factors with an annual cycle** to account for the typical seasonal variations in the fuel conditions and fire types. The annual variability is essentially driven by the partitioning between flaming and smouldering combustions and can be quantified through the modified combustion efficiency.

8. The table of **emission factors** to be used for all other species has been updated with version 3 of the data by Akagi et al. 2011 downloaded from the internet. For minor species, this typically changes the emission flux rates by tens of percents.

9. The **injection height** of fire emissions into the atmosphere is one of the biggest gaps in the input data needed by atmospheric modellers and research has shown that this can significantly influence long-range tracer transport. The global atmospheric MACC-II systems currently assume that all fires emit into the lowest model level. The emissions are subsequently mixed in the boundary layer and further on into the free troposphere by the standard meteorological routines, i.e. convection, diffusion and the diurnal cycle of the boundary layer height. However, big fires regularly emit smoke directly into the free troposphere and sometimes even across the tropopause. In order to represent these cases accurately, they must be identified and an estimate of the injection height must be provided. The FIR sub-project has developed a new combined burnt area and FRP product for the MODIS observations. This product is combined with meteorological fields from ECMWF in an also newly developed 1-dimensional plume rise model (PRM) to calculate vertical smoke detrainment profiles for all individual fires on the globe. The PRM is a fundamental further development of a PRM by Saulo Freitas (INPE-CPTEC) that is already published and in use by several groups around the world. The adapted PRM has successfully been integrated in the GFAS software environment at ECMWF. For test purposes, the simpler injection height parameterisation developed by Mikhail Sofiev (FMI) has also been implemented in GFAS and will be produced alongside the PRM-based injection profiles.

The above investigations have been performed using the GFASv1 data. They will be fine-tuned sequentially in the order of the data processing chain to ensure consistency within the new version of GFAS.

Several lines of investigation yield new insights as shown below. However, more research on these topics is needed before specific algorithms for updates of GFAS can be defined:

A. The representation of the **diurnal variability** of fires together with the assimilation of **FRP products from geostationary satellites** will (1) address a specification request from the atmospheric modelling community, (2) improve the accuracy of daily emission estimates and (3) increase the redundancy in satellite data inputs and thus the operational stability of GFAS. It requires a model for the diurnal fire cycle in regions with sparse observational coverage, e.g. where no geostationary data are available. Such a model is under development and a concept has been tested for Africa and the Mediterranean region, where reference data are available from SEVIRI. It also requires a correction for the large detection threshold of the geostationary instruments. This has not yet been achieved by any research group because of the complexity of the regionally and temporally varying underestimation of FRP by the geostationary instruments. Several attempts to characterise the underestimation by region and season in MACC and MACC-II have been unsuccessful. Our recent investigations show that a correction term can be found in principle if the dependence on FRP is included. Therefore, a new correction approach, which is conceptually consistent with the proposed correction for the variable detection threshold within the MODIS swath, has been proposed and will be followed in the near future. The proposed diurnal cycle model and geostationary bias correction still have the potential for being included in the next update of GFAS.

B. **Spurious signals from industrial installations** other than gas flares constitute minuscule contributions to the global FRP fields. Nevertheless, their appearance is irritating for the users. Therefore, we propose to identify the affected grid cells through visual inspection of air- and space-borne imagery and apply a corresponding mask in GFAS.

C. The approach of using land cover classification for the **conversion of FRP to dry matter** burnt will need to be augmented with a parameterisation of the physical processes involved in the emission (and transmission) of the thermal radiation, e.g. the fire type parameterised by fractional tree cover, tree cover height, relative contribution of peat burning and fuel and soil moisture. Comparison to burnt area observations will yield a better understanding of the processes involved.

D. The **variability of conversion and emission factors with actual meteorology** should be investigated and included in GFAS if possible. We propose to derive the combustion efficiency (MCE) from the meteorological conditions, and to calculate the emission factors for the individual species subsequently from the MCE. This development can build on the seasonally varying emission factors that are currently being implemented for CO2, CO and CH4.

E. **Forecasting of the evolution of the fire activiy** is implicitly done whenever a forecast of the atmospheric composition and air quality is produced. Currently, we recommend using the persistency assumption but this has been shown to lead to false alarms in some cases. Since the meteorological conditions are arguably the main drivers for fire activity, meteorologically forecasts evidently yield information on the future evolution of already detected fires. We have investigated the relationship between the meteorological conditions expressed as fire weather index (FWI) and the observed FRP. While some relationship is evident, more investigations will be performed to clarify how the relationship can be parameterised and used in routine forecasts of fire activity.

On a fundamental level, the GFASv1 approach of **calibrating the FRP-to-DM conversion factors against dry matter burnt estimates from another inventory, i.e. GFED,** appears to reach its limits eventually as it preserves the inaccuracies of the reference inventory. On the other hand, information from various observations of smoke plumes becomes more accessible through the data assimilation and validation activities of MACC-II, and the future CAS. We propose to gradually shift GFAS towards using more and more constraints from the atmospheric observations. This would effectively constitute a combination of the bottom-up and top-down approaches for emission estimation. It would require a **further development of the GFAS fire model** to incorporate more detailed physical parameterisations of, at least, the processes of combustion, emission of trace constituents and thermal radiation, and smoke plume dynamics and chemistry.

The formulation of such a model should be guided by comparisons to other inventories, various fire observations, and fine-scale fire spread modelling. Since building such a fire model will require expert knowledge from a range of scientific disciplines involved in fire research, it would benefit greatly from an active involvement in the Interdisciplinary Biomass Burning Initiative (IBBI), which has recently been created by WMO, IGAC and iLEAPS; The Copernicus Atmosphere Service should consequently **support IBBI**.

The main uncertainties of the model should then be expressed as **parameters that can subsequently be estimated using the global satellite observations** of atmospheric smoke. This will only be possible in very close collaboration with the follow-up activities of the global production and the validation sub-projects of MACC-II. The parameters can then also be included in the state parameter of the atmospheric data assimilation of the global MACC-II system to vary the fire emission estimation in time, in order to create an optimal adjustment to the boundary condition needs of the global atmospheric composition model. This might even compensate for some deficiencies in the atmosphere model. It would be a realisation of the recommendation of developing more sophisticated emission models together with including emission parameters in the 4D-VAR state vector, which was concluded at the *Workshop on parameter estimation and inverse modelling for atmospheric composition* held at ECMWF in October 2013.

6 References

Akagi, S. K., Yokelson, R. J., Wiedinmyer, C., Alvarado, M. J., Reid, J. S., Karl, T., Crounse, J.D., and P. O. Wennberg (2011). Emission factors for open and domestic biomass burning for use in atmospheric models. *Atmospheric Chemistry and Physics*, 11(9), 4039-4072.

Andela, N., Kaiser, J.W., Heil, A., van Leeuwen, T. T., van der Werf, G. R., Wooster, M.J., Remy, S. and Schultz, M.G. (2013). Assessment of the Global Fire Assimilation System (GFASv1). ECMWF Tech. M. 702. http://www.gmes-atmosphere.eu/about/project_structure/input_data/d_fire/lit/20130510_MACCII_GFAS_Assesment_report.pdf.

Andreae, M. O., and Merlet, P. (2001). Emission of trace gases and aerosols from biomass burning. *Global biogeochemical cycles*, 15(4), 955-966.

De Groot, W.J., Field, R.D., Brady, M.A., Roswintiarti, O. and Mohamad, M. (2007). Development of the Indonesian and Malaysian Fire Danger Ratign Systems. Mitig. Adapt. Strat. Glob. Change. 12: 165-180.

Dozier, J. (1981), A method for satellite identification of surface temperature fields of subpixel resolution, Remote Sensing of Environment, 11, 221-229, doi: 10.1016/0034-4257(81)90021-3.

Eskes, H.J., V. Huijnen, A. Wagner, M. Schulz, K. Lefever (eds.) (2013). Validation report of the MACC near-real time global atmospheric composition service, MACC-II deliverable D_82.9. http://gmes-atmosphere.eu/documents/maccii/deliverables/val/MACCII_VAL_DEL_D_82.9_NRTReport07_20131002.pdf

Freeborn, P. H., Wooster, M. J., and Roberts, G. (2010). Addressing the spatiotemporal sampling design of MODIS to provide estimates of the fire radiative energy emitted from Africa. Remote Sensing of Environment, 115:475–498.

Freitas, S., Longo, K., Chatfield, R., Latham, D., Silva Dias, M., Andreae, M., Prins, E., Santos, J., Gielow, R., and Carvalho Jr., J. (2007). Including the sub-grid scale plume rise of vegetation fires in low resolution atmospheric transport models. Atmos. Chem. Phys., 7:3385–3398.

Ellicott, E., Vermote, E., Giglio, L., and Roberts, G. (2009). Estimating biomass consumed from fire using MODIS FRE. *Geophysical Research Letters*, 36, L13401, doi:10.1029/2009GL038581.

Heil, A., Kaiser, J. W., van der Werf, G. R., Wooster, M. J., Schultz, M. G., and D. H. van der Gon (2010). Assessment of the Real-Time Fire Emissions (GFASv0) by MACC. *Tech. Memo. 628*, ECMWF, Reading, UK.

Hely, C., S. Alleaume, R. J. Swap, H. H. Shugart, and C. O. Justice (2003). SAFARI-2000 characterization of fuels, fire behavior, combustion completeness, and emissions from experimental burns in infertile grass savannas in western Zambia. *Journal of Arid Environments*, 54(2), 381–394, doi:10.1006/jare.2002.1097.

Hoffa, E. A., D. E. Ward, W. M. Hao, R. A. Susott, and R. H. Wakimoto (1999). Seasonality of carbon emissions from biomass burning in a Zambian savanna. *Journal of Geophysical Research-Atmospheres*, 104, 13841–13853.

Hyer, E. J., Reid, J. S., Prins, E. M., Hoffman, J. P., Schmidt, C. C., Miettinen, J. I., and Giglio, L. (2013). Patterns of fire activity over indonesia and malaysia from polar and geostationary satellite observations. Atmospheric Research, 122:504–519.

Jones, J. W., A. E. Hall, A. M. Foster, and T. J. Smith (2013). Wetland fire scar monitoring and analysis using archival Landsat data for the Everglades. Fire Ecology 9(1): 133-150. doi: 10.4996/fireecology.0901133

Kaiser, J. W., Heil, A., Andreae, M. O., Benedetti, A., Chubarova, N., Jones, L., Morcrette, J. J., Razinger, M., Schultz, M. G., Suttie, M., and G. R. van der Werf (2012). Biomass burning emissions estimated with a global fire assimilation system based on observed fire radiative power. *Biogeosciences*, 9(1), 527-554.

Kaiser, J. W., Heil, A., Schultz, M. G., Remy, S., Stein, O., van der Werf, G. R., Wooster, M. J., and Xu, W. (2013). Final report on implementation and quality of the D-FIRE assimilation system. Tech. Memo. 709, ECMWF.

Korontzi, S., D. E. Ward, R. A. Susott, R. J. Yokelson, C. O. Justice, P. V. Hobbs, E. Smithwick, and W. M. Hao (2003). Seasonal variation and ecosystem dependence of emission factors for selected trace gases and PM2.5 for southern African savannah fires. *Journal of Geophysical Research-Atmospheres*, *108*, 4758, doi:10.1029/2003JD003730.

Lappalainen, E. (editor) (1996). Global Peat Resources; International Peat Society, Finland http://www.peatsociety.org/peatlands-and-peat/global-peat-resources-country.

Meyer, C. P., G. D. Cook, F. Reisen, T. E. L. Smith, M. Tattaris, J. Russell-Smith, S. W. Maier, C. P. Yates, and M. J. Wooster (2012). Direct measurements of the seasonality of emission factors from savannah fires in northern Australia. *Journal of Geophysical Research*, *117*(D20), D20305, doi:10.1029/2012JD017671.

Oom, S. and J.M.C. Pereira (2013). Exploratory spatial data analysis of global MODIS active fire data. *International Journal of Applied Earth Observation and Geoinformation*, 21, 326–340.

Page, S. E., C. J. Banks, J. Rieley, (2010). Technical report 1: Extent and significance of Tropical Peat Carbon Pools. University of Leicester and Carbopeat partner. http://www.geog.le.ac.uk/carbopeat/media/pdf/tr1.pdf.

Pappenberger, F. (2012) Pilot study: Global multi-hazard forecasting information platform for weather driven natural disasters. In possession of F. Pappenberger, ECMWF, Reading.

Pergaud, J., Masson, V., Malardel, S. and Couvreux, F : A Parameterization of Dry Thermals and Shallow Cumuli for Mesoscale Numerical Weather Prediction, 132, vol. 1, 83-106, doi : 10.1007/s10546-009-9388-0

Roberts, G., Wooster, M. J., Freeborn, P. H., and Xu, W. (2011). Integration of geostationary frp and polar-orbiter burned area datasets for an enhanced biomass burning inventory. Remote Sensing of Environment, 115(8):2047–2061.

Sofiev, M., Ermakova, T., and Vankevich, R. (2012). Evaluation of the smoke injection height from wild-land fires using remote sensing data. ACP, 12:1995–2012.

Strack, M. (2008) (ed.). Peatlands and Climate Change. Jyväskylä, International Peat Society. Saarijärvi, Finland, 223 pp.

Taylor, S.W. & Alexander, M.E. (2006) Science, technology and human factors in fire danger rating: the Canadian experience. International Journal of Wildland Fire. 15:121-135.

Val Martin, M., Logan, J. A., Kahn, R., Leung, F. Y., Nelson, D., and Diner, D. (2007). Smoke injection heights from fires in North America: analysis of 5 years of satellite observations, Atmos. Chem. Phys., 10, 1491-1510.

van der Werf, G. R., Randerson, J. T., Giglio, L., Collatz, G. J., Mu, M., Kasib- hatla, P. S., Morton, D. C., DeFries, R. S., Jin, Y., and van Leeuwen, T. T. (2010). Global fire emissions and the contribution of deforestation, savanna, forest, agricultural, and peat fires (1997–2009). Atmos. Chem. Phys., 10:11707–11735.

Van Leeuwen, T. T., and G. R. Van Der Werf (2011). Spatial and temporal variability in the ratio of trace gases emitted from biomass burning. *Atmospheric Chemistry and Physics*, 11(8), 3611– 3629, doi:10.5194/acp-11-3611-2011.

Van Leeuwen, T. T., W. Peters, M. C. Krol, and G. R. Van Der Werf (2013). Dynamic biomass burning emission factors and their impact on atmospheric CO mixing ratios. *Journal of Geophysical Research – Atmospheres*, 118(12), 6797-6815, doi:10.1002/jgrd.50478.

Van Wagner, C.E. (1987) Development and structure of the Canadian Forest Fire Weather Index System. Forestry Technical Report 35. Canadian Forestry Service.

Vermote, E., Ellicott, E., Dubovik, O., Lapyonok, T., Chin, M., Giglio, L., and Roberts, G. J. (2009). An approach to estimate global biomass burning emissions of organic and black carbon from MODIS fire radiative power. *Journal of Geophysical Research: Atmospheres*, *114*, D18205, doi:10.1029/2008JD011188.

Wooster, M. J., P. H. Freeborn, S. Archibald, C. Oppenheimer, G. J. Roberts, T. E. L. Smith, N. Govender, M. Burton, and I. Palumbo (2011). Field determination of biomass burning emission ratios and factors via open-path FTIR spectroscopy and fire radiative power assessment: headfire, backfire and residual smouldering combustion in African savannahs. *Atmospheric Chemistry and Physics*, 11(22), 11591–11615, doi:10.5194/acp-11-11591-2011.

Yu, Z. C. (2012). Northern peatland carbon stocks and dynamics: a review. *Biogeosciences*, 9, 4071-4085, doi:10.5194/bg-9-4071-2012.

Zhang, X., Kondragunta, S., Ram, J., Schmidt, C., and Huang, H. C. (2012). Near- real-time global biomass burning emissions product from geostationary satellite constellation. JGR, 117(D14):D14201.

Appendix: Analysis of the top 10 FRP signals during 2008 to 2012 in fl6z

The analysis of the top 10 daily mean FRP signals (Table 19) shows that these extreme values are populated by volcanic signals and most likely biomass burning signals.

TDMA	DAYMAX [Wm-2]	Date	LAT,LON	Country/Region	Description	Identified as	Masked via NBB3 mask
1	214.35	2008-11-03	13.85,40.55	Ethiopia, Afar region	Eruption of Dalafilla volcanoe with widepread lava flow.	VOLCANOE	Yes
2	211.18	2011-10-04	-21.15,136.95	Autralia, NT, Costello	Area covered by shrublands. No artificical construction visible.	FIRES?	No
3	202.02	2008-11-04	13.85,40.55	Ethiopia, Afar region	Eruption of Dalafilla volcanoe with widepread lava flow.	VOLCANOE	Yes
4	196.07	2008-06-29	59.25,253.85	Canada, Saskatchewan	Area covered by forests/shrublands. No artificical construction visible.	FIRES?	No
5	190.88	2009-08-06	64.25,211.15	United States, AK, Denali	Area covered by natural vegetation. No artificical construction visible. Signal occurs	FIRES?	No
6	180.50	2012-11-22	-32.85,123.15	Australia, Western Australia,	Area covered by natural vegetation. No artificical construction visible. Signal occurs	FIRES?	No
7	138.05	2011-09-09	50.15,354.45	United Kingdom, Cornwell	Area dominated by intensive agriculture. No gas flaring or industrial construction visible,	UNCLEAR	No
8	134.52	2010-06-22	50.65,288.25	Canada, QC, Maria-Chapdelaine	Area covered by natural vegetation. No artificical construction visible.	FIRES?	No
9	133.91	2009-08-06	64.25,211.25	United States, AK, Denali	Area covered by natural vegetation. No artificical construction visible. Signal occurs	FIRES?	No
10	132.06	2010-06-01	64.15,208.75	United States, AK, Yukon-Koyukuk	Remote area covered by natural vegetation. No artificical construction visible. Signal	FIRES?	No

Table 19: Identification of top ten daily maximum FRP signals over 2008 to 2012 in fl6z.

TDMAX-1: Eruption of the Dalafilla volcanoe in Ethiopia's Afar region on Nov. 3, 2008 with widespread lava flows travelling to the NE

On November 3, 2008, the Dalaffilla in Ethopias Afar region erupted for the first time in recorded history. There was widespread north-east lava flow from a fissure northwest of Dalaffilla, expanding over an area of 15 km2[7]. The eruptive activity deceased until end of November 2008. This NBB event is identified in the Oom and Pereira (2013) inventory and therefore masked out with the new GFAS NBB mask.

The geolocation of the volcano and the lava flow during the eruption, which is clearly visible in Bing map and GoogleEarth point to a northward dislocation of the fl6z 0.1 deg grid cell (the fl6z appears to be shifted northward by half grid cell out of the bounds of maximum volcanic activity). We will check this aspect in more detail with other landmarkers (volcanoes, industrial sites).

[7] http://www.volcano.si.edu/volcano.cfm?vnum=0201-07

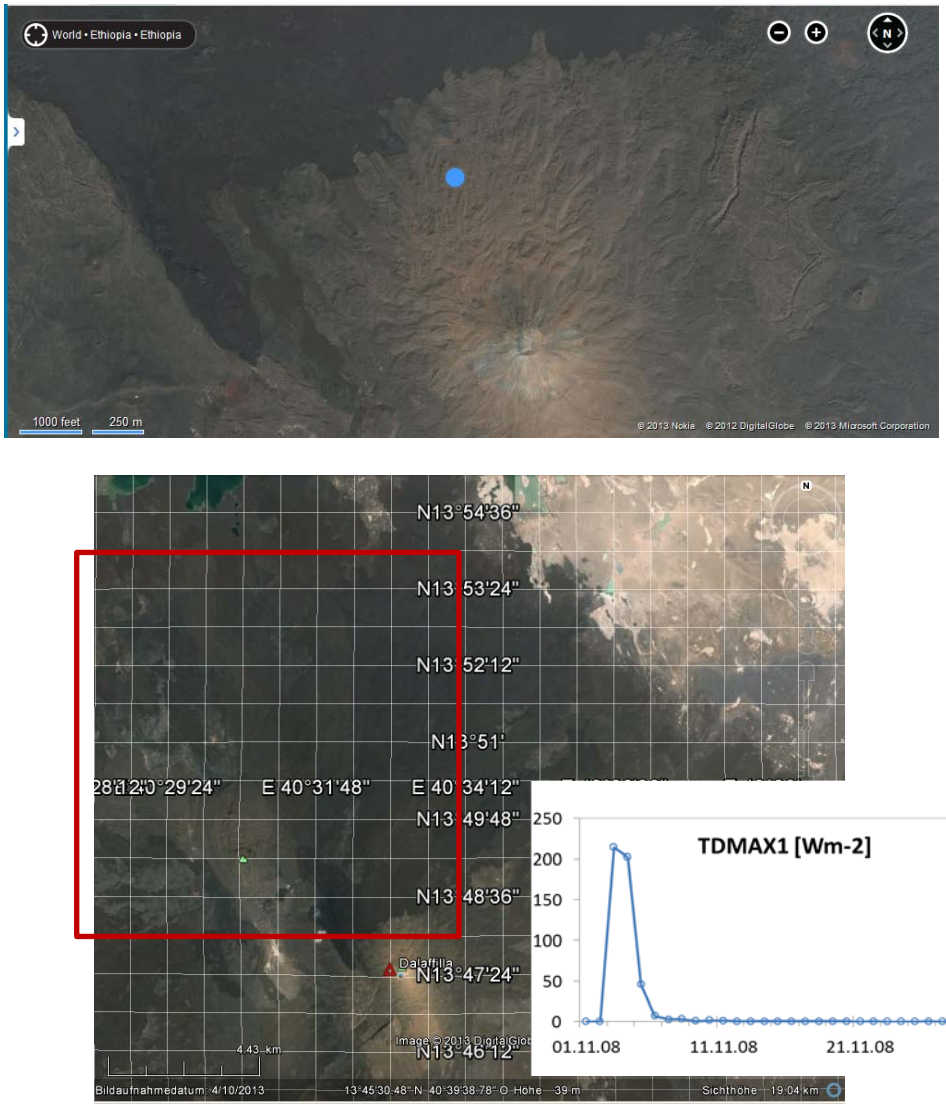

Figure 49: (a) Bing aerial map of TDMAX1 with a blue marker shown at 40.55°E and 13.8°N (which is the southern bound of the TDMAX1 grid cell). (top) and (b) Google Earth Image of the Dalaffilla volcanoe. The grid lines are spaced in 0.01 degree. Encircled in red is the area of the TDMAX1 grid cell, centered at 40.55°E and 13.85°N (bottom).

TDMAX-2: Presumably bushfire (likely) in Australia, Northern Territory, Costello region, on Oct 4, 2011

In September and October 2011, intensive bushfires plagued Central and Northern Australia[8]. TDMAX appears in an area covered by dense bushes and during a period of extreme bushfires in the regions. The GFAS signal is therefore most likely due to an intense bushfire, although no related news reports could be found in the internet.

[8] http://www.ntnews.com.au/article/2011/10/16/266651_ntnews.html2011-10-04

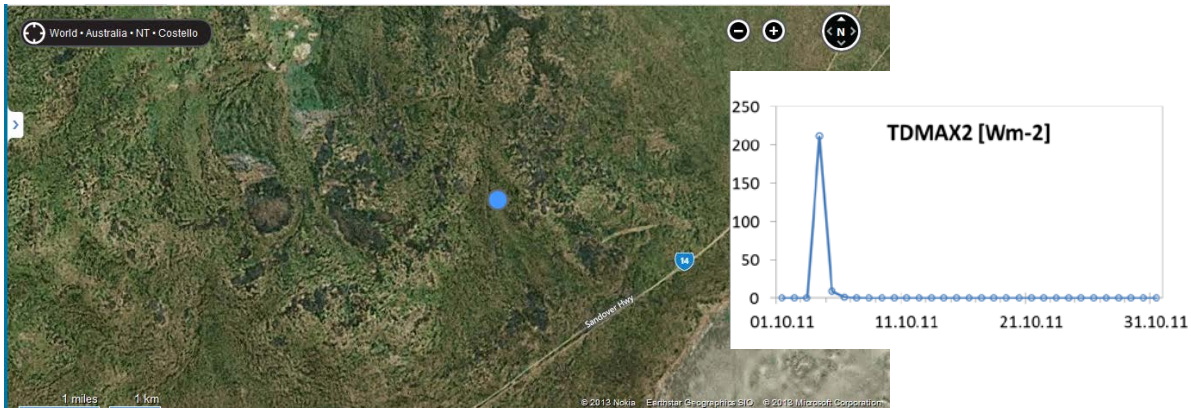

Figure 50: Bing aerial map of TDMAX2 (centered at 21.15°S, 136.95°E, blue marker). The signal occurs in an area covered by dense bushes. The blackish areas could point to burn scars.

TDMAX-3: Continued lava flow of the eruptive Dalafilla volcanoe on Nov. 4, 2008

See TDMAX-1

TDMAX-4: Presumably forest fires

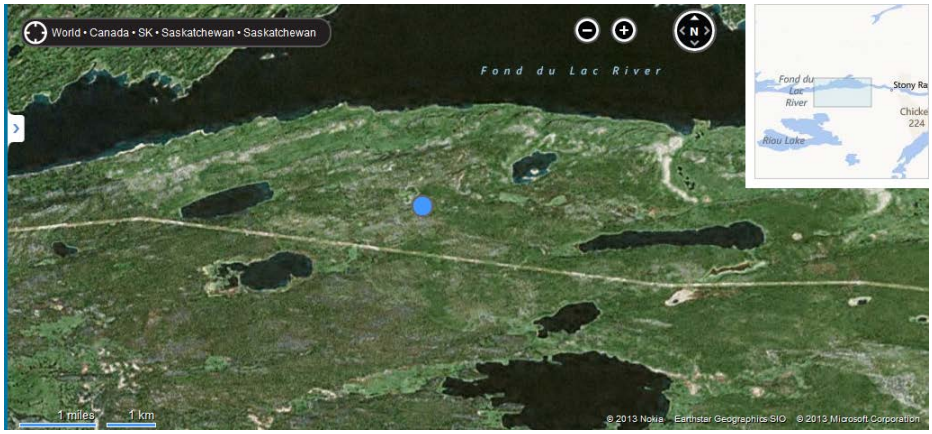

Figure 51: Bing map of TDMAX-4.

TDMAX-5: Presumably forest fire in Denali National Park region

TDMAX-5 occurs during a period of extreme fire risk in an area with natural vegetation.[9]

[9] http://www.nps.gov/dena/parknews/firebanaug05.htm

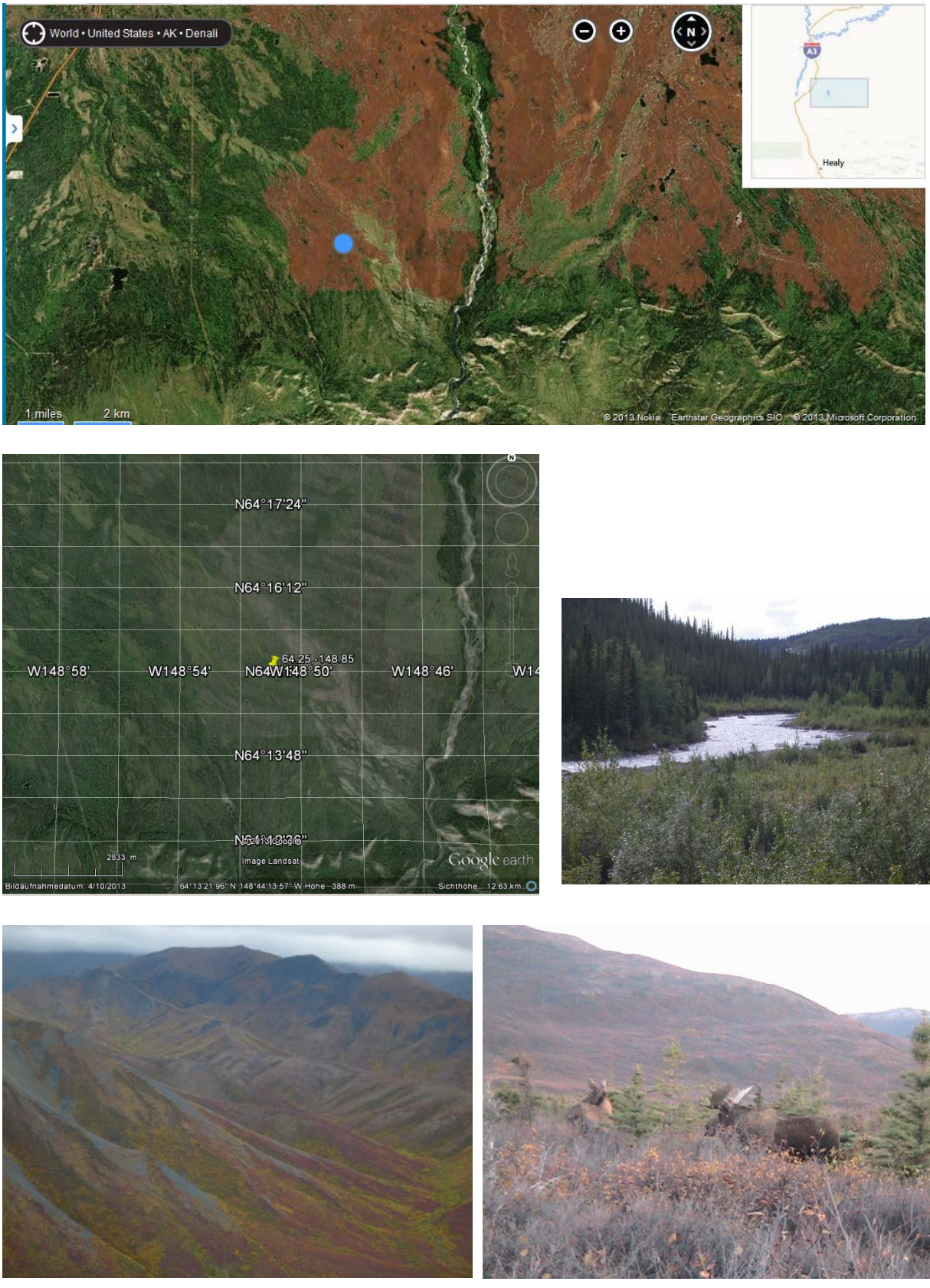

Figure 52: Bing and GoogleEarth imagery of TDMAX-5, complemented by photos of the typical vegetation.

TDMAX-6: Presumably forest fire

TDMAX-6 occurs during a period of extreme fire risk in an area with natural vegetation.

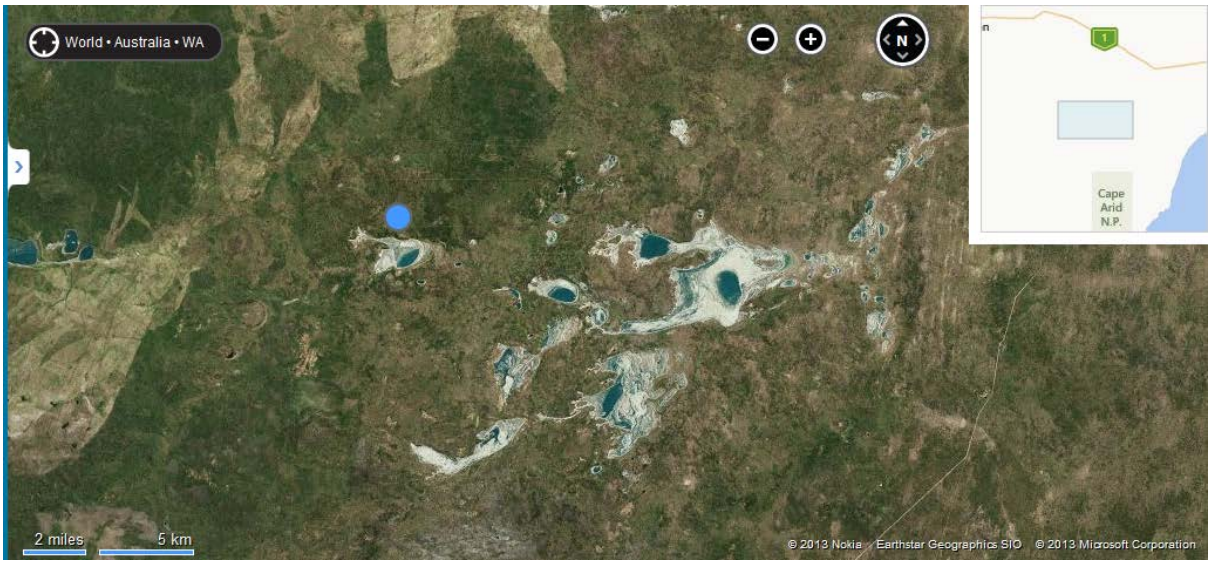

Figure 53: Bing imagery of TDMAX-6.

TDMAX-7: Presumably agricultural waste burning

TDMAX-7 in an area dominated by intensive agriculture. Unclear reason, possibly agricultural burning.[10]

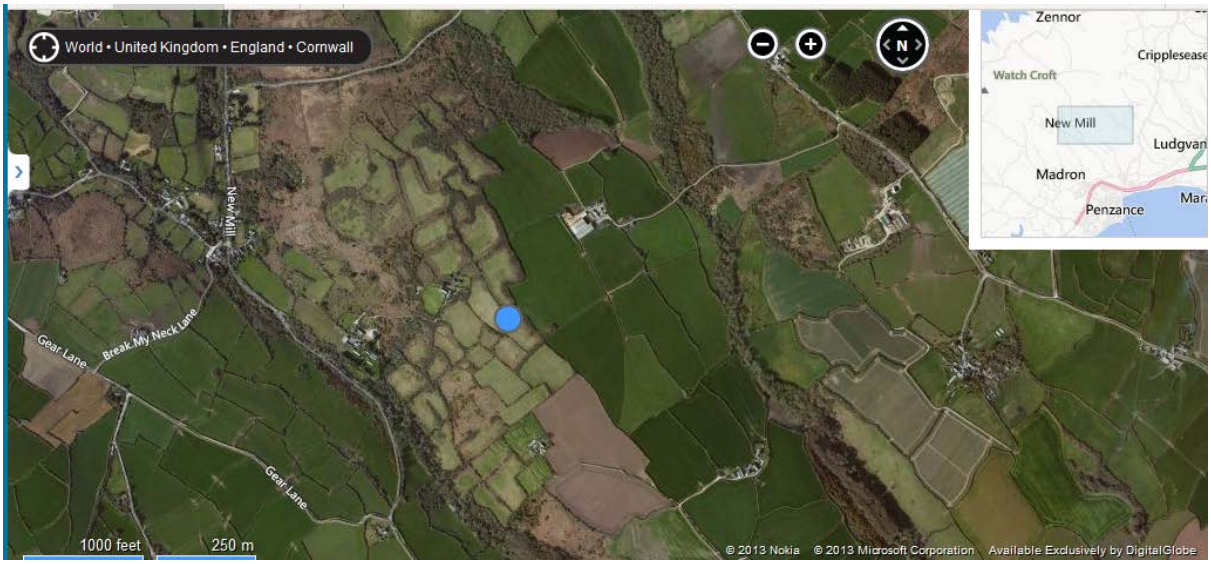

Figure 54: Bing imagery of TDMAX-7.

TDMAX-8: Presumably vegetation fire

[10] http://www.cornishmutual.co.uk/blog/posts/2013/january/thinking-about-burning-grassland-or-heath-do-you-know-what-to-do/

TDMAX-8 in a remote area covered by natural vegetation.

Figure 55: Bing imagery of TDMAX-8, complemented by a photo displaying the typical natural vegetation.

TDMAX-9

See TDMAX-5

TDMAX-10

See TDMAX-5

Figure 56: Bing imagery of TDMAX-10.